

**Numerical Analysis of Die-Casting Process in
Thin Cavities using Lubrication Approximation**

by

Alexandre Reikher

A Dissertation Submitted in

Partial Fulfillment of the

Requirements for the Degree of

Doctor of Philosophy

In Engineering

at

The University of Wisconsin Milwaukee

December 2012

ABSTRACT

Numerical Analysis of Die-Casting Process in Thin Cavities using Lubrication Approximation

by

Alexandre Reikher

The University of Wisconsin Milwaukee, 2012

Under the Supervision of Professor Krishna M. Pillai

Casting of thin wall parts has become a reality of the die cast industry today. Computational fluid dynamics analyses are an integral part of the production development process. Typically the three-dimensional Navier-Stokes equations coupled with the energy equation have to be solved in order to gain an understanding of the flow and solidification patterns, position of the flow front, as well as location of the solid-liquid interface as a function of time during the process of cavity filling and solidification. A typical solution of the governing equations for a thin-wall casting requires large number of computational cells, and as a result, takes impractically long time to generate a solution. Using the Hele-Shaw flow modelling approach, solution of the flow problem in a thin cavity can be simplified by neglecting the out-of-plane flow. As a further benefit, the problem is reduced from a three-dimensional problem to a two-dimensional one. But the Hele-Shaw approximation requires that viscous forces in the flow are much higher than its inertia forces, and in such a case, the Navier-Stokes equation reduces to the Reynolds's lubrication equation. However, owing to the fast injection speed of the die-cast process, the inertial forces cannot be neglected. Therefore the lubrication equation has to be modified to include the inertial effects of the flow.

In this PhD thesis, a fast numerical algorithm is developed for modeling the steady-state and transient flows of liquid metal accompanied by solidification in a thin cavity. The described problem is closely related to the cold-chamber, high-pressure die-cast process and in particular to the metal flow phenomenon observed in thin ventilation channels.

Using the fact that the rate of metal flow in the channel is much higher than the solid-liquid interface velocity, a novel numerical algorithm is developed by treating the metal flow as *steady* at a given time-step while treating the heat transfer along the thickness direction as transient. The flow in the thin cavity is treated as two-dimensional after integrating the momentum and continuity equations over the thickness of the channel, while the heat transfer is modelled as a one-dimensional phenomenon in the thickness direction. The staggered grid arrangement is used to discretize the flow governing equations and the resulting set of partial differential equations is solved using the SIMPLE(Semi-Implicit Method for Pressure-Linked Equations) algorithm. The thickness direction heat-transfer problem accompanied by phase change is solved using a control volume formulation. The location and shape of the solid-liquid interface are found using the Stefan condition as a part of the solution. The simulation results are found to compare well with the predictions of the commercial software FLOW3D[®] that solves the full three-dimensional set of flow and heat transfer equations accompanied with solidification.

The proposed numerical algorithm was also applied to solve a *transient* metal-filling and solidification problem in thin channels. The presence of a moving solid-liquid interface introduces a non-linearity in the resulting set of flow equations, which are now solved iteratively. Once again, a good match with the predictions of FLOW3D[®] was observed.

These two studies indicate that the proposed inertia-modified Reynolds's lubrication equations accompanied by through-the-thickness heat loss and solidification models can be successfully implemented to provide a quick analysis of flow and solidification of liquid metals in thin channel during the die cast process. Such simulation results, obtained with tremendous savings in CPU time, can be used to provide a quick, initial analysis during the design of the ventilation channels of a die-cast die.

Table of Contents

Abstract	ii
Table of Contents	iv
List of Figures and Tables	vii
1. Introduction	
1.1 Casting processes	1
1.2 Sand casting process	1
1.3 Permanent mold	2
1.3.1 Gravity casting	3
1.3.2 Low-pressure permanent mold casting	4
1.3.3 Counter-pressure casting	4
1.4 Die casting	5
1.5 Die cast process	6
1.5.1 Hot chamber process	7
1.5.2 Cold chamber process	9
1.6 Challenges of metal flow in thin cavities	10
2. Literature overview	12

2.1	Historical overview of numerical methods	12
2.2	The finite difference methods	13
2.3	Control volume Method (CVM)	13
2.4	Free surface approximation	14
2.4.1	Marker and cell (MAC) method	14
2.4.2	Surface marker method	15
2.4.3	Free surface approximation using Volume of Fluid (VOF) Method	15
2.5	Reynolds's lubrication approximation	16
2.6	Scope and objective	17
3.	A fast numerical simulation for modeling simultaneous metal flow and solidification in thin cavities using the lubrication approximation	19
3.1	Introduction	20
3.2	Development of steady state solution of flow in thin cavity	25
3.3	Governing equations	29
3.4	Solution procedure	37
3.5	Results	41
3.6	Conclusion	46

4.	A fast simulation of transient metal flow and solidification in a narrow channel	47
4.1	Transient model development	47
4.2	Main cavity model	49
4.3	Thin channel model	50
4.4	Coupling of the main cavity and thin channel flows	54
4.5	Discretization of governing equations	55
4.5.1	Main cavity	55
4.5.2	Thin channel	56
4.6	Solution procedure	57
4.6.1	Solution procedure in main cavity	57
4.6.2	Solution procedure in thin channel	60
4.7	Summary of numerical methods	64
4.8	Validation of the Proposed Numerical Algorithm	64
4.9	Validating velocity distribution in the channel	68
4.10	Validating solidification analysis	70
4.11	Validating locations of liquid metal-air and solid-liquid interfaces	71
4.12	Verification of solidification rate using measured secondary dendrite arm spacing	78
4.13	Significant Improvement in Computational Speed	81
4.14	Further Validation through a Parametric Study	82

4.14.1	Effect of changes in ventilation-channel thickness	82
4.14.2	Effect of changes in wall temperature of the ventilation channel	83
4.14.3	Effect of changes in the initial metal velocity	84
4.15.	Summary and conclusions	86
5.	Some Concerns and Future Research Directions	88
6.	References	93
Appendix A	Reynolds lubrication equation after including the effect of inertia	98
Appendix B	Discretization of momentum equations	107
Appendix C	Estimation of the location of solid-liquid interface	111
CURRICULUM VITAE		113

List of Figures

No	Description	Page
Fig. 1.1	Schematic representation of sand casting mould	2
Fig. 1.2	Schematic representation of hot chamber die cast machine	8
Fig. 1.3	Schematic representation of steps in the hot-chamber die-cast process	8
Fig. 1.4	Schematic representation of cold chamber die-cast machine	9
Fig. 1.5	Schematic representation of steps in the cold chamber die-cast process	10
Fig. 2.1	Control volume method	14
Fig. 2.2	Volume of fluid method	16
Fig. 3.1	Straight channel with a rectangular cross-section: the liquid metal enters from the left-most section in the y-z plane, flows along the x direction, and then exits from the other end.	26
Fig. 3.2	A typical control volume, defined around the nodes of the mid-level x-y plane, is used to model the z-direction heat loss and subsequent solidification, in the thin cavity.	36
Fig. 3.3	Flow chart for the steady state solution algorithm	40
Fig. 3.4	Grid independence study conducted at z=0.5 plane. [The cavity width in y direction was non-dimensionalized as y/L , Eq(3.8), after using the length of the cavity as $L=0.1(m)$. The velocity was rendered dimensionless as u/\bar{v} , Eq(3.8), after employing the characteristic velocity value of $\bar{v}=1(m/s)$.]	42
Fig. 3.5	Velocity distribution; a) Velocity distribution at $x=0.2$, b) Velocity distribution at $x=0.5$, c) Velocity distribution at $x=0.9$ [The cavity	43

No	Description	Page
	width in y direction was non-dimensionalized as y/L , Eq(3.8), after using the length of the cavity as $L=0.1(\text{m})$. The velocity was rendered dimensionless as u/\bar{V} , Eq(3.8), after employing the characteristic velocity value of $\bar{V}=1(\text{m/s})$.].	
Fig. 3.6	Temperature distribution along the cavity thickness at time=1s: a) Temperature distribution at $x=0.2$; b) Temperature distribution at $x=0.5$; c) Temperature distribution at $x=0.9$. Coordinate in the z direction was non-dimensionalized as z/H_o , Eq(3.8), while using $H_o = 0.001(\text{m})$ as the cavity thickness.	44
Fig. 3.7	Evolution of the solid–liquid interface with time for $u=1$: a) The interface location at $t=0.5\text{s}$, b) The interface location at $t=1\text{s}$. [The cavity length in x direction was non-dimensionalized as x/L , Eq(3.8), after using the length of the cavity as $L=0.1(\text{m})$. Coordinate in the z direction was non-dimensionalized as z/H_o , Eq(3.8), while using $H_o = 0.001(\text{m})$ as the cavity thickness.]	45
Fig. 4.1	A schematic showing the thick and thin section of a typical die-cast part	48
Fig. 4.2	A schematic showing the main cavity and the thin channel of a die-cast die connected through a cut-off plane.	49
Fig. 4.3	The thin-channel geometry used for model validation: the left- and right-side segments are 1 mm and 0.5 mm thick, respectively.	54
Fig. 4.4	The staggered grid arrangement (based on SIMPLE algorithm) was employed for solving the in-plane flow variables.	56
Fig. 4.5	The proposed solution algorithm for solving flow and temperature	58

No	Description	Page
	variables in the thin cavity.	
Fig. 4.6	A schematic of a die-cast die with shot sleeve and plunger: 1) Shot sleeve, 2) Plunger, 3) Stationary half of the die-cast die, 4) Ejector half of the die-cast die, 5) Mold cavity, 6) Ventilation channel.	59
Fig. 4.7	Typical plunger velocity profile (IPS = inches per second)— 'position' is the distance plunger travels during the die cast process.	60
Fig. 4.8	A picture (a 'full shot') of a part made using the die-cast process. The overflows are created when the metal front, after filling the main cavity, fills up the machined 'overflow' pockets in the die-cast mold. Ventilation channel is last to fill-up.	65
Fig. 4.9	Flow analysis results using FLOW3D of the metal flow and solidification in the main cavity.	66
Fig. 4.10	Temperature distribution in the considered cavity of the die-cast die, filled with liquid metal at the end of the fill process.	66
Fig. 4.11	A schematic of the considered ventilation channel: the stepped profile is necessary to solidify and contain the overflowing metal. The dimensions a, b and c are listed in Table 4.1.	67
Fig. 4.12	A schematic showing a typical cross-section of the stepped ventilation channel	69
Fig. 4.13	Comparison of velocity distributions in the ventilation channel: (Left at 0.05s) section I and (Right at 0.05s) section II of Figure 4.12. Note that the plot gives velocities averaged along the thickness direction.	69

No	Description	Page
Fig 4.14	Comparison of temperature distributions in the ventilation channel: (Left at 0.05s) section I and (Right at 0.05s) section II of Figure 4.12.	71
Fig 4.15	Locations of the free surface: Proposed numerical algorithm (top), FLOW3D (bottom) at a) 0.01s, b) 0.018s, c) 0.029s, d) 0.045s, e) 0.06s [In all views, the horizontal axis along 'x' direction is along the channel length, while the vertical axis is the width of the channel (m) in 'y' direction]	72
Fig 4.16	Experimentally observed solidified metal in the ventilation channel	74
Fig 4.17	Location of the solid-liquid interface predicted by simulations: the proposed algorithm (top), commercial software FLOW3D (bottom) at a) 0.036s, b) 0.055s, c) 0.06s. The yellow (light) color represents the liquid metal while the green (dark) color signifies solidified metal.	78
Fig 4.18	Cross section of the casting used to measure SDAS (200X magnification)	79
Fig 4.19	Temperature history at the centreline of location I in Figure 4.12; the solidification rate, v , is obtained from the slope of the curve.	81
Fig 4.20	Metal flow-length vs. cavity thickness—result of the parametric study.	83
Fig 4.21	Metal flow-length vs. wall temperature—result of the parametric study.	84
Fig 4.22	Metal flow-length vs. metal velocity at the entrance of the	85

No	Description	Page
	ventilation channel—result of the parametric study.	
Figure 5.1	The measure solidification curve for aluminum A380 alloy	90
Figure 5.2	The first-derivative curve, obtained from the slope of the solidification curve shown in Figure 5.1, is overlaid on the original solidification curve.	90
Figure 5.3	Non-dendrite structures seen in the micrograph of a section of a thin ventilation channel.	91
Fig B.1	Staggered grid arrangement	107
Fig B.2	Grid lines arrangement near the channel walls	109
Fig. C1	Metal solidification in the channel	112

List of tables

Table 1.1	Properties of alloys	6
Table 3.1	Properties of A380 aluminum	25
Table 4.1	Thin channel dimensions	68
Table 4.2	Values of variables in Eqs.(4.20-4.21)	80

Chapter 1: Introduction

1.1 Casting Processes

There are several casting methods that are used to produce light metal parts. The most widely used are

- Sand casting
- Permanent mould casting
- Die casting

Usually economic considerations are the driving force in deciding which casting process can be used. The sand casting process requires the least amount of up-front investment in tooling. But parts cannot be produced with close tolerances and minimum machine stock¹. It will require extra machining operations, which will drive the part price up.

Permanent mould requires up-front investing in tooling. But parts can be cast with much closer tolerances and less machining operations. Due to intensive cooling, parts can be produced in a much shorter cycle time, compared with sand casting.

The die-cast process requires a large up-front investment in tooling. Due to high pressure used during the die-cast process, parts can be produced with close tolerances and minimum machine stock.

1.2 Sand Casting

Sand casting is the oldest way to produce near net-shape parts. Sand casting moulds (Figure 1.1) are made using green or chemically bonded sand. Green sand moulds use

¹ Machine stock is a material added to the casting surface for subsequent machining operations with the purpose to achieve better surface finish and closer tolerances than die cast process allows.

either a mixture of natural sand and clay or synthetic sands. A typical sand casting mould has a gating system, risers and chills.

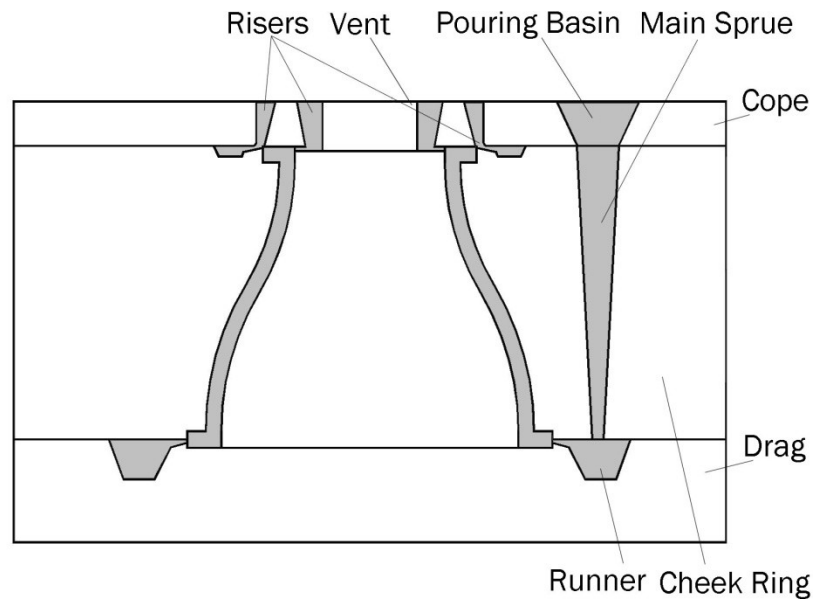


Figure 1.1 Schematic representation of sand casting mould

1.3 Permanent Mould Casting

Permanent mould casting is referred to as a method of casting in which the mould is not destroyed during extraction of the casting. Permanent moulds are capable of producing large number of the same casting. Castings produced in permanent moulds have generally finer grain structure and superior mechanical properties compared with sand castings. Castings also have less gas porosity, major defect of the die-castings.

Permanent mould has the following major components:

1. Gating system, which directs liquid metal into the cavity at a selected rate.
2. Feeding system, which feeds liquid metal to thicker areas of the part during the solidification period.

3. Chills, which complements the feeding system by cooling thicker areas of the part.
4. Venting system, which allows gases to escape during the cavity fill process.

In general, the permanent mould casting is operationally very similar to a sand casting. It employs gravity as a feeding method. In order to ensure proper filling of the casting, sufficient head has to be provided. Position of the gating system, risers, and chill has to allow directional solidification, starting from the areas of the casting away from the gate and moving into the direction of the gates and feeders. Incorrectly designed and positioned gating system will result in a short fill and shrink porosity. Mistakes in the design of the feeding system and chills will result in excessive shrink porosity, or longer dwell time. Incorrectly placed and sized ventilation channels will result in excessive gas porosity in the casting.

There are three major processes that are currently used to produce castings in permanent moulds:

- Gravity casting
- Low-pressure castings
- Counterpressure casting

1.3.1 Gravity Casting

Gravity casting is a basic casting process that uses gravity to fill the cavity of the mould. This process can be used for simply shaped parts that are not going to be used in high stress or leak free applications.

1.3.2 Low-pressure Permanent Mould Casting

Low-pressure permanent mould casting is a process that uses pressure to feed metal in to the cavity. Castings produced by this method have a higher density and lower gas and shrink porosities. Molten metal is fed from the bottom of the cavity through the riser tube under some pressure (0.5 – 0.8 Bar). Advantages of this method are

1. The process can be easily automated, which allows control of metal velocity, reduces the turbulence of the metal flow and minimizes air entrainment.
2. A hermetically sealed furnace minimizes metal oxidation and avoids unwanted inclusions.
3. Metal is fed from the bottom of the bath which allows feeding cleaner metal into the cavity of the mould.
4. Directional solidification to the riser allows feeding metal until the casting is completely solidified. This reduces the amount of shrink porosity.
5. This method allows producing quality casting with thinner walls.
6. High casting yield

1.3.3 Counter-pressure Casting

Counterpressure casting is a method that uses low pressure to feed metal into the cavity from the bottom of the mould, similar to the low-pressure permanent mould casting method. As the cavity is filled with liquid metal, the pressure constantly increases which suppresses the hydrogen precipitation. Counter-pressure permanent mould casting method allows achieving the highest mechanical properties in a casting. The pressurized cavity eliminates shrink porosity without using risers.

1.4 Die Casting

The earliest examples of die casting by pressure injection, as opposed to casting by gravity pressure, occurred in the mid-1800s. A patent was awarded to Sturges in 1849 for the first manually operated machine for casting printing type. The process was limited to printer's type for the next 20 years, but development of other shapes began to increase toward the end of the century. By 1892, commercial applications included parts for phonographs and cash registers, and mass production of many types of parts began in the early 1900s. The first die-casting alloys were various compositions of tin and lead, but their use declined with the introduction of zinc and aluminium alloys in 1914. Magnesium and copper alloys quickly followed, and by the 1930s, many of the modern alloys still in use today became available [1].

The die-casting process has evolved from the original low-pressure injection method to techniques including high-pressure casting (at pressures exceeding 4500 pounds per square inch), squeeze casting, and semisolid die casting. These modern processes are capable of producing high integrity, near net-shape castings with excellent surface finishes.

Alloys of aluminum, copper, magnesium, and zinc are most commonly used for casting (see Table 1.1):

- Aluminium is a lightweight material exhibiting good dimensional stability, mechanical properties, machinability, and thermal and electrical conductivity.
- Copper alloy is a material with high strength and hardness. It has high mechanical properties, dimensional stability, and wear resistance.

- Magnesium is the lightest cast alloy. It is about 4 times lighter than steel and 1.5 times lighter than aluminium. It has a better strength to weight ratio than some steel, iron and aluminium alloys.
- Zinc is the easiest alloy to cast. It can be used to produce castings with 0.5 mm wall thickness.

Table 1.1 Properties of the alloys [2]

	Aluminum	Magnesium	Zinc
Tensile strength, psi x 1000	47	34	41
Yield strength, psi x 100 (0.2 pct offset)	23	23	—
Shear strength, psi x 1000	28	20	31
Fatigue strength, psi x 1000	20	14	7
Elongation, pct in 2 in.	3.50	3.0	10
Hardness (Brinell)	80	63	82
Specific gravity	2.71	1.80	6.60
Weight, lb/cu. in.	0.098	0.066	0.24
Melting point (liquid), °F	1100	1105	728
Thermal conductivity, CG5	0.23	0.16	0.27
Thermal expansion, in./in./°F x 10 ⁶	12.1	15.0	15.2

1.5 Die-cast Process

High-pressure die casting is used for a wide range of applications in all major industries.

Advantages of the aluminum die castings are:

1. High mechanical properties in combination with light weight.
2. High thermal conductivity.
3. Good machinability.
4. High resistance to corrosion.
5. Parts can be produced with no or a limited amount of machining.

6. Parts can be cast with reproducible and close dimensional tolerances.
7. Low scrap rate.
8. High production rate
9. Thin cross sections

Die casting is a precision manufacturing process in which molten metal is injected at high pressure and velocity into a permanent metal mould. There are two basic die-casting processes:

1. Hot chamber process.
2. Cold chamber process.

1.5.1 Hot Chamber Process

In a hot chamber die-cast machine (Figure 1.2), a metal injection system is immersed in the molten metal.

Advantages of hot chamber die-cast process are

1. Cycle time kept to a minimum.
2. Molten metal must travel only a short distance, which ensures minimum temperature loss during cycle time.

The hot chamber process can be used only for alloys with a low melting point (lead, zinc). Alloys with a higher melting point will cause degradation of the metal injection system.

The hot chamber die-cast process has the following steps:

1. Hydraulic cylinder applies pressure on plunger (Figure 1.2).
2. Plunger pushes metal from the sleeve through the gating system into the cavity (Figure 1.3a).

3. High pressure is maintained during the solidification process.
4. After solidification is complete, the die opens (Figure 1.3b).
5. The part is ejected from the cavity (Figure 1.3c).

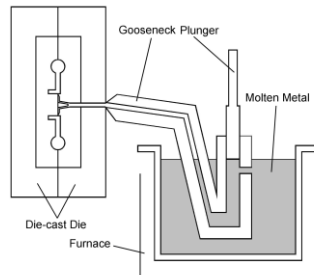


Figure 1.2. Schematic representation of hot chamber die-cast machine

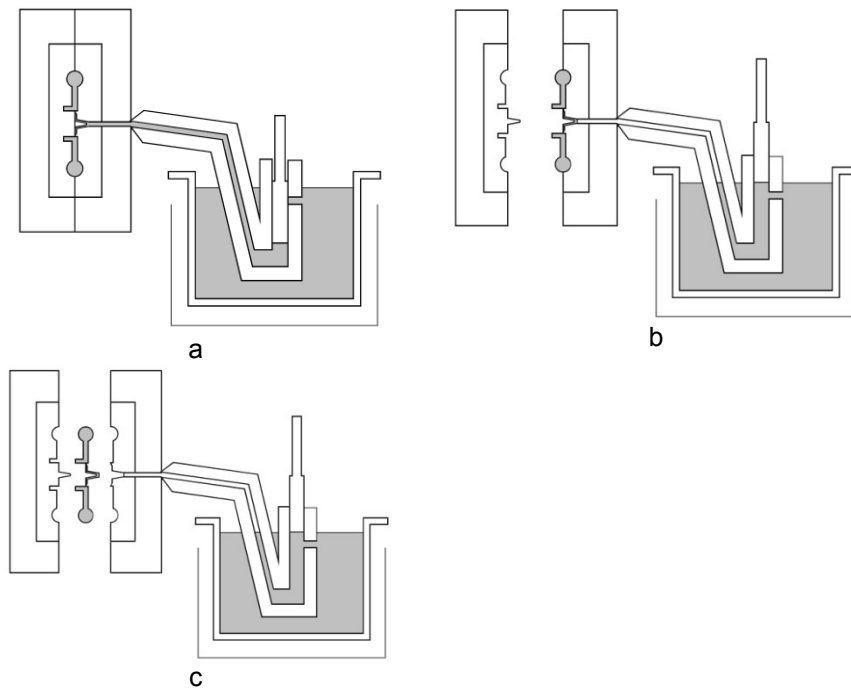


Figure 1.3. Schematic representation of steps in the hot chamber die-cast process: a. plunger pushes metal from the sleeve through the gating system into the cavity; b. after solidification process is complete, the die opens; c. the part is ejected from the cavity.

1.5.2 Cold Chamber Process

The cold chamber die-cast process is used for alloys with a higher melting point (aluminium, magnesium, brass). In a cold chamber die-casting machine (Figure 1.4), the metal is in contact with the machine injection system only for a short period of time.

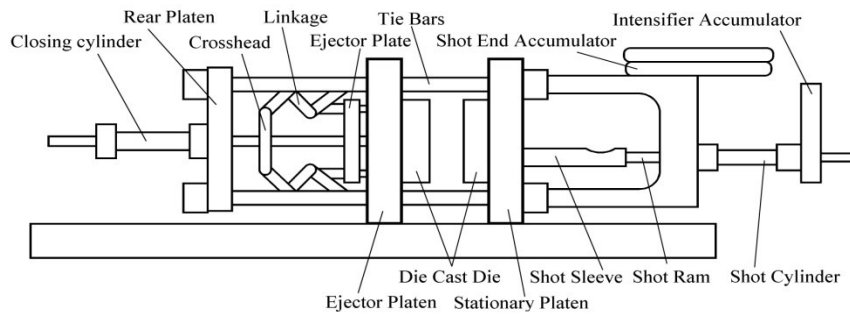


Figure 1.4. Schematic representation of cold chamber die-cast machine

A typical process consists of several steps (Figure 1.5):

1. Molten metal is ladled into the shot sleeve (Figure 1.5a).
2. Hydraulic cylinder applies pressure on the plunger (Figure 1.5b).
3. The plunger pushes metal from the sleeve through the gating system into the cavity (Figure 1.5c).
4. High pressure is maintained during the solidification process (Figure 1.5d).
5. After solidification is complete, the die opens (Figure 1.5e).
6. The part is ejected from the cavity (Figure 1.5f).

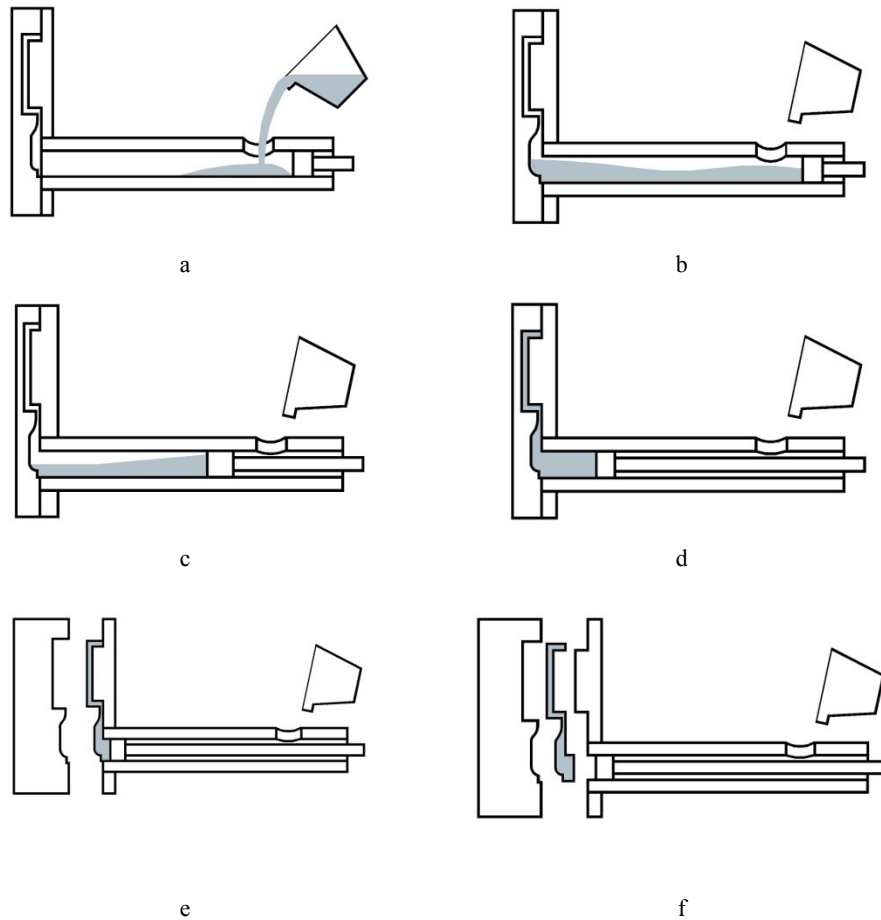


Figure 1.5. Schematic representation of steps in the cold chamber die-cast process: a. molten metal is ladled into the shot sleeve; b. hydraulic cylinder applies pressure on plunger; c. plunger pushes metal from the sleeve through the gating system into the cavity; d. high pressure is maintained during solidification; e. after solidification is complete, the die opens; f. the part is ejected from the cavity.

Disadvantages of the die cast process are:

1. Porosity is the major defect of the die cast process,
2. High cost of the die-cast die.

1.6 Challenges of metal flow in thin cavities

Recent trends in the industry to reduce energy consumption, reduce mass of components, and achieve greater efficiency of the end user products resulted in more complex die-cast parts. Thin wall castings, in combination with new materials, offer weight reduction with

increased strength. Secondary operations like welding and heat treatment have raised quality requirements for these highly engineered castings. In order to achieve the greater structural uniformity, high-efficiency vacuum systems are routinely used on die cast dies. Major problems that increase cost and limit the use of die-cast parts are porosity and blisters. Gas porosity usually results from improperly design flow pattern or cooling system, inadequate size of the ventilation system. High temperature gradients between the molten metal and die-cast die cavity steel require more careful consideration at the process design stage.

Numerical simulations are regularly used nowadays to predict problems during molding and optimize mold design. Flow and thermal analyses in die casting are conducted by commercial software including FLOW3D, EKK and MAGMASOFT. Such numerical analyses help to predict defects of the die cast process such as gas and thermally induced porosities, cold flow, and premature solidification.

Purpose of the present work is to simplify numerical analysis of the liquid metal flow and solidification in a thin cavity by employing the Reynolds's lubrication approximation. Reducing the three-dimensional Navier-Stokes equations to a two-dimensional flow equations based on the Reynolds lubrication approximation allows one to eliminate velocity calculations in the traverse direction. It simplifies computational domain from three dimensions to two dimensions, reduce computational time significantly, and allows one to achieve the solution of the flow and solidification problem much faster with reasonable accuracy.

Chapter 2: Literature Overview

2.1 A Historical Overview of Numerical Methods

Numerical analysis is the area of mathematics that solves differential equations that describe real world problems by numerical approximation. History of numerical approximations can be traced back to 1650 BC when Rhind Papyrus of Egypt used a root-finding method for solving equations [3]. Archimedes of Syracuse in 287-212 BC used numerical methods for calculating lengths, areas, and volumes of geometric figures [4]. Many current numerical approximations are based on a fundamental work of Isaac Newton and Gottfried Leibnitz [4]. Numerical methods for root-finding and polynomial interpolation first introduced by Newton still find wide use in modern algorithms. Contribution of famous mathematicians of 18th and 19th century Euler (1707-1783), Joseph-Louis Lagrange (1736-1813), and Karl Friedrich Gauss (1777-1855) laid the foundation for treating numerical methods as an independent branch of the mathematical science. Beginning of modern numerical analysis can be attributed to work by John von Neumann and Herman Goldstine [5].

In our days, development of new computational platforms as well as development and constant evolution of programming languages allows one to implement more sophisticated, more powerful numerical algorithms. Fortran still remains the most popular programming language for implementing numerical algorithms. Together with other programming languages including C, C++, and JAVA, it allows one to develop new engineering software-based tools for solving rather complex engineering problems. In recent years, programming languages that combine numerical programming and graphical tools have gained popularity. MATLAB© is one of the most popular ways of

doing numerical computations, while Maple© and Mathematica© are the most popular packages used for solving the mathematical problems analytically.

2.2 Finite Difference Method

To find solution of partial differential equation (PDE), computational domain has to be discretized into finite difference grid. Lines that divide computational domain called finite difference grid. Points of intersection of the grid lines called grid points. One of the numerical procedures that solve PDE at the grid points are called finite difference method. After finite difference grid is established, a finite difference approximation has to be developed—it is often done by writing Taylor series at every grid point for the dependant variable. Then the solution of the PDE in terms of the solution of a system of algebraic equations can be found [6].

2.3 Control Volume Method (CVM)

The computational domain is subdivided into a finite number of non-overlapping control volumes by orthogonal but not necessarily uniformly-spaced grid lines. Control volume method (see Figure 2.1) is based on the principal of achieving flux balance in a finite control volume [7]. Algebraic equations are set by achieving the balance of a physical quantity in a control volume. A scalar grid point “P”, located at the center of each control volume, is used for storing values of variables such as pressure and enthalpy. Velocity components are stored at control volume faces. However storage of velocity components are staggered with respect to the faces: velocities ‘u’ are stored at west and east faces, while velocities ‘v’ are stored at north and south faces. So control volume storage for vector quantities are different from the scalar components—this arrangement is used to prevent the estimation of unrealistic results for pressure and velocities.

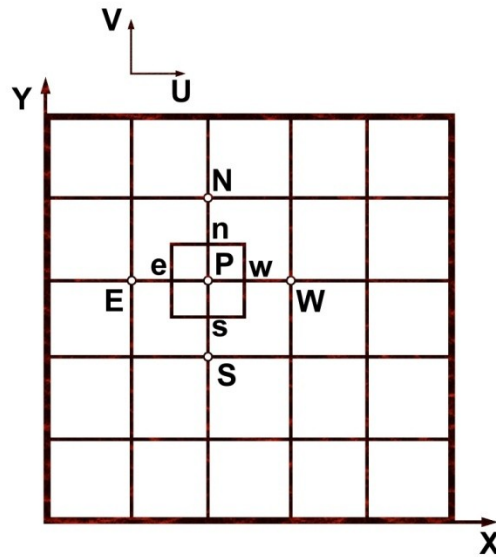


Figure 2.1 Control volume method.

2.4 Free Surface Approximation using a Numerical Technique

2.4.1 Marker and Cell (MAC) Method

Marker and cell method was first introduced in 1965 [8]. The method is based on placing a set of marker particles within a fluid. Particles can move with the fluid but have no volume or mass. Computational cells that contain the marker particles are considered occupied by a fluid. Computational cells without the marker particles are considered empty. Free surface is considered to be in a cell that has a marker particle and borders with at least one empty cell. Advection of a free surface is computed based on movement of the particles with locally-interpolated fluid velocities. A prominent disadvantage of the MAC method is the high usage of CPU time for tracing all marker particles. Other disadvantages include lost ability to track volume and impractical implementation for three dimensional flows.

2.4.2. Surface Marker Method

In an attempt to reduce the CPU and memory requirements of the MAC method, marker particles were placed on a free surface only [9]. This method did improve the computer memory usage.

2.4.3 Free Surface Approximation using Volume of Fluid (VOF) Method

Volume of fluid method [10] (see Figure 2.2) was developed to take advantage of volume tracking capabilities of the MAC method and reduce its CPU memory requirements. In order to minimize storage space, only one of the flow variables (pressure, velocity, temperature) is stored in a single control volume. Following the same methodology, fluid volume fraction is stored in each computational volume. Volume fraction is a step function that can be either zero or one. Free surface is located between completely filled and empty cells. Based on a fraction of fluid in the particular cell, slopes and the curvature of the free surface can be easily computed as well. To compute surface advection in time in 2D, the kinematic equation for fluid fraction can be used:

$$\frac{\partial F}{\partial t} + u \frac{\partial F}{\partial x} + v \frac{\partial F}{\partial y} = 0 \quad (2.1)$$

where F is a fraction of fluid in a cell, u and v are velocities in x and y direction respectively. Volume of fraction method has proven to be a robust and accurate in tracking a free-surface flow [11]. It is a substantially simplified MAC method without any added computational costs.

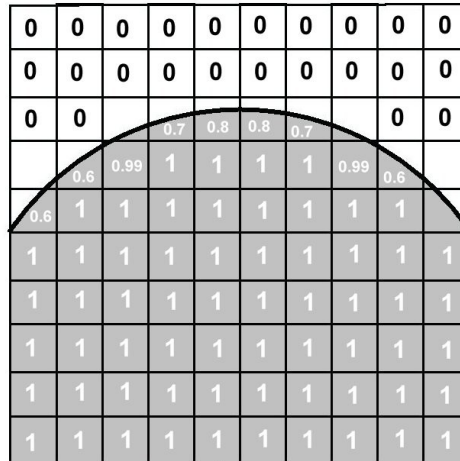


Figure 2.2 Volume of fluid method

2.5 Reynolds's lubrication approximation

In 1886 Osborne Reynolds [12] derived the differential equation governing the pressure distribution in thin film of lubrication. If the cavity is assumed to be thin, and out of plane flow is neglected, the three dimensional problem can be simplified to a two dimensional one. Consider one dimensional Navier-Stokes equation:

$$\rho \left(\frac{\partial u}{\partial t} + u \frac{\partial u}{\partial x} \right) = \mu \frac{\partial^2 u}{\partial z^2} - \frac{\partial p}{\partial x} \quad (2.2)$$

where, ρ , μ , and p are density, viscosity, and pressure respectively.

If we assumed that

- Derivative of u with respect of time is equal to zero,
- Velocity is independent of x and doesn't have y or z component,
- Pressure is hydrostatic in z direction,
- Cavity is assumed to be thin and varying slowly along the x and y directions,
- Inertial forces are much smaller than viscous forces,

then the Navier-Stokes equations, on being integrated along the thickness (z) direction, can then be reduced to the well known Reynolds lubrication equation [13]:

$$\frac{\partial}{\partial x} \left(\frac{h^3}{\mu} \frac{\partial P}{\partial x} \right) + \frac{\partial}{\partial y} \left(\frac{h^3}{\mu} \frac{\partial P}{\partial y} \right) = 6(U_1 - U_2) \frac{\partial h}{\partial x} + 12(V_2 - V_1) \quad (2.3)$$

Here h is the cavity thickness while U_i and V_i are the x and y direction velocities of the upper and lower surfaces. For our case with both the walls of the channel being stationary and no variation in flow in the y direction, Eq. 2.3 reduces to

$$\frac{\partial}{\partial x} \left(S \frac{\partial P}{\partial x} \right) = 0 \quad (2.4)$$

where $S = \frac{h^3}{\mu}$ is flow conductance and P is liquid pressure.

Equation (2.3) indicates that the Navier – Stokes equation is reduced to a lubrication equation under the assumption that inertia effects can be neglected. However in order to implement lubrication equation for numerical analysis of the liquid metal-flow in the thin cavities, the inertia effects cannot be excluded from our consideration due the high thickness-based Reynolds ($\sim 60,000$) number of the process. Hence the lubrication equation with inertia effects coupled with energy equation will be used to numerically compute liquid metal flow with solidification in a narrow channel.

2.6 Scope and objective

In the present work, numerical algorithm for modeling the steady as well as transient flow of liquid metal and its subsequent solidification in a thin cavity is developed. Metal flow happens in a thin ventilation channel at the end of the die cast process. Main purpose of this algorithm is to develop a numerical ability to calculate quickly and with reasonable degree of accuracy how far liquid metal will be able to travel in the ventilation

channel before solidification occurs. It will enable engineers to design die ventilation channels without solving the full Navier-Stokes equation, which takes a long time owing to a very large aspect ratio of the channel geometry, i.e., the channel thickness is in millimeters while the potential length of the liquid metal flow is in tens of centimeters.

Objectives of this thesis proposal are:

1. Develop a 2-D equation set for the flow and solidification of liquid metal in thin cavities using the Reynolds's lubrication approximation
2. Develop a numerical algorithm to analyze steady-state and transient metal flow in the thin channel with solidification
3. Validate our numerical simulation against experimental data

To achieve these objectives, we will present the results in the following two parts: (a) a proof-of-concept study in chapter 3 with a simpler, steady flow of metal in a channel while the skin of solid metal growing on the channel walls, (b) a more advanced, transient flow in the channel in chapter 4 with a moving metal-air interface while the solid-metal skin grows on the walls.

Chapter 3: A fast numerical simulation for modeling simultaneous metal flow and solidification in thin cavities using the lubrication approximation

Abstract: A numerical algorithm for modelling *steady* flow of liquid metal accompanied by solidification in a thin cavity is presented. The problem is closely related to a die cast process and in particular to the metal flow phenomenon observed in thin ventilation channels. Using the fact that the rate of metal flow in the channel is much higher than the rate of solidification, a numerical algorithm is developed by treating the metal flow as steady in a given time-step while treating the heat transfer in the thickness direction as transient. The flow in the thin cavity is treated as two dimensional after integrating the momentum and continuity equations over the thickness of the channel, while the heat transfer is modelled as a one-dimensional phenomenon in the thickness direction. The presence of a moving solid-liquid interface introduces non-linearity in the resulting set of equations, and which are solved iteratively. The location and shape of the solid-liquid interface are found as a part of the solution. The staggered grid arrangement is used to discretize the flow governing equations and the resulting set of partial differential equations is solved using the SIMPLE algorithm. The thickness direction heat-transfer problem accompanied by phase change is solved using a control volume formulation. The results are compared with the predictions of the commercial software FLOW3D[®] which solves the full three-dimensional set of flow and heat transfer equations

accompanied with solidification. The Reynolds's lubrication equations accompanied by the through-the-thickness heat loss and solidification model can be successfully implemented to analyze flow and solidification of liquid metals in thin channel during the die cast process. The results were obtained with significant savings in CPU time.

3.1 Introduction

Global competition for manufacturing superiority has entered a new stage. As economists predicted for quite some time, there is no a single country or a region which can claim absolute world dominance in manufacturing capabilities. Widespread use of numerical analysis software and free exchange of information allow engineers around the world to design, analyze, and bring to manufacture new products in record times. Die cast industry is not an exception. Flow, thermal, and distortion analyses are the integral part of developing die cast process parameters as well as die-cast die design. But due to an increase in complexity of part design, it takes longer to go through the complete numerical analyses cycle; in many cases, it takes several iterations to achieve the desired results.

With the development of faster computers as well as more efficient and accurate numerical approximations, engineers can examine more design options and achieve better results in a much shorter time. However, in spite of the latest advances in numerical simulations, detailed examinations of the flow and solidification inside thin channels remain challenging.

Liquid flow and solidification in channels is a complex phenomenon which gained much attention of researchers in the past few decades. Complexity of the fluid-flow physics and solidification, as well as changes in the flow regime along the length of the channel, create quite a few challenges in the development of numerical algorithms to predict the location and shape of the liquid-solid interface as well as velocity and temperature distributions in the channel. Detailed descriptions of the fluid flow, heat transfer and solidification in the straight channels was conducted by Epstein and Chung [14]. The numerical analysis of fluid flow and solidification in channels requires the solution of the 3D Navier–Stokes equations. The thin cavities with high length-to-thickness aspect ratios require quite a large number of computational cells in order to achieve accuracy and convergence.

Many numerical algorithms were developed to analyze flow and solidification between two parallel plates. In order to simplify the 3D problem, it is reduced into a 2D one, where the original governing equations are converted from the Cartesian coordinate system into the curvilinear coordinates. The numerical model developed by B. Weigand *et. al* [15] successfully solved the two-dimensional Navier-Stokes equation coupled with the heat transfer equation. The numerical analysis of heat transfer during solidification in a channel, in most cases, requires the conversion of the heat conduction equation from the Cartesian coordinates into the curvilinear coordinates as well [16].

Though several numerical methods have been proposed to model solidification of materials in the recent past, not all of them are useful for modelling the flow and solidification in thin channels. For example, a generalized finite difference method was shown to be an efficient technique to model the solidification of metals in [17]. However,

the model was developed for stationary liquid metals and requires a numerical procedure for identification and generation of nodes throughout the computational domain; such a method will be difficult to implement in thin channels as it will require to generate large number of computational nodes. Similarly, a cellular automaton model, used for microscopic modelling of heat transfer and coupled with the finite volume method for macroscopic modelling of solidification process, was introduced by Yao et al. [18]. The model allows for accurate prediction of the solidification parameters in both macro and micro scales. However, the model is implemented for stationary fluids only and requires finite volume discretization in the direction of solidification. A numerical algorithm for modelling two-phase flow was proposed in [19] where forcing terms are added to the Navier-Stokes equations to account for the properties variation between the two fluids. The method doesn't account for the inertia driven flows as well as does not predict solidification, and requires computational discretization of the domain in the direction of the interface between two fluids during advection. In the last few years, several finite-difference and finite-volume based methods have been developed and implemented to model solidification of metals during casting [20-21]. These models concentrate on developing accurate and efficient algorithms to predict temperature distribution during the solidification process. Such models require a large number of computational cells to be generated in the direction of solidification-front motion and do not account for the effects of the inertia driven flow on temperature distribution in the liquid phase.

Another approach is to convert the original 3D governing equations into the depth-averaged equations; this approach is widely used in the shallow-depth fluid-flow models [22-23]. However, these algorithms still require the solution of the turbulence

models. Several turbulence models have been developed to be used with the depth-averaged governing equations [23-26].

Although the above-mentioned approaches simplify the governing equations, the inclusion of turbulence and other details in numerical models requires substantial amount of CPU time to achieve converged solution. Moreover, conversion of the governing equations into curvilinear coordinates in [23-26] creates added complexities in the development of the numerical algorithm.

In this paper, we propose a simpler, less-computationally expensive approach where the three-dimensional problem of flow and solidification in a thin channel is reduced to a two-dimensional one based on the Hele-Shaw approximation [27]. This approach is based on the Reynolds lubrication theory. Fundamental assumption of the lubrication equation is that in thin, slowly-varying cavities with the flow at relatively small Reynolds's numbers, the inertia forces are much smaller than the viscous forces and can be neglected. In such a situation, the three-dimensional Navier-Stokes equation can be reduced to a Reynolds's lubrication equation and used to analyse flows in thin cavities [13]. In spite of its limitations, the Reynolds's lubrication formulation remains the foundation of the numerical analysis in thin cavities.

Owing to the high-speed nature of the die cast process [28], inertia effects in the metal flow cannot be neglected. Some attempts were made to include the influence of inertia in the lubrication equation. For example, validity of integration of the governing equation over a cavity thickness after assuming a parabolic distribution of the velocity was experimentally confirmed [27]. Similarly, the inertia effects in thin-channel flows

were included in the lubrication equation and validity of the altered lubrication equation for a wide range of Reynolds numbers was established [30-31].

In this paper, a numerical solution of flow in a thin cavity using the lubrication approximation along with a control-volume based solidification model will be presented. The staggered grid arrangement is used to discretize the governing equations. Then an iterative SIMPLE algorithm is used to solve the discretized equations for momentum in the centre-line 2D plane within the channel, while another iterative scheme is used to model the out-of-plane solidification.

Before presenting a detailed flow model, several dimensionless parameters have to be examined in order to identify the driving forces controlling the flow in thin channels during the die-cast operation. Relative importance of the inertial forces compared to the surface tension forces can be examined using the Weber number:

$$We = \frac{\rho_l U_0^2 h}{\sigma} \quad (3.1)$$

where, ρ_l , U_0 , h and σ are density of liquid metal, average velocity, height of the channel, and surface tension, respectively.

Using the die-cast aluminium properties listed in Table 3.1 and assuming the average fluid velocity in the ventilation channel to be 1.6 ms^{-1} while taking the channel gap to be 0.0005 m , the corresponding Weber number will be

$$We = \frac{2650 * 1.6^2 * 0.0005}{0.86} = 3.9$$

This value indicates that the initial inertia forces, before the metal flow in the cavity is affected by solidification, are almost two times higher than the surface tension forces.

The ratio between the surface tension and viscous forces has to be studied next. The Capillary number, which represents the ratio of the viscous forces compared to the capillary forces, can be expressed as

$$Ca = \frac{\mu U_0}{\sigma} \quad (3.2)$$

Table 3.1 Properties of A380 aluminium [32]

Metal density (ρ)	2650 [kg m ⁻³]
Heat conduction coefficient (k_s, k_l)	94 [J m ⁻¹ s ⁻¹ K ⁻¹]
Specific heat (C)	938 [J kg ⁻¹ K ⁻¹]
Liquid metal viscosity (μ)	10 ⁻³ [kg m ⁻¹ s ⁻¹]
Solidification point	538 [°C]
Latent heat (L _f)	3.97x10 ⁵ [J kg ⁻¹]

Using the values listed in Table 3.1, the Capillary number can be estimated to be

$$Ca = \frac{10^{-3} * 1.6}{0.86} = 1.86e^{-2}$$

This result indicates that the surface tension forces are two orders-of-magnitude larger than the viscous forces. Evaluation of Eqs.(3.1) and (3.2) lead to the conclusion that *inertial forces dominate the metal flow in thin channels during the die-cast operation.*

3.2 Development of steady-state solution of flow in thin cavity

Metal flow and solidification in a thin channel is a subject of this study. Molten metal is fed from the left of the channel (see Figure 3.1) in positive “x” direction. Flow is induced due a pressure difference between the left side (inlet) and right side (outlet) of the channel. In the present study, it is assumed that a steady flow of metal has been

established before the onset of solidification at the walls. (Such an assumption is justified since the filling of such channels happen within a second.) After a sufficient amount of heat has been extracted from the metal, a solid-liquid interface formed next to the channel walls grows and meets at the centre of the channel. Fluid flow is assumed to feed the solidification front while the heat is being extracted.

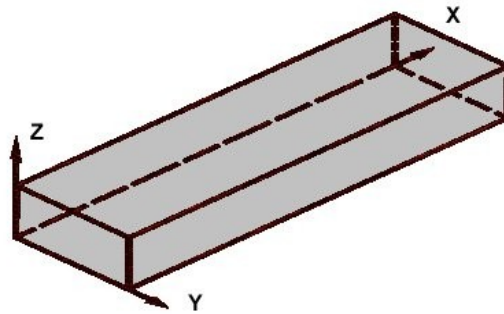


Figure 3.1. Straight channel with a rectangular cross-section: the liquid metal enters from the left-most section in the y - z plane, flows along the x direction, and then exits from the other end.

Both the metal and channel are at superheated temperature initially. The channel walls are suddenly cooled to a temperature below the solidification temperature.

Solidification fronts will be forming near the walls of the channel, propagating inside the molten metal. During solidification, the metal is moving under a pressure-driven flow with a prescribed inlet velocity.

Now we present a comparison of the typical speed with which the metal solidifies versus the speed with which the metal passes through the channel—such a comparison will help us to ignore solidification during the filling of the channel. A typical solidification rate “ S ” inside the horizontal channel can be found [25] using properties of aluminium, shown in Table 3.1 as

$$S = k_s \frac{T_m - T_w}{\rho L_f H_o} \quad (3.3)$$

$$\Rightarrow S = 94 \frac{650 - 10}{2650 * 3.97e^5 * 0.001} = 5.7e^{-2} \frac{m}{s}$$

where, T_m, T_w, L_f, H_o, k_s and ρ - temperature of the metal, temperature of the wall, latent heat of fusion, average height of the channel, heat transfer coefficient, and density of the aluminum, respectively.

Meanwhile the typical rate for metal flow in the channel* without the solid-liquid interface being present is 1 ms^{-1} . The characteristic values clearly show that the rate of solidification is much smaller than the rate of metal flow in the channel. In fact, as the solid-liquid interface converges at the centre of the channel, the rate of metal flow increases, and the ratio of the solidification rate to the flow rate further reduces and goes almost to zero. Based on these conclusions, *we are justified in developing our numerical algorithm for transient solidification in the channel accompanied by liquid-to-solid heat conduction, while treating the metal flow to be quasi-steady.*

The proposed numerical algorithm is developed based on the assumptions, that at time greater than zero, the liquid metal is entering the channel with its temperature above the melting point. Due to their low thermal resistance, the channel walls are assumed to remain at a constant temperature below the melting point to induce solidification. Since the variation in the solid-layer thickness with position along the channel length is small, quasi stable-state can be assumed for the heat conduction in the solid. The liquid-metal temperature is taken to be a constant, while the metal velocity at the channel entrance is

* The typical velocity corresponds to the end of the die cast process, after the main cavity is filled and liquid metal is in the ventilation channel.

considered to be fully developed and steady. All physical properties for both the liquid and solid phases are considered constants.

Problem is applicable to the metal die-cast process involving flow in thin cavities. A brief description of the process is given below. Thin-wall castings, flow in ventilation channels, etc., are some examples where the proposed algorithm can be utilized. The proposed numerical solutions can be used to reduce the number of design iterations employing the full 3D simulation algorithm. One of the ways to reduce the computational time is to reduce a 3-D problem to a 2-D one. In the present case, the die-cast mold cavity is thin and hence the flow in the vertical direction is neglected. Assumption of negligible inertial forces allows one to reduce the Navier-Stokes equations to the Reynolds lubrication approximation. But such an approximation is valid only for small Reynolds numbers. A major characteristic of the die casting process is metal flow under high pressure and velocity, and since the Reynolds numbers can achieve quite high values, the inertia effects cannot be neglected. Hence a modified lubrication approximation after including the inertial effects is employed to predict the thickness-averaged in-plane flow in the die-cast mould.

The presented algorithm considers the thickness-averaged 2-D steady-state flow in a die-cast mold in the in-plane directions and 1-D along-the-thickness transient heat-transfer. A set of nonlinear partial differential equations is developed to solve for flow which are then discretized using the finite difference scheme after employing the SIMPLE algorithm. A direct control-volume based formulation is proposed to model heat transfer and solidification along the thickness direction. The two sets of equations are solved in an iterative manner using Matlab and the obtained results are validated by

comparing with the ones achieved using the commercial software FLOW3D², where the control volume method is used to discretize the governing equations while the enthalpy method is used to estimate temperature distribution in the cavity.

3.3 Governing equations

We are considering a three-dimensional flow in a straight channel with rectangular cross-section as shown in Figure 3.1. The flow is considered to be incompressible, viscous, and Newtonian. Due to the fact that the rate of metal flow in the channel is much higher than the rate of solidification, a steady-state flow at a given time-step with transient heat conduction from liquid into solid is assumed. Since the inertial effects characterized by high Reynolds's number are dominant in the flow, so the gravitational forces are neglected. The governing equations are expressed in the Cartesian coordinate system with x coordinate in the direction of flow (along the cavity length), y in the direction normal to the flow (along the cavity width), and z in the direction transverse to the x - y plane (along the cavity height); u , v , and w are the corresponding velocities. The governing equations used are the continuity, momentum, and energy equations in the liquid and solid phases with momentum and energy boundary conditions specified at the channel walls, inlet, and outlet as well as at the solid-liquid interface. Location and shape of the solid-liquid interface is found as a part of the solution of the

² FLOW3D® [33] is a general purpose commercial CFD software which solves three-dimensional fluid-flow and solidification problems using the finite different approximation. FLOW3D utilizes the Volume-of-Fluid technique and the FAVOR method to track free surfaces as well as solid-liquid interfaces. The two equation k - ϵ model is used to resolve the turbulent properties of the flow. The averaged Navier–Stokes equations coupled with the energy equation allow the software to achieve an accurate solution for turbulent metal flow undergoing solidification.

presented algorithm. The steady-state conservation equations governing the transport of mass, momentum and energy are expressed as follows.

Liquid region

Continuity equation:

$$\frac{\partial u}{\partial x} + \frac{\partial v}{\partial y} + \frac{\partial w}{\partial z} = 0 \quad (3.4)$$

Momentum balance equations:

$$\rho \left(u \frac{\partial u}{\partial x} + v \frac{\partial u}{\partial y} + w \frac{\partial u}{\partial z} \right) = \mu \left(\frac{\partial^2 u}{\partial x^2} + \frac{\partial^2 u}{\partial y^2} + \frac{\partial^2 u}{\partial z^2} \right) - \frac{\partial p}{\partial x} \quad (3.5a)$$

$$\rho \left(u \frac{\partial v}{\partial x} + v \frac{\partial v}{\partial y} + w \frac{\partial v}{\partial z} \right) = \mu \left(\frac{\partial^2 v}{\partial x^2} + \frac{\partial^2 v}{\partial y^2} + \frac{\partial^2 v}{\partial z^2} \right) - \frac{\partial p}{\partial y} \quad (3.5b)$$

$$\rho \left(u \frac{\partial w}{\partial x} + v \frac{\partial w}{\partial y} + w \frac{\partial w}{\partial z} \right) = \mu \left(\frac{\partial^2 w}{\partial x^2} + \frac{\partial^2 w}{\partial y^2} + \frac{\partial^2 w}{\partial z^2} \right) - \frac{\partial p}{\partial z} \quad (3.5c)$$

Energy balance equation:

In differential form, the energy balance equation is expressed as

$$\rho C \frac{\partial T}{\partial t} + \rho C \vec{v} \cdot \nabla T - \nabla \cdot \vec{q} = 0 \quad (3.6)$$

where, C , T , t , and q are specific heat, temperature of the metal, time, and heat flux, respectively.

Solution of the governing equations (3.4) to (3.6) presents several problems. To begin with, the convective terms in the left hand side of Eq. (3.5) are non-linear. All equations are coupled because velocity components are present in each equation. On comparing the

rate of solidification (see Eq. 3.3) to the rate of flow, one can define a solidification parameter as

$$\Delta_s = \frac{S}{u} \quad (3.7)$$

Based on the flow and solidification characteristic of the presented problem and the characteristic x-direction velocity of $u=1\text{m/s}$, the solidification parameter in our case will be

$$\Delta_s = \frac{0.0518}{1.0} = 0.0518$$

Metal flowing in thin channels is affected by solidification, which results in the presence of a growing solid-liquid interface next to the cooler channel wall. As the time progresses, the solid-liquid interfaces from the two walls converge at the centre of the channel; in other words, a progressive reduction of the effective channel gap h . When $h \rightarrow 0$, the conservation of mass of the flowing metal indicates that $u \rightarrow \infty \Rightarrow \Delta_s \rightarrow 0$. In this limit when $\Delta_s \rightarrow 0$, the effect of solidification in terms of momentum transfer on the metal flow is negligible, and hence the velocity field can be uncoupled from the temperature field [31]. In other words, we can use the zero velocity at the interface to model the metal flow while the energy equation is used to estimate the channel gap.

In order to further simplify the governing equations, we conducted an order-of-magnitude analysis to determine the importance of each term on the flow characteristics. Under this, the dimensionless variables were defined as

$$\begin{aligned}
\tilde{x} &= \frac{x}{L}, \tilde{y} = \frac{y}{L}, \tilde{z} = \frac{z}{H_o}, \tilde{h} = \frac{h}{H_o}, \theta = \frac{T - T_m}{T_w - T_m}, \tilde{t} = \frac{t}{\tau} \\
\tilde{u} &= \frac{u}{\bar{V}}, \tilde{v} = \frac{v}{\bar{V}}, \tilde{w} = \frac{w}{\bar{W}} = \frac{Lw}{\bar{V}H_o}, \tilde{p} = \left(\frac{H_o}{L}\right)^2 \frac{L}{\mu\bar{V}} p \\
\tilde{s} &= \frac{s}{H_o}
\end{aligned} \tag{3.8}$$

where, tildes designate dimensionless quantities, L , θ , τ , \bar{V} , \bar{W} , and s are length of the channel, dimensionless temperature, reference time, reference velocity in x and y direction, reference velocity in z direction $\left(= \bar{v} \frac{H_o}{L}\right)$ and location of the solid-liquid interface, respectively.

Owing to a small aspect ratio of the cavity height to its length and width, length and width of the cavity are considered on the same order of magnitude and will be denoted by L along both x and y. For notational convenience, the tildes are dropped from non-dimensional variables.

On non-dimensionalizing the continuity equation, Eq. (3.4), we get

$$\frac{\bar{V}}{L} \frac{\partial u}{\partial x} + \frac{\bar{V}}{L} \frac{\partial v}{\partial y} + \frac{\bar{W}}{H_o} \frac{\partial w}{\partial z} = 0 \tag{3.9}$$

Multiplying all terms of Eq. (3.9) by L/\bar{V} will result in

$$\frac{\partial u}{\partial x} + \frac{\partial v}{\partial y} + \frac{\bar{W}}{H_o} \frac{L}{\bar{V}} \frac{\partial w}{\partial z} = 0 \tag{3.10}$$

We have to define the characteristic velocity in z direction. In order to insure that all the terms of Eq. (3.10) are on the same order of magnitude, the characteristic velocity in z direction is defined as:

$$\frac{\bar{W}}{H_o} \frac{L}{\bar{V}} = 1 \Rightarrow \bar{W} = \bar{V} \frac{H_o}{L} \quad (3.11)$$

Eq. (3.11) indicates that the characteristic velocity in z direction is much smaller than those in x and y directions, i.e., $\bar{W} \ll \bar{V}$ because $H_o \ll L$. After absorbing this conclusion, the resultant non-dimensional continuity equation, Eq.(3.10), reduces to

$$\frac{\partial u}{\partial x} + \frac{\partial v}{\partial y} + \frac{\partial w}{\partial z} = 0 \quad (3.12)$$

Substitution of dimensionless variables in the momentum balance equations, Eq. (3.5),

leads to

$$\rho \frac{H_o^2 \bar{V}}{L\mu} \left(u \frac{\partial u}{\partial x} + v \frac{\partial u}{\partial y} + w \frac{\partial u}{\partial z} \right) = \frac{\partial^2 u}{\partial z^2} + \frac{H_o^2}{L^2} \left(\frac{\partial^2 u}{\partial x^2} + \frac{\partial^2 u}{\partial y^2} \right) - \frac{\partial p}{\partial x} \quad (3.13a)$$

$$\rho \frac{H_o^2 \bar{V}}{L\mu} \left(u \frac{\partial v}{\partial x} + v \frac{\partial v}{\partial y} + w \frac{\partial v}{\partial z} \right) = \frac{\partial^2 v}{\partial z^2} + \frac{H_o^2}{L^2} \left(\frac{\partial^2 v}{\partial x^2} + \frac{\partial^2 v}{\partial y^2} \right) - \frac{\partial p}{\partial y} \quad (3.13b)$$

$$\rho \frac{H_o^4 \bar{V}}{L^3 \mu} \left(u \frac{\partial w}{\partial x} + v \frac{\partial w}{\partial y} + w \frac{\partial w}{\partial z} \right) = \frac{H_o^2}{L^2} \frac{\partial^2 w}{\partial z^2} + \frac{H_o^4}{L^4} \left(\frac{\partial^2 w}{\partial x^2} + \frac{\partial^2 w}{\partial y^2} \right) - \frac{\partial p}{\partial z} \quad (3.13c)$$

Due to the small cavity aspect ratio, i.e. $\frac{H_o}{L} \ll 1$, all terms on the order $\frac{H_o^2}{L^2}$ or higher

can be neglected. Then the in-plane momentum balance equations result in

$$\rho \frac{H_o^2 \bar{V}}{L\mu} \left(u \frac{\partial u}{\partial x} + v \frac{\partial u}{\partial y} + w \frac{\partial u}{\partial z} \right) = \frac{\partial^2 u}{\partial z^2} - \frac{\partial p}{\partial x} \quad (3.16a)$$

$$\rho \frac{H_o^2 \bar{V}}{L\mu} \left(u \frac{\partial v}{\partial x} + v \frac{\partial v}{\partial y} + w \frac{\partial v}{\partial z} \right) = \frac{\partial^2 v}{\partial z^2} - \frac{\partial p}{\partial y} \quad (3.16b)$$

while the momentum equation in the direction transverse to the flow reduces to

$$0 = \frac{\partial p}{\partial z} \quad (3.17)$$

Eq. (3.17) indicates that the fluid pressure is uniform in the z direction regardless of the inertia effects in the flow and hence, the pressure is $p = f(x, y, t)$ regardless of the high- Re character of the flow.

Previous work on high-speed flow in thin channels [29] has assumed a parabolic distribution of flow velocities. We also will assume a parabolic distribution of velocity along the x and y directions for further analysis:

$$u = U(x, y)(z^2 - zh) \quad (3.20a)$$

$$v = V(x, y)(z^2 - zh) \quad (3.20b)$$

On being integrated over the thickness of the channel, the continuity equation, Eq. (3.12), becomes

$$\frac{\partial U}{\partial x} + \frac{\partial V}{\partial y} = 0 \quad (3.21)$$

Note that based on the no-penetration boundary condition on top and bottom, and the small cavity size in z the direction, “ w ” velocity variation is negligible and is set to zero

(i.e., $\frac{\partial w}{\partial z} = 0$).

On non-dimensionalizing Eq.(3.16), the in-plane two-dimensional momentum equations are expressed as

$$\begin{cases} \delta \left(U \frac{\partial U}{\partial x} + V \frac{\partial U}{\partial y} \right) = \frac{\partial^2 U}{\partial z^2} - \frac{\partial P}{\partial x} \\ \delta \left(U \frac{\partial V}{\partial x} + V \frac{\partial V}{\partial y} \right) = \frac{\partial^2 V}{\partial z^2} - \frac{\partial P}{\partial y} \end{cases} \quad (3.22)$$

After integrating Eq.(3.22) across the cavity thickness from 0 to h , the momentum equations become³

$$\frac{\delta}{30} h^4 \left(U \frac{\partial U}{\partial x} + V \frac{\partial U}{\partial y} \right) + \frac{\delta}{6} \left(U^2 \frac{\partial h}{\partial x} + UV \frac{\partial h}{\partial y} \right) h^3 = 2U - \frac{\partial p}{\partial x} \quad (3.23a)$$

$$\frac{\delta}{30} h^4 \left(U \frac{\partial V}{\partial x} + V \frac{\partial V}{\partial y} \right) + \frac{\delta}{6} \left(UV \frac{\partial h}{\partial x} + V^2 \frac{\partial h}{\partial y} \right) h^3 = 2V - \frac{\partial p}{\partial y} \quad (3.23b)$$

where, $\delta = \varepsilon^2 Re$ modified Reynolds number, ε as a cavity aspect ratio $\left(= \frac{H_0}{L} \right)$

and Re as a Reynolds number with the $\left(= \frac{\rho \bar{V} H_0}{\mu} \right)$.

For a detailed derivation of the equation set Eq.(3.23), see Appendix A (Appendix A shows the derivation of the equations for the transient-flow case. Derivation of the steady-state flow equations, Eq. (3.23), is the same, except for the absence of the transient term).

Energy equation

A general balance equation for energy is developed for the arbitrary control volume shown on Figure 3.2. On integrating the conservative form of Eq. (3.6) over the control volume after neglecting variations in fluid properties and velocity, we get

$$\iiint_{CV} \left\{ \frac{\partial}{\partial t} (\rho CT) + \nabla \cdot (\rho CT \vec{v}) - \nabla \cdot \vec{q} \right\} dV = 0 \quad (3.24)$$

On rewriting the last two terms of Eq. (3.24) as surface integrals, the energy balance equation over the fixed control volume changes to

³ Derivation of the Eq. 3.23 is for two dimensional variation of the cavity thickness “h”. The second term of the equations has denominator of 6 instead of 12 in [12].

$$\frac{\partial}{\partial t} \iiint_{CV} \rho CT dV = - \iint_{CS} \rho CT \vec{v} \cdot \hat{n} dA + \iint_{CS} \vec{q} \cdot \hat{n} dA \quad (3.25)$$

The control volume can be treated as an open system that exchanges heat with its surroundings and where mass can flow in and out, hence Eq. (3.25) represents the energy balance that can be described as: Rate of heat accumulation in control volume = net rate of heat transport into control volume (by fluid flow) - net rate of heat transferred out of control volume to surrounding through conduction. Note that due to high Peclet numbers (45) involved in this problem, the energy transfer between the fluid metal and the channel wall, or between the fluid and solidified metal, is driven by convection; the heat transfer through the liquid metal is taken to be purely convective as well. The conduction terms are ignored.

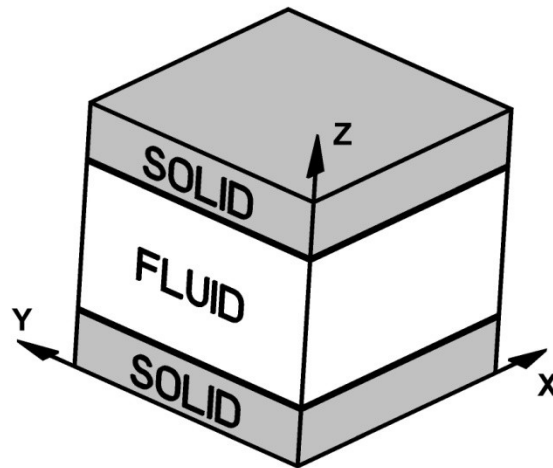


Figure 3.2. A typical control volume, defined around the nodes of the mid-level x-y plane, is used to model the z-direction heat loss and subsequent solidification, in the thin cavity.

Boundary and initial conditions

At the initial time $t = 0$, the same uniform temperature, $T = 650^\circ\text{C}$, is applied to liquid metal lying within the computational domain. At the entrance ($x = 0$), the fluid temperature is set as $T = 650^\circ\text{C}$. At the solid-liquid interface, $T_s = T_l = T_{melt}$. The wall temperatures at $z = 0$ and $z = h$ are set to 10°C . The flow is driven by a uniform velocity imposed at $x=0$ location. The outflow boundary condition specified at the end of the cavity, $x=L$, is $\frac{\partial u}{\partial x} = 0$. The no-slip boundary conditions are applied at the walls.

Additionally, a no-penetration boundary condition, in the form of the velocity gradient in the direction normal to the wall being equal to zero (i.e., $\frac{\partial v}{\partial y} = 0$), is applied. An additional condition is needed to express the velocity of the moving solid-liquid interface as a function of heat transfer in both the solid and liquid phases. This is called the Stefan condition and can be expressed [30] as

$$\rho L f \frac{ds}{dt} = k_s \left. \frac{\partial T_s}{\partial x} \right|_{x=s(t)} - k_l \left. \frac{\partial T_l}{\partial x} \right|_{x=s(t)} \quad (3.26)$$

where, k is heat transfer coefficient, subscripts s and l are designate solid and liquid metal, respectively.

In order to establish the validity of Eqs. (3.21), (3.23) and (3.25) that form the governing equations for the presented problem, they were solved numerically and the results were compared with the solution of the incompressible Navier – Stokes equations fully-coupled with the three-dimensional energy equation during solidification that was solved using the commercial software FLOW3D.

3.4 Solution procedure

The system of dimensionless equations, Eqs.(3.21)-(3.23), and Eq.(3.25) gives a

complete mathematical formulation of the presented problem of liquid-metal flow and solidification in a thin channel. The solution involves determination of velocity and temperature distribution in the liquid phase, as well as the temperature distribution in the solid phase, of the thin channel. The governing equations in a liquid phase are coupled through the interface (Stefan) condition, Eq.(3.26). The solution of the Stefan condition gives the location of the solid-liquid interface as a function of time and position along the length of the channel.

The problem is solved in a straight channel of rectangular cross-section shown in Figure 3.1. A uniform velocity is applied at the $x=0$ location to drive the flow. Constant temperatures are specified at $z=0$ and $z=h$ walls, while the walls at $y=0$ and $y= y_{\max}$ are considered adiabatic. Owing to the weak coupling between the momentum and energy equations, the temperature distribution within the computational domain can be solved first. This establishes the location and shape of the solid-liquid interface, and thus defines the boundaries of the liquid domain. Momentum equations are then solved using the SIMPLE [7] procedure where the momentum and continuity equations are solved in a coupled manner. The momentum equation, Eq (3.23), uses the guessed pressure field and solves for the preliminary velocities U and V . Then the modified continuity equation, Eq (3.21), is used to calculate the corrected value of the pressure field:

$$\frac{\partial P}{\partial t} + a^2 \left(\frac{\partial U}{\partial x} + \frac{\partial V}{\partial y} \right) = 0 \quad (3.27)$$

In the usual incompressible form, the mass conservation or the continuity equation does not have any pressure term. An artificial compressibility term “ a ” has to be added to the

modified continuity equation, Eq.(3.27), to allow for a solution of P. The usual values are $0.1 > a > 1.2$ —it is taken to be 0.8 [38] in the present algorithm.

Solution procedure is described in Figure 3.3, and can be broken down as follows:

1. Guess pressure values in the first time step.
2. Solve the momentum equation to estimate the preliminary values of the u and v velocity components.
3. Use the modified continuity equation, Eq. (3.27), to correct the pressure values.
4. Correct velocities using the new pressure value and continue iterating until the continuity Eq. (3.21) is satisfied.

At this point of analysis, height “ h ” of the channel in the momentum equations still remains unknown. In the absence of solidification, “ h ” is equal to the channel height, and the momentum and continuity equations alone will allow us to estimate the velocity and pressure distributions in the channel. In order to close the system of governing equations, the energy balance equation has to be solved to find temperature distribution in the channel. Based on the result of the energy equation and using Stefan condition, Eq. (3.26), location of the solid-liquid interface can be established for every particular time step. On knowing the location of the solid-liquid interface, “ h ” value can be updated and used in the momentum equation for the next time step. It is assumed that there is a perfect contact between the solidified metal and walls of the channel. Walls of the channel are assumed to have high thermal mass and conductivity, and therefore, their temperatures remain constant during the calculation procedure.

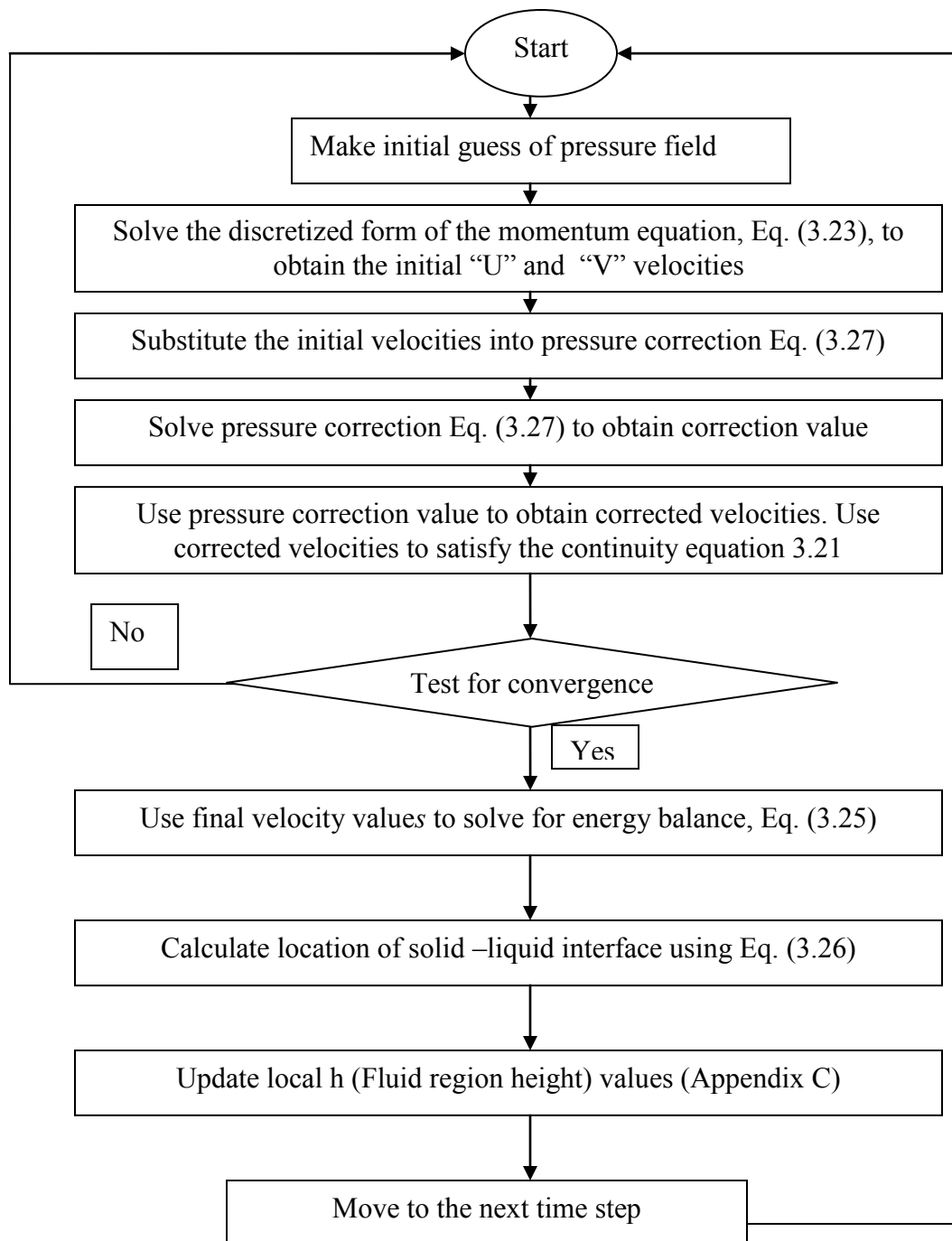


Figure 3.3 Flow chart for the solution algorithm

Note that the momentum equations were solved in dimensionless form while the energy equation was solved in dimensional form.

3.5 Results

Governing equations were solved as indicated in section 3.4 (Solution procedure). The material properties used in the results presented in this section are shown in Table 3.1.

The proposed algorithm is verified for flow and solidification in a straight channel of a rectangular cross-section (Figure 3.1). At the initial time step itself, the flow is considered fully developed. Flow is driven by a uniform axial velocity imposed at the entrance of the cavity at $x=0$. At the time $t=0$, metal temperature is considered to be 600°C and a uniform temperature of 10°C is applied to the top and bottom of the cavity (z direction). At the inflow boundary, the metal temperature is set to a constant 600°C . Analyses were run for 1s. Velocity, temperature distribution, and location of solid—liquid interface were plotted at three locations. Velocity $u=1\text{m/s}$ was applied at $x = 0$ location. Proposed algorithm was verified against results obtain using the commercial software FLOW3D which simulated a fully-coupled three-dimensional flow analysis with solidification.

Channel (Figure 3.1) dimensions are $10 \times 1 \times 0.1$ (mm) in the x , y , and z directions, respectively. Grid independence was insured by comparing 2-D results⁴ of the analysis with grid densities 100×10 , 200×20 , 300×30 , 400×40 , 500×50 , 600×60 shown in Figure 3.4. Since the difference between 500×50 and 600×60 results are less than 0.1%, the analyses were conducted originally with 500×50 grid. In order to reduce angularity in the

⁴ The mesh densities are for solving the z -averaged velocity fields along x and y directions

interface-location plots, the mesh density along the thickness z-direction was later taken to be 150 grid points.

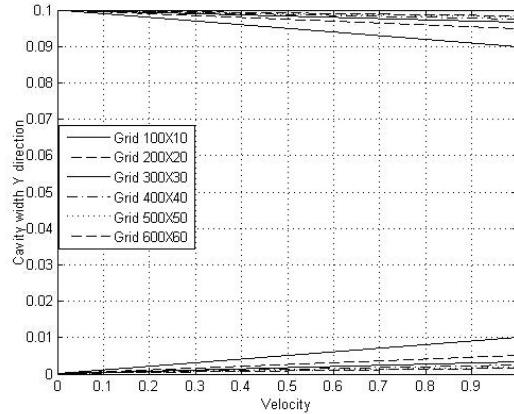


Figure 3.4. Grid independence study conducted at $z=0.5$ plane. [The cavity width in y direction was non-dimensionalized as y/L , Eq(3.8), after using the length of the cavity as $L=0.01\text{m}$. The velocity was rendered dimensionless as u/\bar{v} , Eq(3.8), after employing the characteristic velocity value of $\bar{v}=1\text{ m/s}$.]

The governing equations, Eqs. (3.21) and (3.23), were solved using the algorithm described in the last section. Convergence of the solution was judged by the maximum change in each variable values during each iteration. The solution was considered converged when changes in a dimensionless variables value was less than 10^{-8} .

To verify analyses obtained using the presented algorithm, three-dimensional flow and solidification solutions from the commercial CFD code FLOW3D were obtained using the same boundary and initial conditions. Presented results include fluid velocity, temperature distribution, as well as location of the solid-liquid interface. Three control points along the x direction at dimensionless locations $x = 0.2$, $x = 0.5$, and $x = 0.9$ were chosen for the plots of z -averaged velocities based on the solidification patterned observed in the cavity.

Results presented in Figures 3.5a, 3.5b, and 3.5c show velocity variation along the cavity length where the velocities predicted by our program are compared with the velocities predicted by FLOW3D. We observe that a fairly close flow-prediction is made by our simulation based on the lubrication approximation. We also observe that the x-direction velocity increases with x .

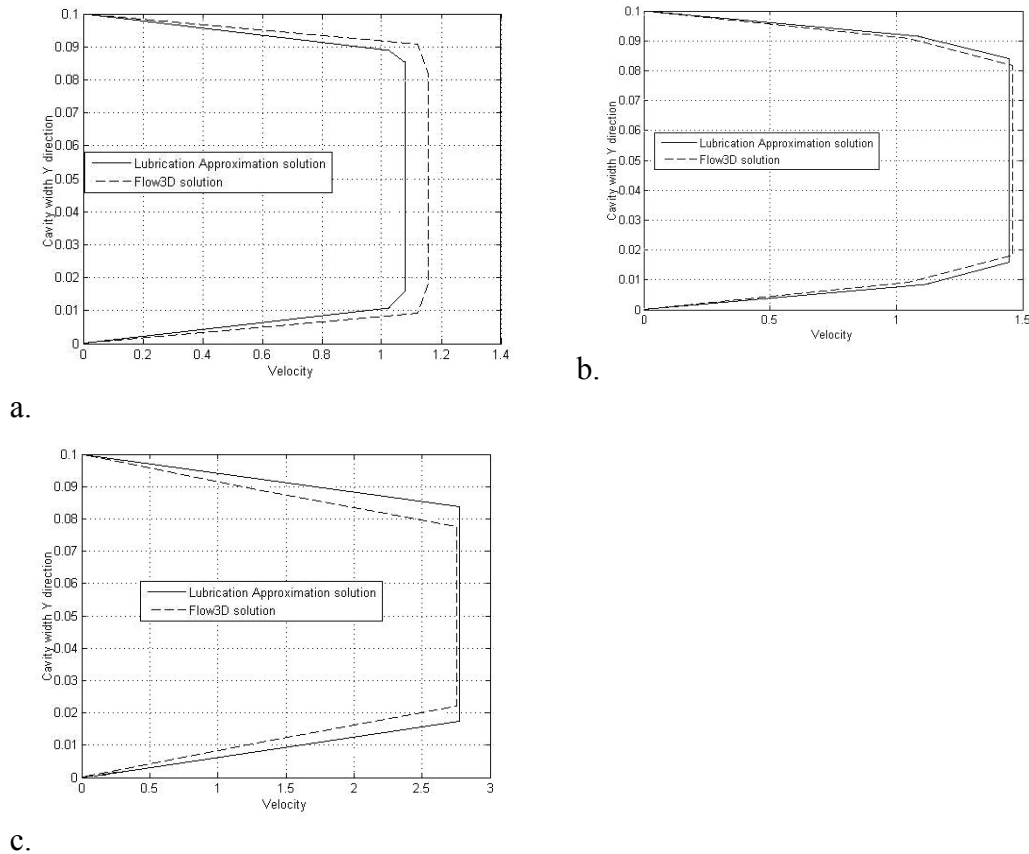


Figure 3.5. Velocity distribution; a) Velocity distribution at $x=0.2$, b) Velocity distribution at $x=0.5$, c) Velocity distribution at $x=0.9$ [The cavity width in y direction was non-dimensionalized as y/L , Eq(3.8), after using the length of the cavity as $L=0.1\text{m}$. The velocity was rendered dimensionless as u/\bar{v} , Eq(3.8), after employing the characteristic velocity value of $\bar{v}=1\text{m/s}$.]

Temperature distribution shown in Figures 3.6a, 3.6b, and 3.6c are plotted at the same locations as used for Figure 3.5. Temperature distribution, as it falls below liquidus temperature or melting point of Aluminium (Table 3.1), suggests the presence of solid-

liquid interface some distance away from the cavity wall. Moving solid-liquid interface reduces cavity height, and as a result, causes an increase in the melt velocity (Figure 3.5) due to conservation of mass.

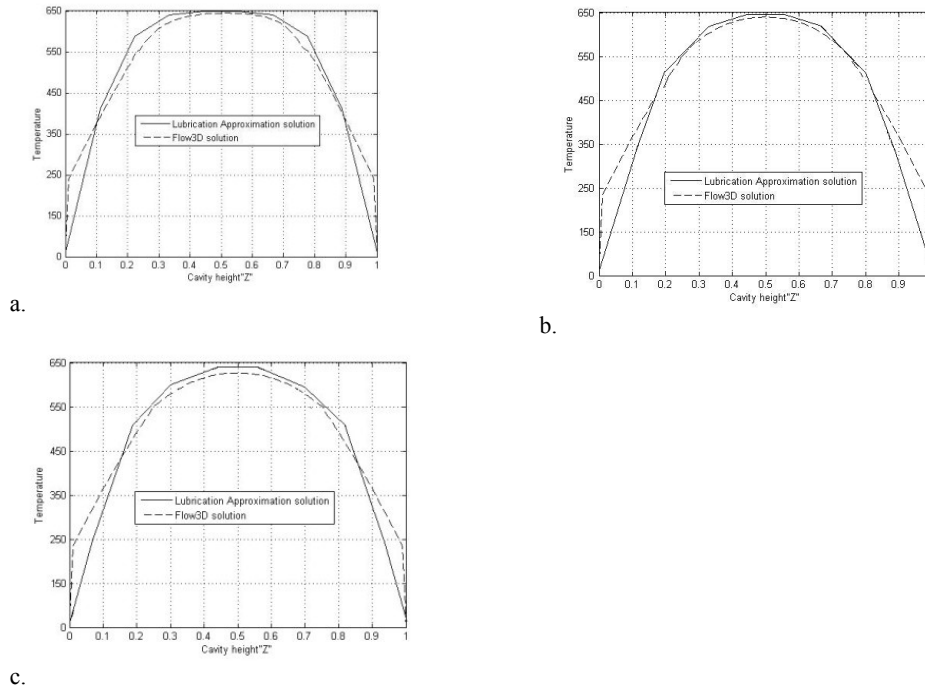


Figure 3.6. Temperature distribution along the cavity thickness at time=1s: a) Temperature distribution at $x=0.2$; b) Temperature distribution at $x=0.5$; c) Temperature distribution at $x=0.9$. Coordinate in the z direction was non-dimensionalized as z/H_o , Eq(3.8), while using $H_o = 0.0001\text{m}$ as the cavity thickness.

Evolution of the solid-liquid interface along the channel length is shown using Figures 3.7a and 3.7b. We note that some discrepancy exists between the lubrication approximation solution and the Flow3D solution in the beginning. However, we achieve a better convergence of results as the time increases. The difference in the results may be attributed to the turbulent nature of the flow employed in FLOW3D simulation: as the channel height decreases, turbulence is less prevalent in the flow, and the results predicted by the presented algorithm are closer to the FLOW3D solution.

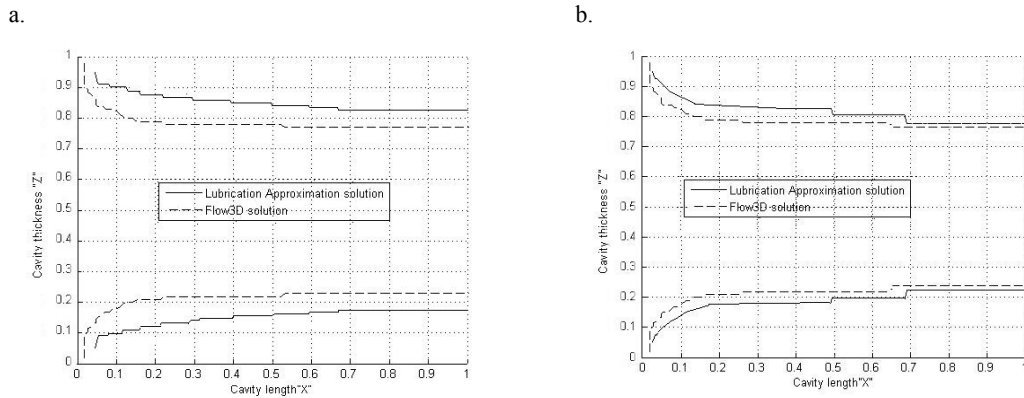


Figure 3.7. Evolution of the solid–liquid interface with time for $u=1$: a) The interface location at $t=0.5s$, b) The interface location at $t=1s$. [The cavity length in x direction was non-dimensionalized as x/L , Eq(3.8), after using the length of the cavity as $L=0.1m$. Coordinate in the z direction was non-dimensionalized as z/H_o , Eq(3.8), while using $H_o = 0.001m$ as the cavity thickness.]

At the specified x locations, differences in the position of the solid—liquid interface are significant enough to cause visible velocity differences in Figure 3.5. As the above given discussion indicates, velocity changes caused by the reduction in cavity height “ h ” corresponds nicely with the changes in velocity estimated by FLOW3D. All results are within 10% of the solution obtained by running three- dimensional analyses utilizing the commercial software FLOW3D.

A significant computational advantage is achieved through a dramatic reduction in CPU time. Owing to the simplification of the governing equations using the lubrication approximation, the CPU time for the proposed algorithm was observed to be 20s. In contrast, the CPU time for the corresponding three-dimensional analysis with FLOW3D software was 12 min. This 36 fold reduction in CPU time clearly demonstrates that the proposed algorithm based on reduced physics is quite fast without a significant sacrifice in the accuracy.

3.6 Conclusion

Results of the presented analyses indicate that Reynolds lubrication approach can be successfully implemented to investigate the flow and solidification of the molten metal in thin cavities during the die cast process. The proposed 2.5D algorithm allows one to estimate the thickness-averaged liquid-metal velocity in the plane of the cavity using the finite difference method; then a finite-volume based algorithm allows one to estimate temperature distribution along the thickness direction as well as location of the solid—liquid interface. The numerical simulation based on the algorithm is verified by comparing its predictions with the solution of the three-dimensional Navier-Stokes equation fully coupled with three dimensional energy equation as predicted by the commercial software FLOW3D[®]. Results indicate that the proposed simulation is fairly accurate in predicting the averaged velocity fields, temperatures along the thickness, and gap thicknesses inside the cavity. Considering small error and significant savings in computational time, the proposed algorithm can be used to reduce time on the initial stages of process development of the die-cast process. It will expedite flow analysis of the die casting process by using the presented algorithm in cases where the high aspect ratio of the thin cavity requires large number of the computational cells to achieve the converged solution. It can be especially useful in analyzing fluid flow and solidification in ventilation channels of the die-cast die.

Chapter 4: A Fast Simulation of Transient Metal Flow and Solidification in a Narrow Channel

Abstract: A fast numerical algorithm for modelling the *transient* flow and solidification of liquid metal in a narrow gap is presented. The problem is closely related to the die-cast process, and in particular to metal flow in thin ventilation channels. After integrating over the channel thickness and employing the lubrication approximation, the Navier-Stokes equations are reduced to 2-D equations for modelling the in-plane flow. The flow model is solved along with a heat balance equation after including the effects of solidification in a control volume. The flow variables and temperature distribution are solved in three stages. In step one, commercial software FLOW3D® is utilized to solve 3-D Navier-Stokes equations coupled with the heat balance equation for flow and solidification in the main cavity. In step two, the flow and heat transfer variables from the main model are transferred as the entrance boundary condition for the proposed numerical simulation. And finally in step three, the metal flow and solidification in a thin channel is modelled using the 2-D equations coupled with the 1-D heat balance equation. Since the solid-liquid interface introduces non-linearity in the flow, the 2-D flow equations are solved iteratively while a staggered grid arrangement as required by the SIMPLE algorithm is used for discretization. Later, the proposed simulation is applied to predict parts produced by the high pressure die cast process (HPDC). The model is validated by comparing its results with those obtained from the commercial flow-and-solidification software Flow3D® as well as with the experimentally measured secondary dendrite arm spacing (SDAS).

4.1. Model development

In typical applications related to a high pressure die-cast process, metal has to flow through a combination of thin (1-3 mm) and thick sections (4-8mm). Commercial software

allows one to use different mesh densities based on the scale of the computational domain. As can be seen in Figure 4.1, the ventilation (or the gas evacuation) channel is an order of magnitude smaller than the rest of the casting. Substantial reduction in the cell size is required in order to achieve a convergent solution in a thin channel portion of the casting. Owing to the fact that flow in the cavity of the die-cast die is highly turbulent, the mesh has to be sufficiently refined in order to resolve the flow accurately.

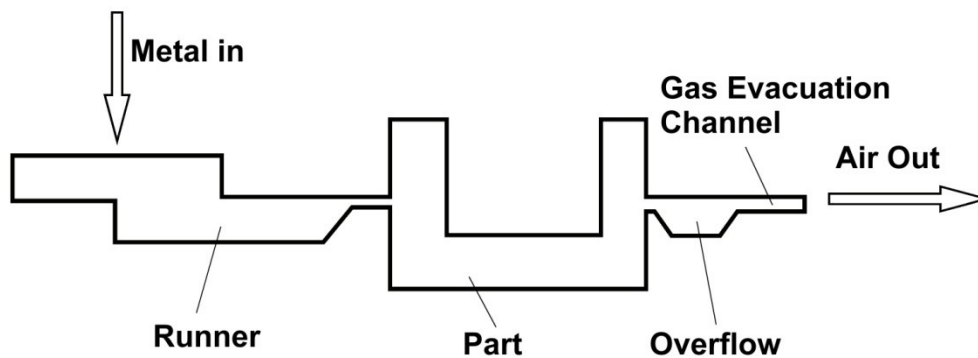


Figure 4.1 A schematic showing the thick and thin section of a typical die-cast part

Further increase in mesh density to accommodate flow within thin ventilation channels is usually impractical, and as a common practice, the flow analyses are conducted in the main cavity only. The algorithm presented in this paper will allow one to extend the flow and solidification analysis into thin channels also. The computational domain is divided into two regions (see Figure 4.2). In the main cavity, the flow and solidification analysis is conducted using commercial software, which solves the three-dimensional Navier-Stokes equation coupled with energy equation. In the thin-channel region, the lubrication equation, coupled with heat balance equation developed for a control volume defined around a node of the 2-D in-plane mesh, is solved in a finite time interval iteratively. Owing to the fact that both models are solved in different dimensional

and time scales, a procedure was developed to transfer the flow-variable values from the main cavity to the thin-channel via the interface (or ‘cut-off’) plane.

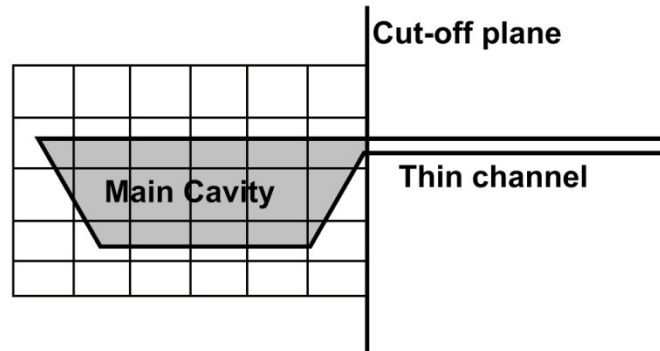


Figure 4.2. A schematic showing the main cavity and the thin channel of a die-cast die connected through a cut-off plane.

4.2 Main cavity model

Flow variables and temperature distribution in the main cavity are solved using the general-purpose commercial CFD software FLOW3D[®]. The software provides solutions to three-dimensional fluid and heat flow and solidification problems using the finite difference approximation. The Navier –Stokes equations coupled with the energy equation achieve an accurate representation of the turbulent fluid and heat flow accompanied with solidification. The two-equation k - ϵ model is used to resolve the properties of turbulent flow. A control volume method is used to discretize the governing equations and the enthalpy method is used to evaluate temperature distribution in the die cavity. The VOF (volume of fluid) method is used to accurately track free surface evolution in the computational domain.

4.3 Thin channel model

Owing to the small aspect ratio (height to length ratio) of the channel,

$$\varepsilon = \frac{H_o}{L_c} \ll 1 \quad (4.1)$$

and the problem of modelling metal flow in the ventilation channel can be reduced to the solution of the in-plane lubrication equation combined with the solution of the out-of-plane heat transfer and solidification model (see chapter 3 as well as [34]). To take into consideration the high-velocity flow observed in the die-cast process, the inertia-effect terms were added to the final lubrication equations according to the recommendations of [30, 34]. In order to model die-cast die filling with liquid metal, an extra transient term has to be incorporated into the momentum equation, Eq. (3.5), for the steady-flow case discussed in section 3. The governing equations in differential form are shown below.

Continuity equation:

$$\nabla \cdot \vec{v} = 0 \quad (4.2)$$

Momentum balance equations:

$$\rho \left(\frac{\partial v}{\partial t} + \vec{v} \cdot \nabla \vec{v} \right) = \mu \nabla^2 \vec{v} - \nabla p \quad (4.3)$$

Energy balance equation:

$$\rho C \frac{\partial T}{\partial t} + \rho C \vec{v} \cdot \nabla T - \nabla \cdot \vec{q} = 0 \quad (4.4)$$

An order-of-magnitude analysis was conducted in order to simplify the governing equations and to determine the importance of each term during high-speed flows in thin

channels. Only a summary will be presented here—the details of this reduction in the governing equations for thin-channel flows can be found in chapter 3.3 and Appendix A.

For this reduction (chapter 3.3 and Appendix A), the following dimensionless variables were used:

$$\begin{aligned}\tilde{x} &= \frac{x}{L}, \tilde{y} = \frac{y}{L}, \tilde{z} = \frac{z}{H_0}, \tilde{h} = \frac{h}{h_0}, \tilde{t} = \frac{t}{\tau} \\ \tilde{u} &= \frac{u}{\bar{V}}, \tilde{v} = \frac{v}{\bar{V}}, \tilde{w} = \frac{Lw}{\bar{W}h_0}, \tilde{p} = \left(\frac{H_0}{L}\right)^2 \frac{L}{\mu\bar{V}} p\end{aligned}\tag{4.5}$$

The earlier-given governing equation can be re-expressed in dimensionless form, after dropping the inconvenient tilde signs, as:

Continuity equation

$$\frac{\partial u}{\partial x} + \frac{\partial v}{\partial y} + \frac{\partial w}{\partial z} = 0\tag{4.6}$$

Momentum equation

$$\rho \frac{h_0^2 \bar{V}}{L_c \mu} \left(\frac{\partial u}{\partial t} + u \frac{\partial u}{\partial x} + v \frac{\partial u}{\partial y} + w \frac{\partial u}{\partial z} \right) = \frac{\partial^2 u}{\partial z^2} - \frac{\partial p}{\partial x}\tag{4.7a}$$

$$\rho \frac{h_0^2 \bar{V}}{L_c \mu} \left(\frac{\partial v}{\partial t} + u \frac{\partial v}{\partial x} + v \frac{\partial v}{\partial y} + w \frac{\partial v}{\partial z} \right) = \frac{\partial^2 v}{\partial z^2} - \frac{\partial p}{\partial y}\tag{4.7b}$$

The momentum equation in the direction transverse to flow reduces to

$$0 = \frac{\partial p}{\partial z}\tag{4.7c}$$

implying that fluid pressure is uniform in the z direction regardless of the inertia effects in the flow.

The dimensionless groups used in this development are:

Reynolds number

$$\text{Re} = \frac{\bar{V}L_c\rho l}{\mu} \quad (4.8)$$

Modified Reynolds number [39]

$$\delta = \varepsilon^2 \text{Re} \quad (4.9)$$

with $\varepsilon = \frac{h_0}{L_c}$

Eqs. (4.7a) and (4.7b) can now be expressed as

$$\delta \left(\frac{\partial u}{\partial t} + u \frac{\partial u}{\partial x} + v \frac{\partial u}{\partial y} + w \frac{\partial u}{\partial z} \right) = \frac{\partial^2 u}{\partial z^2} - \frac{\partial p}{\partial x} \quad (4.10a)$$

$$\delta \left(\frac{\partial v}{\partial t} + u \frac{\partial v}{\partial x} + v \frac{\partial v}{\partial y} + w \frac{\partial v}{\partial z} \right) = \frac{\partial^2 v}{\partial z^2} - \frac{\partial p}{\partial y} \quad (4.10b)$$

Once again, based on the recommendations of [33], we assume a parabolic velocity distribution along the x and y directions:

$$u = U(x, y)(z^2 - zh) \quad (4.11a)$$

$$v = V(x, y)(z^2 - zh) \quad (4.11b)$$

After integrating over the thickness of the channel, the continuity equation, Eq. (4.6), becomes

$$\frac{\partial U}{\partial x} + \frac{\partial V}{\partial y} = 0 \quad (4.12)$$

Note that based on the no-penetration boundary condition $\frac{\partial w}{\partial z} = 0$ and small size of the cavity in the z direction, w velocity variation is negligible, and is set to zero.

After integrating across the thickness of the cavity from 0 to h, the momentum, Eq. (4.10), becomes

$$\frac{\delta}{2} h \left(-\frac{1}{3} \frac{\partial U}{\partial t} h - \frac{\partial h}{\partial t} U \right) + \frac{\delta}{30} h^4 \left(U \frac{\partial U}{\partial x} + V \frac{\partial U}{\partial y} \right) + \frac{\delta}{6} \left(U^2 \frac{\partial h}{\partial x} + UV \frac{\partial h}{\partial y} \right) h^3 = 2U - \frac{\partial p}{\partial x} \quad (4.13a)$$

$$\frac{\delta}{2} h \left(-\frac{1}{3} \frac{\partial V}{\partial t} h - \frac{\partial h}{\partial t} V \right) + \frac{\delta}{30} h^4 \left(U \frac{\partial V}{\partial x} + V \frac{\partial V}{\partial y} \right) + \frac{\delta}{6} \left(UV \frac{\partial h}{\partial x} + V^2 \frac{\partial h}{\partial y} \right) h^3 = 2V - \frac{\partial p}{\partial y} \quad (4.13b)$$

Note that the only difference between Eqs. (3.23) and Eqs.(4.13) is the presence of the first (transient) terms.

Energy equation

The general thermal energy balance equation (Eqs. (4.4), (3.24), and (3.25)) are described in Section 3.3 and are used in the transient model as well.

Boundary and initial conditions

The thin-channel geometry used for model validation is shown in Figure 4.3. At the initial time $t = 0$, the same uniform temperature, $T = 600^\circ\text{C}$, is applied to the liquid metal lying within the computational domain. At the entrance ($x = 0$), the fluid temperature is set as $T = 600^\circ\text{C}$. At the solid-liquid interface, $T_s = T_l = T_{melt}$. The wall temperatures at $z = 0$ and $z = h$ are set to 60°C . The flow is driven by a uniform velocity imposed at $x = 0$

location. The outflow boundary condition specified at the end of the cavity, $x=L$, (after the liquid has gone beyond the exit) is $\frac{\partial u}{\partial x} = 0$. The no-slip boundary conditions are applied at the left and right walls in the y direction. Additionally, a symmetry boundary condition, in the form of the velocity gradient in the direction normal to the wall being equal to zero (i.e., $\frac{\partial v}{\partial y} = 0$), is applied.

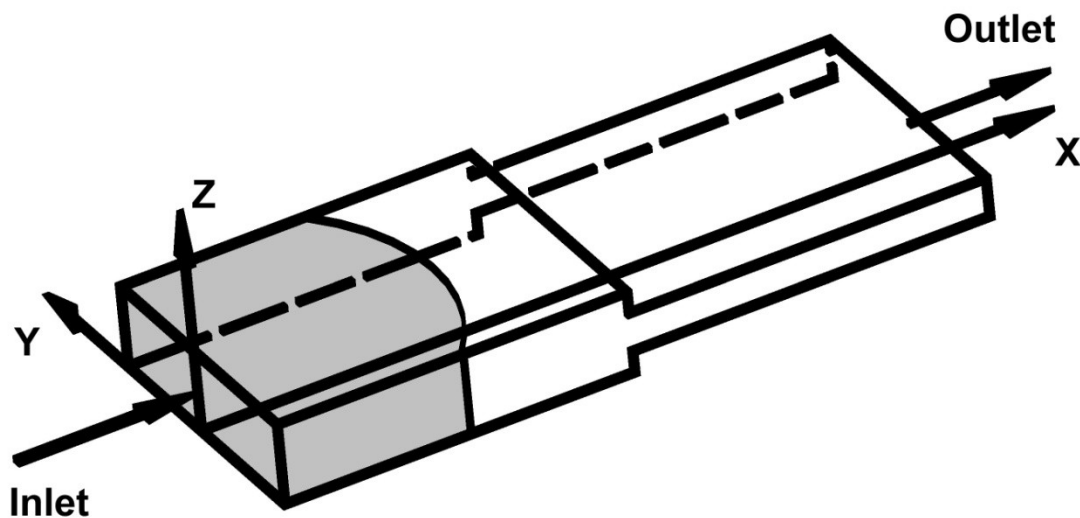


Figure 4.3 The thin-channel geometry used for model validation: the left- and right-side segments are 1 mm and 0.5 mm thick, respectively. (The other dimensions are given in Figure 4.11 and Table 4.1)

Note that Eqs. (4.12), (4.13) and (3.25) form the governing equations for the thin channel problem.

4.4 Coupling of the main cavity and thin channel flows

Main cavity and thin channel are divided by cut-off plane (see Figure 4.2). In order to ensure a smooth transition of velocities and pressure from the main cavity into the thin channel region, the pressure, velocity and temperature values have to match at

the cut-off plane. The metal velocity in the main cavity is matched to the metal velocity in a thin channel by the fact that flow volume supplied from the main cavity is equal to the volumetric flow in the channel:

$$\bar{v} = \bar{U} \frac{H}{h} \quad (4.14)$$

The temperature and pressure distributions at the exit of the main cavity are integrated over the thickness of the cavity H , such that these averaged values are applied as a temperature and pressure boundary conditions for the thin channel section at the cut-off plane. The time-step size has to be addressed as well. Owing to the difference in the length scales of the two regions, the time scales of the main cavity and thin channel regions are related as

$$\Delta t_{channel} = \frac{\Delta t_{main}}{\lambda} \quad (4.15)$$

The parameter λ had to be chosen such that the solution in the thin channel was kept stable. Based on the difference in the main cavity and thin channel length-scales, the scale parameter was chosen to be $\lambda = 10$.

4.5. Discretization of governing equations

The computational domain has to be subdivided on smaller controlled volumes where the average flow variables can be solved for using the discretized form of balance laws.

4.5.1 Main cavity

Owing to the fact that FLOW3D[®] [39], a commercial CFD software, was used for computing flow and temperature quantities in the main cavity, discretization of governing

equation for the main cavity is not given in this paper. Automatic structured grid generation function of the software was used to discretize the computational domain. The fractional area/volume method, FAVOR™ [11], is used for modelling the complex geometry of our main cavity.

4.5.2 Thin channel

To avoid unrealistic behaviour of the momentum equations, a staggered grid arrangement is used to discretize the governing equations, Eqn. 4.13 (a) and (b), in the thin channel using the SIMPLE algorithm. The principal of the 2-D staggered grid arrangement (Figure 4.4) is that the scalar quantities such as pressure, temperature, and height of the channel are stored at the centre of the control volume. However, storage of velocity components are staggered with respect to the faces: velocities ‘ U ’ are stored at the west and east faces, while velocities ‘ V ’ are stored at the north and south faces. The discretization of the governing equations in thin cavity is described in detail in Appendix B; only equations in the final form are given below in section 4.6.2.

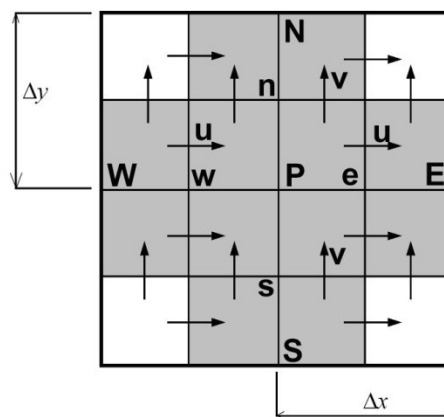


Figure 4.4. The staggered grid arrangement (based on SIMPLE algorithm) was employed for solving the in-plane flow variables.

4.6. Solution procedure

Solution procedure in the form of a flow chart is described in Figure 4.5. Initial conditions in the main cavity include metal temperature, cold chamber die-cast machine plunger-velocity profile, initial temperature of the die-cast die.

4.6.1 Solution procedure in main cavity

Before calculations of the metal flow in the main cavity can begin, die temperature distribution has to be established. Using a FLOW3D feature called "thermal die cycling", the die is filled with molten metal instantaneously and held for the duration of the dwell time (25s). During this time, the conduction equation to predict temperature in the die-cast die is solved in order to account for heat transfer from liquid metal to the die steel. Then the liquid metal is 'removed' from the die 'instantaneously', and external cooling is applied to the die in order to correct the die steel temperature. This process is repeated until the die temperature attains a quasi-stable state. The final calculated die temperature was compared to the temperature of the die-cast die using a thermal imaging camera. Process was repeated with adjustment in time and efficiency of the external cooling, until error of temperature distribution was less than five percent. When the thermal quasi-stable state is achieved, flow analysis in the main cavity can begin. The final die temperature is used as a boundary condition for further flow and solidification analysis in the main cavity. Metal in the cavity is then driven by the plunger of the die cast machine. (Figure 4.6 shows the schematics of a typical die-cast die with shot cylinder and piston assembly.)

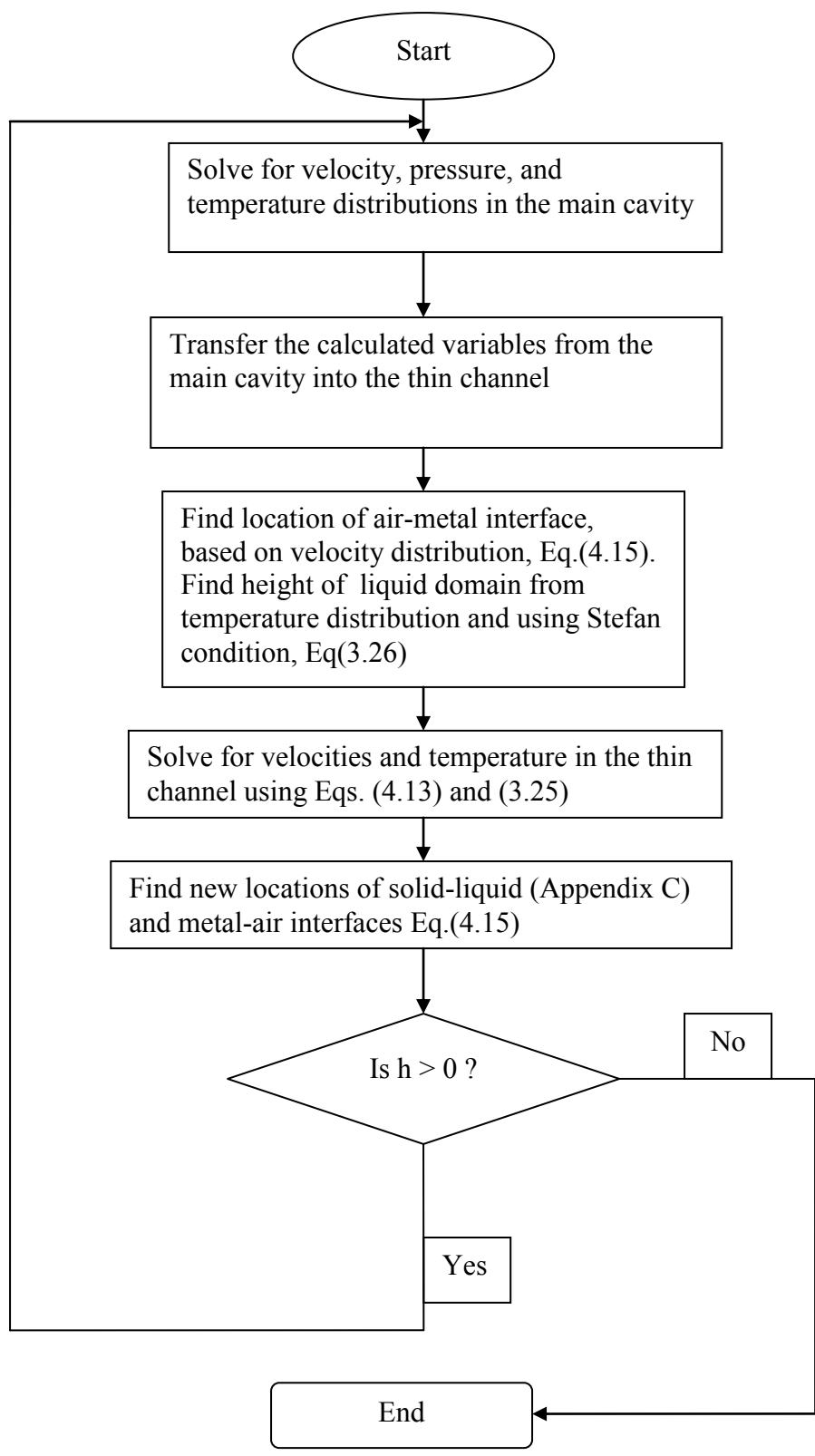


Figure 4.5 The proposed solution algorithm for solving flow and temperature variables in the thin cavity

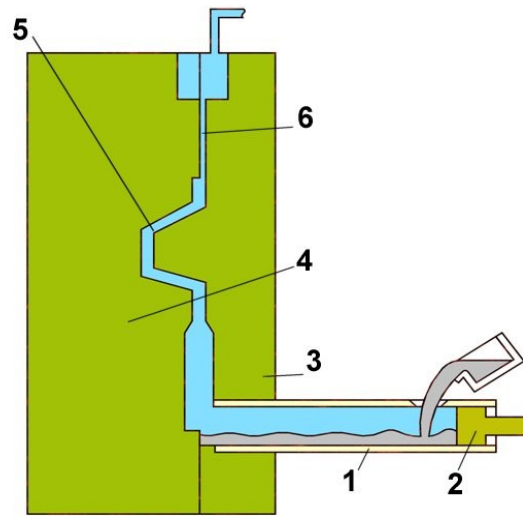


Figure 4.6 A schematic of a die-cast die with shot sleeve and plunger: 1) Shot sleeve, 2) Plunger, 3) Stationary half of the die-cast die, 4) Ejector half of the die-cast die, 5) Mold cavity, 6) Ventilation channel.

The plunger velocity profile (Figure 4.7) is transferred into FLOW3D[®] from the shot monitoring system VisiTrak[®]⁵. Calculations in the main cavity continue until the liquid metal has reached the cut-off plane, which is positioned on the border between the main cavity and thin channel. At this point, all flow and temperature variable values are transferred from the main cavity into the thin channel using the procedure outlined in Section 4.4

Tracking of free surface between liquid metal and air

Fractional volume of fluid (VOF) [11] method is used to track the metal-air free surface interface. Method is based on the assumption that function F , which represents fraction of fluid in the cell, can assume values between 0 and 1: value 1 is assigned to the cell full of

⁵ The shot monitoring system is for tracking the plunger velocity during the injection process.

fluid, while 0 is assigned to an empty cell (see Figure 2.2). Based on this assignment, every cell with function F values between 0 and 1 contain a free surface. The time-dependent function F is governed by the equation

$$\frac{\partial F}{\partial t} + u \frac{\partial F}{\partial x} + v \frac{\partial F}{\partial y} = 0 \quad (4.16)$$

which states that the value of F moving with the fluid remains unchanged. The VOF method is based on the assumption that the local rate of change of F in a cell is equal to the amount of F fluxing through the faces of the cell. The total amount of fluid volume crossing the face of the cell per unit cross-sectional area is $Vol = U\delta$; this is multiplied by the cell face-area to estimate the amount of fluid passing through in a unit of time.

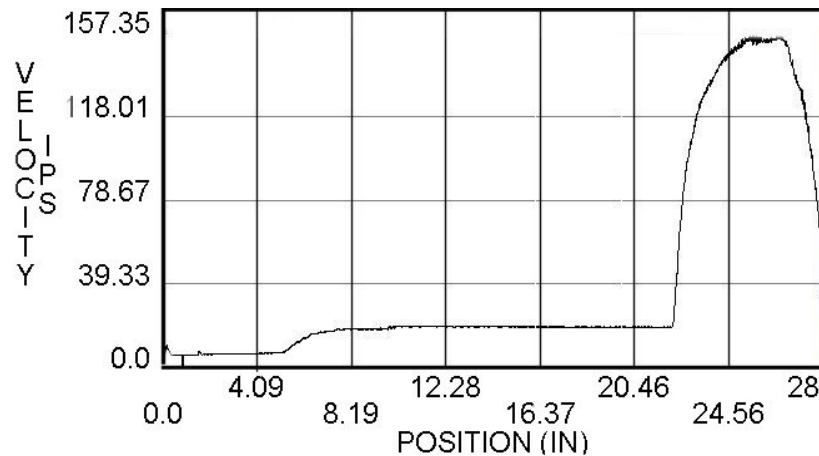


Figure 4.7. Typical plunger velocity profile (IPS = inches per second)—‘position’ is the distance plunger travels during the die cast process.

4.6.2 Solution procedure in thin channel

The problem is solved in a straight channel with a rectangular cross-section (Figure 4.3). Computation begins with an estimation of temperature distribution in the computational domain. It establishes the location and shape of the solid-liquid interface in the region

traversed by the liquid metal. The solid-liquid interface defines the boundary of the liquid domain. Then the momentum equations can be solved to define the distribution of thickness-averaged velocities in the computational domain. This velocity distribution is then used to define the position of the free surface in the next time step. The assumptions adapted for the development of the proposed algorithm are: 1. Fluid is incompressible and Newtonian. 2. Flow is laminar. 3. Heat conduction in the direction of metal flow in the channel is negligible. 4. Heat resistance of the channel walls are negligible

Solution of the thickness-averaged continuity and momentum equations

Discretized forms of Eqns. (4.12), (4.13), and (3.25) can be expressed as follows.

In the following equations, Eqs. (4.17)—(4.19), indices in capital letters indicate the primary grid where indices in small letters indicate the secondary grid (see Appendix B for more details).

Continuity equation:

$$\left[(U)_{i+1,J} - (U)_{i,J} \right] + \left[(V)_{I,j+1} - (V)_{I,j} \right] = 0 \quad (4.17)$$

Momentum equation *In the x direction:*

$$\begin{aligned} & -\frac{1}{6} \frac{U_{I,J}^{n+1} - U_{I,J}^n}{\Delta t} + \frac{\delta}{30} h_{i+1,J}^4 \left[\frac{(U^2)_{I+1,J}^n - (U^2)_{I,J}^n}{\Delta x} + \frac{(UV)_{i+1,j+1}^n - (UV)_{i+1,j}^n}{\Delta y} \right] \\ & + \frac{\delta}{6} h_{i+1,J}^3 \left[U_{I,J}^2 \frac{(h)_{i+1,J}^n - (h)_{I,J}^n}{\Delta x} + UV_{I,J} \frac{(h)_{i+1,j+1}^n - (h)_{i+1,j}^n}{\Delta y} \right] \\ & = 2 * U_{I,J}^n - \frac{(P)_{I+1,J}^n - (P)_{I,J}^n}{\Delta x} \end{aligned} \quad (4.18a)$$

In the y direction:

$$\begin{aligned}
& -\frac{1}{6} \frac{V_{I,J}^{n+1} - V_{I,J}^n}{\Delta t} + \frac{\delta}{30} h^4_{I,j+1} \left[\frac{(V^2)_{I,J+1}^n - (V^2)_{I,J}^n}{\Delta x} + \frac{(UV)_{i+1,j+1}^n - (UV)_{i,j+1}^n}{\Delta y} \right] \\
& + \frac{\delta}{6} h^3_{I,j+1} \left[V_{I,J}^2 \frac{(h)_{I,J+1}^n - (h)_{I,J}^n}{\Delta x} + UV_{I,J} \frac{(h)_{i+1,j+1}^n - (h)_{i,j+1}^n}{\Delta y} \right] \\
& = 2 * V_{I,J} - \frac{(P)_{I,J+1}^n - (P)_{I,J}^n}{\Delta y}
\end{aligned} \tag{4.18b}$$

Energy equation

Heat balance equation, Eq. (3.25), discretized over the control volume in a finite time-interval results in

$$\begin{aligned}
& \rho C_p U_{i+1,J} (\Delta x \Delta y) T_{i+1,J} - \rho C_p U_{i,j} (\Delta x \Delta y) T_{i,j} + \rho C_p V_{I,j+1} (\Delta x \Delta y) T_{I,j+1} \\
& - \rho C_p V_{I,j} (\Delta x \Delta y) T_{I,j} = \rho C_p (\Delta x)(\Delta y) \frac{\partial (h_{I,J} T_{I,J})}{\partial t} + 2q_w (\Delta x)(\Delta y)
\end{aligned} \tag{4.19}$$

The momentum equations are solved using the SIMPLE procedure [7] which is used to couple the momentum and continuity equations. The momentum equations, Eqs. (4.18a) and (4.18b), use the pressure field transferred from the main cavity and solve for preliminary velocities U and V . In its incompressible form, the mass conservation equation doesn't have a pressure term. However, an artificial compressibility term, “ a ”, has to be added to the modified continuity equation, Eq.(3.27), to allow for the solution of pressure P . Usual values of the artificial compressibility term are $0.1 > a > 1.2$; it is taken to be 1.2 [39] in the presented algorithm.

The modified continuity equation, derived from Eq. (3.27), is used to calculate the corrected values of the pressure field:

$$\frac{P_{i,j}^{n+1} - P_{i,j}^n}{\Delta t} + a^2 \left(\frac{U_{i+1,j}^{n+1} - U_{i,j}^{n+1}}{\Delta x} + \frac{V_{i,j+1}^{n+1} - V_{i,j}^{n+1}}{\Delta y} \right) = 0 \quad (4.20)$$

Solution of the continuity and momentum equations procedure can be broken down into following steps: 1. Use the pressure transferred from the main cavity in the first time-step. 2. Solve the momentum equation to estimate the preliminary values of U and V . 3. Use the modified continuity equation, Eq. (4.20), to correct pressure values. 4. Correct the U and V velocities using the new pressure values and continue the iterations until the continuity equation, Eq.(4.17), is satisfied.

At this point of the analysis, the height of the thin channel, h , in the momentum equations still remains unknown. In the absence of solidification, the momentum and continuity equations alone will allow one to estimate the velocity and pressure distributions in the thin channel behind the front in a given time step. In order to close the system energy balance, Eq. (4.19) has to be solved; solution of this energy balance equation allows one to estimate the temperature distribution in our calculation domain. Based on the result of the energy equation and through the use of the Stefan condition, Eq. (3.26), the location of the solid-liquid interface can be established for every time-step (see Appendix C for details). The location of the solid-liquid interfaces allows one to update the h values and to use them in the momentum equation for the next time-step. It is assumed, in this algorithm, that there is perfect contact between the solidified metal and walls of the channel. Wall temperature of the channel remains constant during the calculation procedure—this means that the walls have high thermal mass and conductivity.

4.7 Summary of Numerical Methods

The presented numerical algorithm allows one to estimate the flow and solidification variables during the die-cast operation in a mould containing a thick main cavity and a thin ventilation channel. Flow and heat transfer in the main cavity is estimated using the commercial software Flow-3D. The cut-off plane separating the main cavity from the thin channel is used to transfer flow and temperature variables from the main cavity to the thin channel as boundary and initial conditions in the proposed algorithm. The flow velocities and time steps are transferred according to the length-scale difference between the two flow regions. Velocities and pressure distribution in a thin channel are estimated using the lubrication approximation after taking into account inertia effects and solidification in the metal. The 3-D flow field is reduced to a thickness-averaged 2-D flow field which is to be solved in the central plane of the thin channel. The liquid metal-air free surface is tracked using the VOF method. The channel gap is estimated after incorporating solidification through 1-D out-of-plane heat transfer in the channel. Owing to the simplification of the algorithm based on the lubrication approximation, the proposed numerical approximation is expected to offer significant amount of savings in computational time.

4.8. Validation of the Proposed Numerical Algorithm

Casting shown in Figure 4.8 is produced by a cold chamber high pressure die-cast process.

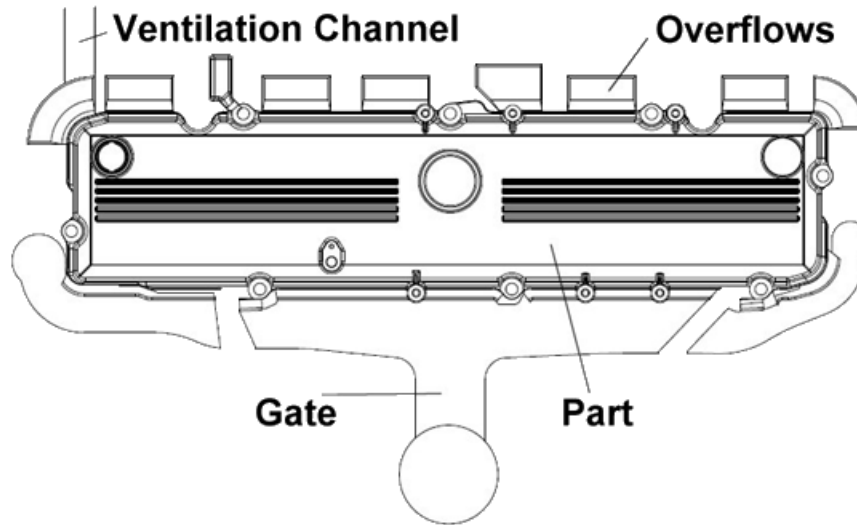


Figure 4.8 A picture (a ‘full shot’) of a part made using the die-cast process. The overflows are created when the metal front, after filling the main cavity, fills up the machined ‘overflow’ pockets in the die-cast mold. Ventilation channel is last to fill-up.

The plunger velocity profile is transferred into FLOW3D[®] from the shot monitoring system VisiTrak[®] and is shown in Figure 4.7. The molten-metal (Aluminium A380) temperature was set at 650⁰C, and the initial die-temperature was set at 150⁰C. Through the instantaneous fill-cycle process of FLOW3D⁶, the die temperature was made to reach a quasi-stable state. Then a prescribed plunger velocity was applied to fill the cavity of the die-cast die. Results of the flow analysis are shown in Figure 4.9. Final temperature distribution in the cavity of the die- cast die filled with liquid metal is illustrated in Figure 4.10.

⁶ Twenty five instantaneous fill cycles were applied.

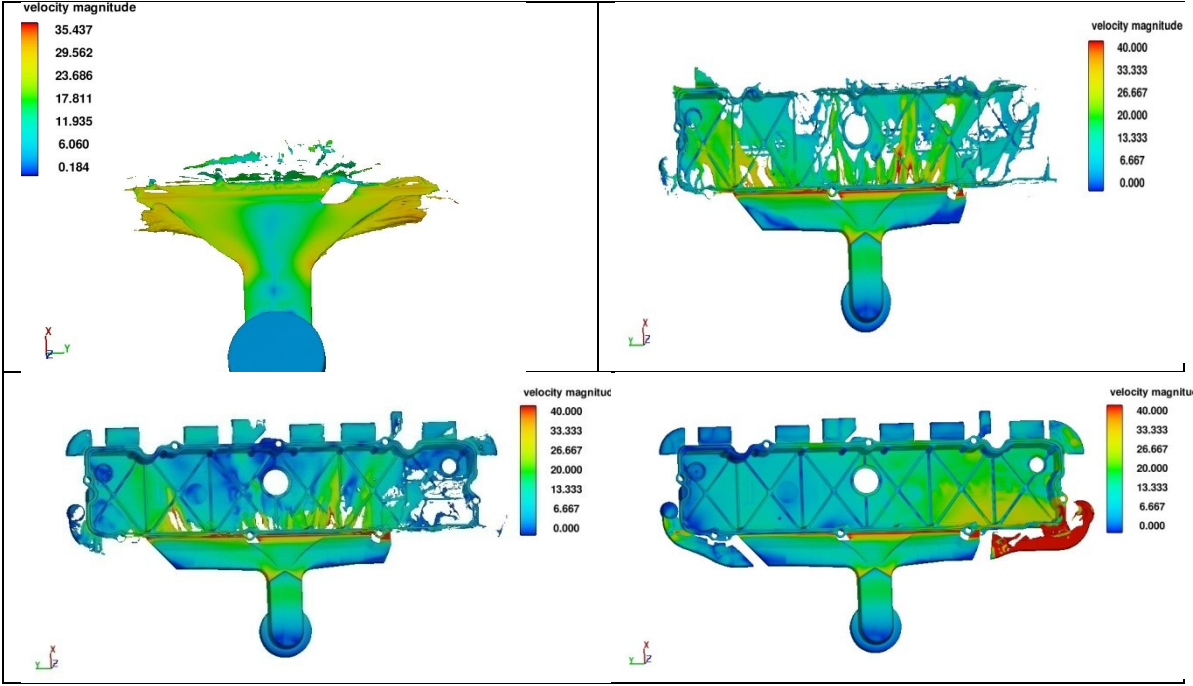


Figure 4.9 Flow analysis results using FLOW3D of the metal flow and solidification in the main cavity. (The velocity is in m/s.)

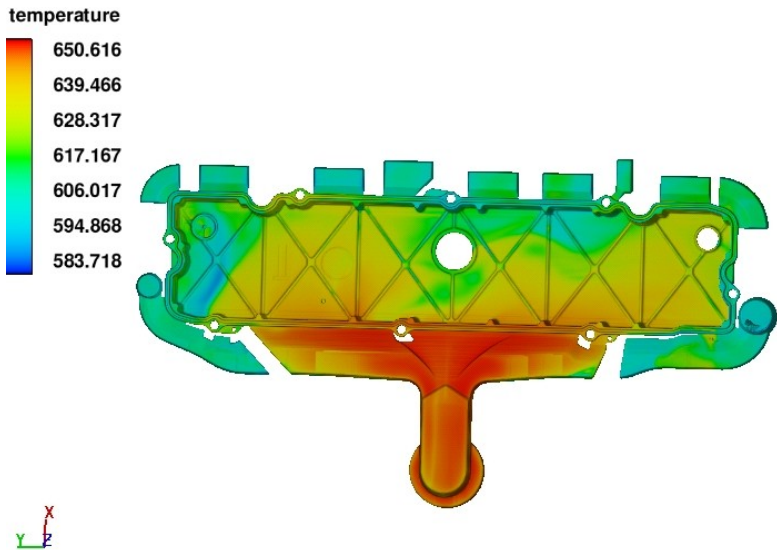


Figure 4.10 Temperature distribution in the considered cavity of the die-cast die, filled with liquid metal at the end of the fill process. (The temperature is in °C.)

Velocity, temperature, and pressure distribution were extracted from the main cavity at the location of the cut-off plane. All the flow and metal temperature quantities

were transferred into the proposed algorithm as the initial condition for the subsequent numerical simulation in the thin channel. In order to verify the velocity distribution predicted by the proposed algorithm, they were compared with the ones obtained from the analysis conducted by the commercial software FLOW3D. A separate three-dimensional model of the thin channel was imported into FLOW3D. The velocity and temperature distributions, converted into thin-channel scale, were applied as a boundary and initial conditions. The temperature and velocity at the inlet of the channel were considered constant. Both FLOW3D[®] and our proposed numerical algorithm were set to run until the solid-liquid interfaces converged at the middle of the channel.

In order to establish the validity of governing equations [Eqs. (4.12), (4.13) and (3.25)] for modelling the flow and solidification of liquid metal in a thin channel, the resultant simulation was applied to a ventilation channel of rectangular cross-section (Figure 4.11).

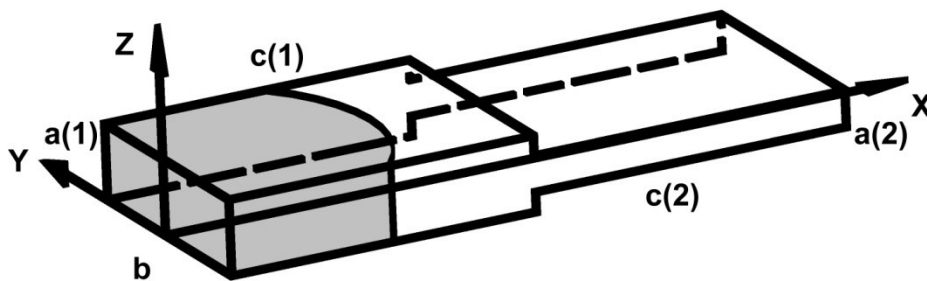


Figure 4.11 A schematic of the considered ventilation channel: the stepped profile is necessary to solidify and contain the overflowing metal. The dimensions a , b and c are listed in Table 4.1.

Table 4.1 Thin channel dimensions

	a(1)	a(2)	b	c(1)	c(2)
Dimensions (mm)	1	0.5	20	50	50

The proposed governing equations were solved numerically and the results were compared with the solution of the incompressible Navier – Stokes equations fully-coupled with the three-dimensional energy equation during solidification that was solved using the commercial software FLOW3D. Finally, a parametric study was conducted to define the relation between metal progress in the ventilation channel and three parameters: initial velocity, temperature of the channel walls, and the thickness of the channel. Developed curve can be used as a guide in designing ventilation channel of the die-cast dies.

Properties of the commercial Aluminium alloy, A380, were used for our numerical calculations. Results of the numerical prediction of the flow and solidification of the molten metal flowing in a thin channel by our code were compared with the results obtained from the commercial software FLOW3D as well as the actual casting lengths. The predicted rate of solidification was further validated by comparing the calculated (based on the results obtained using the proposed numerical algorithm) and measured secondary-dendrite-arm spacing.

4.9 Validating velocity distribution in the channel

Metal flow in the cavity, as controlled by the solid-liquid interface location in the channel, was studied. Mesh density was set at 500 X 150 cells along the x and y directions, respectively. Ventilation channel in FLOW3D was meshed with 100X10X5

computational cells in x, y, and z direction, respectively. Decision on mesh densities in both algorithms were based on our mesh independence analysis, and were carried out until differences in the obtained results did not vary more than 0.1%.

Velocity distributions in a channel was extracted at fixed locations (see Figure 4.12) at a given time from the numerical results given by the proposed algorithm and the results obtained from the commercial software FLOW3D; such comparisons are shown in Figure 4.13.

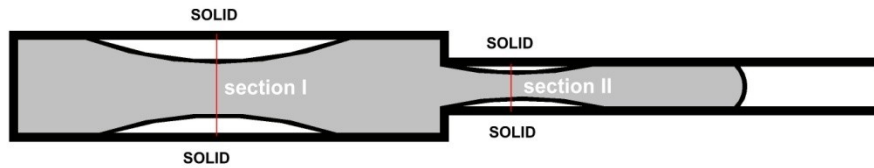


Figure 4.12 A schematic showing a typical cross-section of the stepped ventilation channel. Sections I and II are used for the comparison of predictions by the proposed algorithm and FLOW3D.

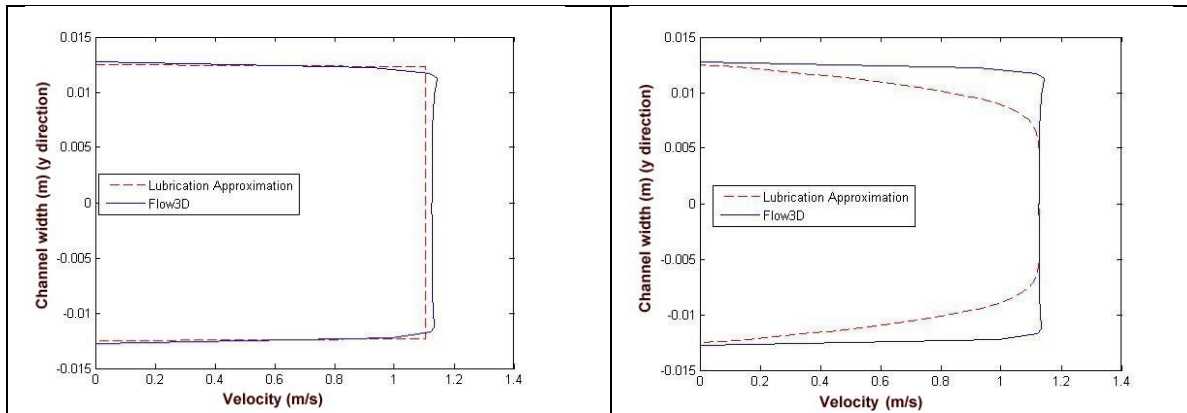


Figure 4.13 Comparison of velocity distributions in the ventilation channel: (Left at 0.05s) section I and (Right at 0.05s) section II of Figure 4.12. Note that the plot gives velocities averaged along the thickness direction.

Solution obtained from FLOW3D takes into account the turbulent character of the flow where it employs fully-coupled three-dimensional momentum and energy equations. Turbulent quantities were resolved using the two-equation $k - \varepsilon$ model. As observed in Figure 4.13, the thickness-averaged velocity distribution, obtained from the lubrication approximation based simulation, do not differ by more than 5% from the full 3D flow and solidification simulation. However, due to the turbulence character of the flow, the resultant velocity distribution obtained using FLOW3D exhibit plug-type flow profile. Assumptions of laminar flow and parabolic velocity profile in the proposed algorithm explain the differences in velocity profiles obtained from FLOW3D and the algorithm. The in-plane velocity profile approximated by the lubrication formulation becomes curved as flow progresses along the channel. On the other hand, the velocity profile predicted by FLOW3D appears plug-like, which is typical of turbulent flows.

4.10 Validating solidification analysis

Solidification analysis is an important part of the numerical approximation of the die-cast process. It defines the boundary of computational domain during liquid-metal flow simulation, as well as mechanical properties of the die-cast part [35]. Initial metal temperature was extracted from the flow and solidification analysis conducted in the main cavity. Temperature of the metal was kept constant at the inlet during numerical simulation of flow and solidification in the ventilation channel. Temperature of the channel walls used in the simulation is based on the measured temperature of the die steel of the die-cast die. Twenty consecutive measurements using an infrared device ('thermal gun') has shown that average temperature of the channel walls is 60° C. Due to the quick

filling of the channel, wall temperature was considered constant. In order to verify the accuracy of temperature distribution obtained using the proposed algorithm, values of metal temperature were extracted at two specified locations (Sections 1 and 2) shown in Figure 4.12. Along-the-thickness temperatures presented in Figure 4.14 show a very good correlation between results from the proposed algorithm and results from the commercial software FLOW3D.

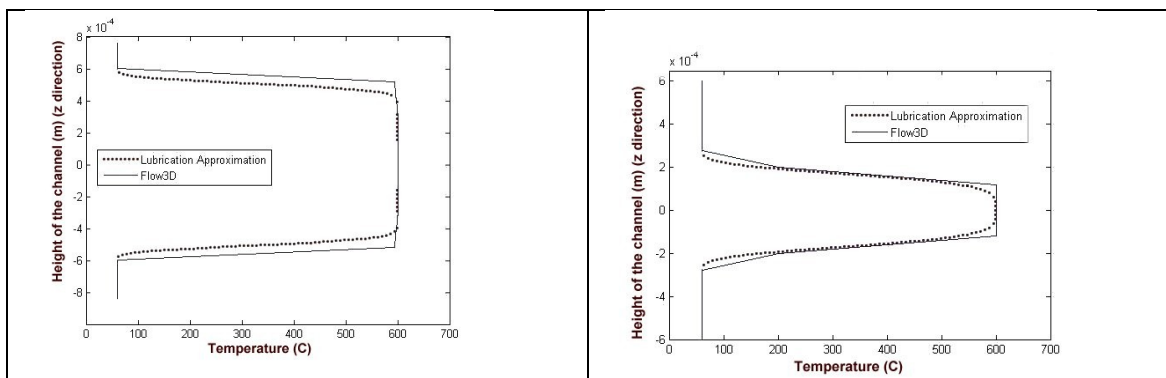


Figure 4.14 Comparison of temperature distributions in the ventilation channel: (Left at 0.05s) section I and (Right at 0.05s) section II of Figure 4.12.

4.11 Validating locations of liquid metal-air and solid-liquid interfaces

As was described above, the proposed algorithm allows one to predict the location of the solid-liquid interface as well as the location of the free surface as they evolve during computational cycle. Location of the solid-liquid interface is found using the Stefan condition, while the free-surface position is defined by the VOF method. Velocity and temperature distributions are calculated in the liquid region.

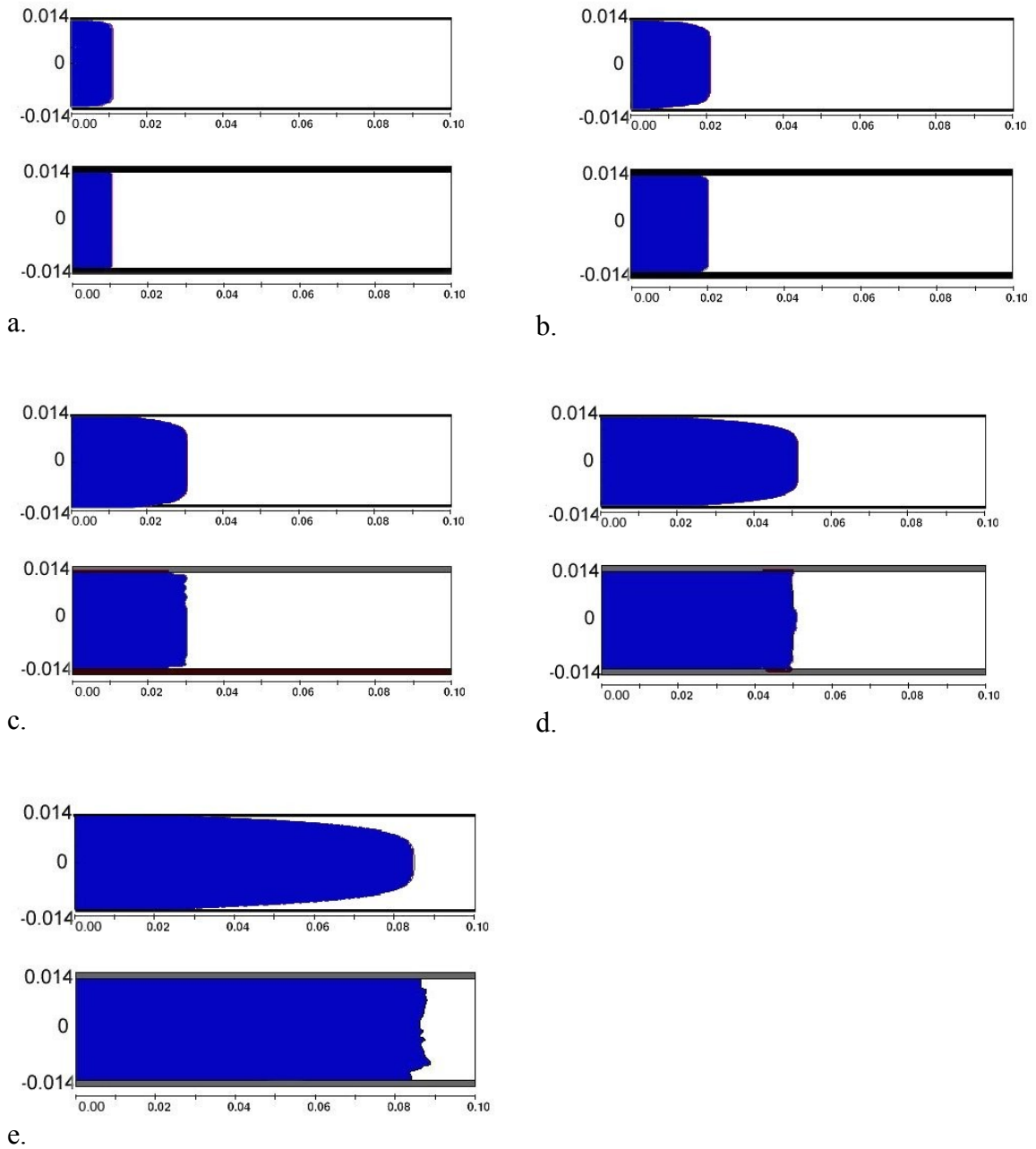
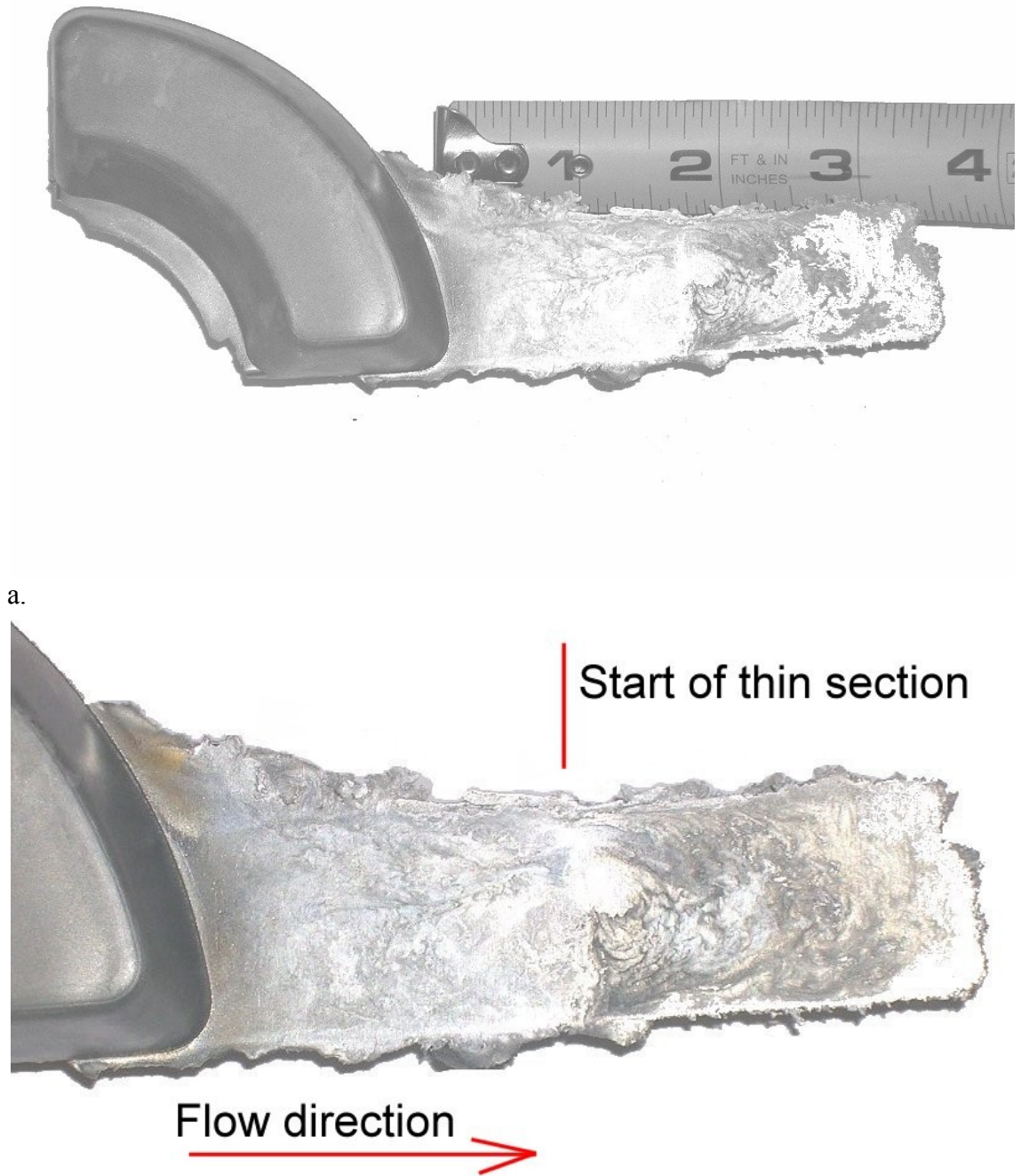


Figure 4.15 Locations of the free surface: Proposed numerical algorithm (top), FLOW3D (bottom) at a) 0.01s, b) 0.018s, c) 0.029s, d) 0.045s, e) 0.06s [In all views, the horizontal axis along 'x' direction is along the channel length, while the vertical axis is the width of the channel (m) in 'y' direction]

Locations of the free surface at various times are shown in Figure 4.15. As it can be seen, there is good correlation in the location of the free surface as predicted by our

algorithm and FLOW3D. However, an observation can be made on shapes of the free surfaces predicted by the two simulations. The proposed algorithm predicts a smooth, second order curve as a free surface, compared with the almost flat free-surface predicted by FLOW3D. Actual casting of the metal solidified in the ventilation channel shows that both algorithms predicted correct length of metal flow in the channel (note that numerically estimated flow-lengths were found to be within 5% of the flow-lengths seen in an actual casting), but FLOW3D predicted correct shape of the solidified metal⁷ (see Figure 4.16). An explanation of the difference in the free-surface shapes comes from the assumption of laminar flow in the proposed algorithm; FLOW3D utilizes the two-equation k- ϵ model for modelling the turbulent metal flow, which contributes to its ability to predict correct free-surface shape.

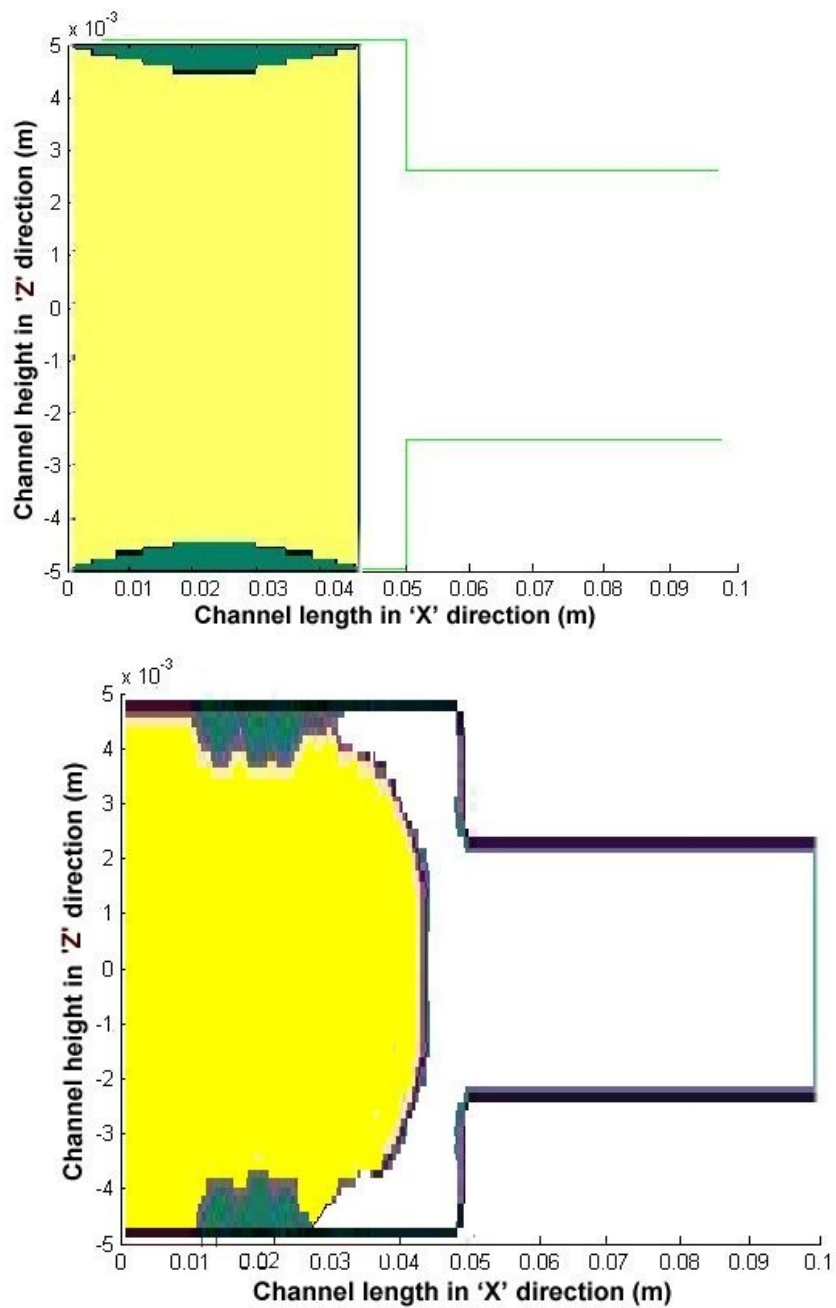
⁷ The sections of castings (Figure 4.16) have confirmed that the wavy shape of the solidified metal as predicted by Flow3D is quite accurate.



b.
Figure 4.16 Experimentally observed solidified metal in the ventilation channel; a) Measured length of metal flow in the ventilation channel after solidification stops it; b) Enlarged image of the solidified metal in the channel

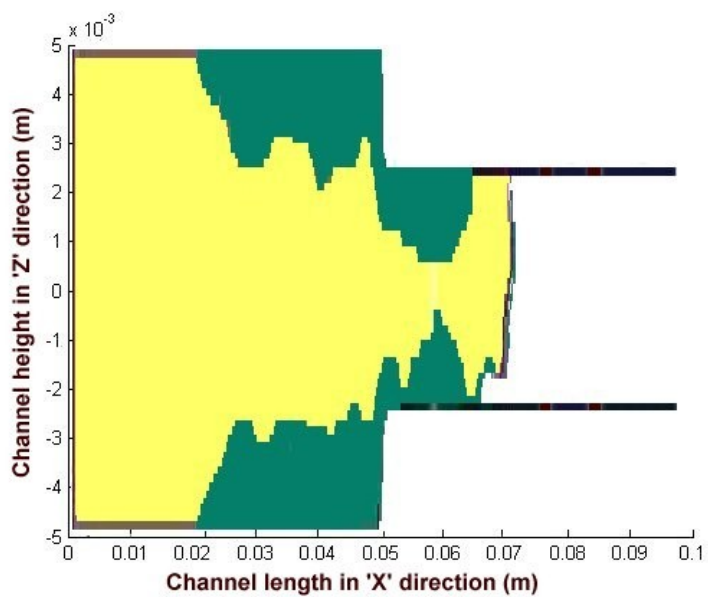
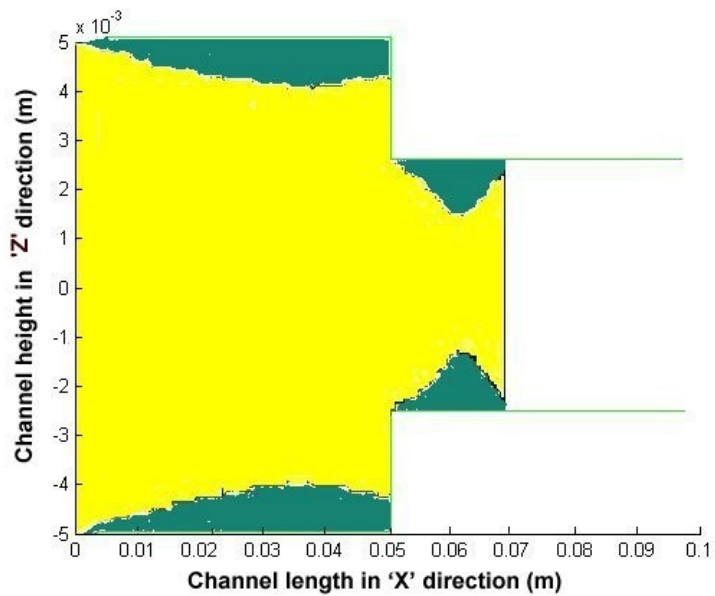
Locations of the solid-liquid interface as predicted by the two simulations, at various times, are shown in Figure 4.17. It can be observed that as the metal flows in the cavity, heat gets extracted by the channel walls held at constant temperature, below the temperature of solidification. Metal solidification on walls occurs at some distance from the channel inlet. As metal continue to flow into the cavity and reaches the thinner section of the channel, the metal starts solidifying at the cross-over point also. It can be explained by the fact that since the velocity in the constricted part of the channel is higher, it increases the heat transfer between walls of the channel and the liquid metal. Both algorithms predict correct locations of the areas where constrictions due to metal solidification on walls are formed inside the channel, and the area where the top and bottom solid-liquid interfaces converge in the middle of the channel and stop the metal flow. This location is also confirmed by the actual casting (Figure 4.16), where the darker area in the beginning of the thinner area of the channel⁸ indicates where the solidification occurs first.

⁸ The dark color of the metal is due to the mixing of burnt die-release agent with liquid metal at the contraction of channel.



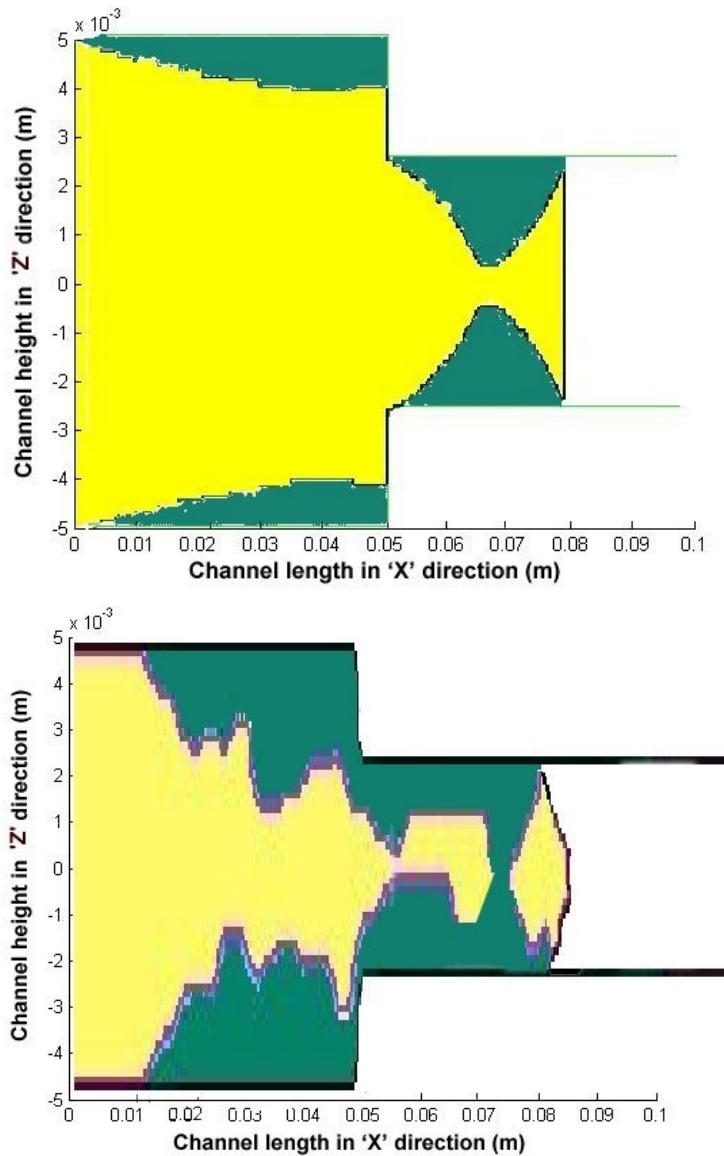
a.

(Figure 4.17)



b.

(Figure 4.17)



c.

Figure 4.17. Location of the solid-liquid interface predicted by simulations: the proposed algorithm (top), commercial software FLOW3D (bottom) at a) 0.036s, b) 0.055s, c) 0.06s. The yellow (light) color represents the liquid metal while the green (dark) color signifies solidified metal.

4.12 Verification of cooling rate using measured secondary dendrite arm spacing.

Often verification of the cooling rate of the molten aluminium is conducted by comparing the calculated and measured Secondary Dendrite Arm Spacing (SDAS) [42]. Three samples were prepared to measure SDAS. Preparation procedure included: a) cutting the

sample, b) mounting the sample in a fixture using an epoxy, c) grinding and polishing with progressively reduced grit size until a planer surface is achieved, d) chemical etching using a reagent. Keller's reagent was used to prepare sample shown in Figure 4.18; the purpose of this step was to highlight the microstructure of the specimen.

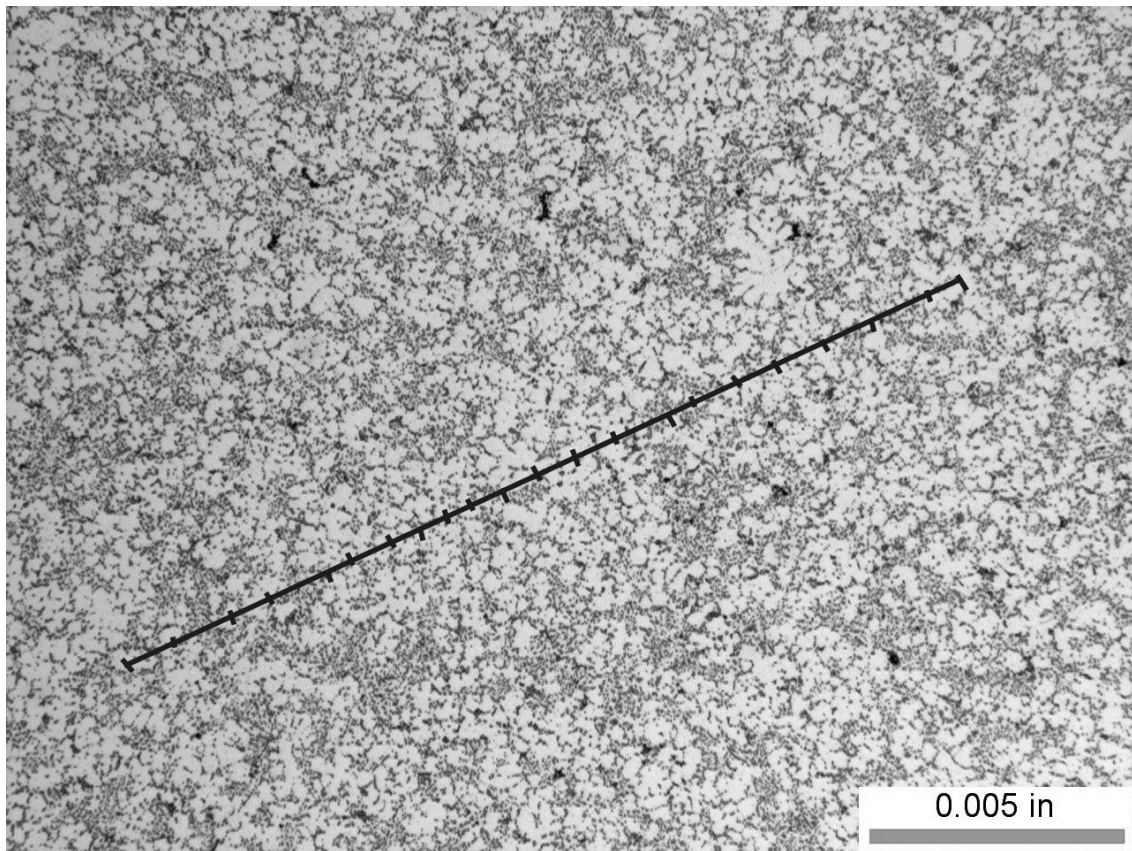


Figure 4.18 Cross section of the casting used to measure SDAS (200X magnification)

Three separate samples were prepared using procedure described above. Measured SDAS were in the range 0.00017 – 0.00019 m. In order to verify rate of solidification of the presented algorithm and commercial software FLOW3D, solidification curve was plotted (see Figure 4.19). Based on the calculated rate of solidification, SDAS can be estimated using the formulae

$$\lambda_2 = 5.5 \left(M \frac{\Delta T}{Gv} \right)^{1/3} \quad (4.21)$$

where, G is a temperature gradient, v solidification rate, and ΔT is a temperature range between the start and end of secondary dendrite growth.

The constant M is estimated as

$$M = \frac{D\Gamma \ln(c_e / c_0)}{m(1 - k_d)(c_e - c_0)} \quad (4.22)$$

where D , Γ , c_e , c_0 , m , and k_d are diffusivity, Gibbs—Thompson coefficient, eutectic concentration, solute concentration, liquidus slope, and distribution coefficient respectively.

Using the values from Table 4.2, the constant M can be calculated as

$$M = \frac{(5e(-9))(5.56e(-8)) \ln(0.12 / 0.09)}{2.25(1 - 0.1613)(0.12 - 0.09)} = 1.41e(-15)$$

Therefore, the calculated SDAS is

$$\lambda_2 = 5.5 \left(1.41e(-15) \frac{922 - 588.7}{40 \cdot 1250} \right) = 0.00018 \text{ m}$$

Results of this calculation show that both FLOW3D and proposed algorithm predict correct rate of solidification of the liquid metal.

Table 4.2 Values of variables in Eq. (4.21)-(4.22) [43]

D(m ² /s)	Γ (K m)	c_e	c_0	k	m(K/%)	G(K/s)	v (K/s)
5e-9	5.56e-8	0.12	0.09	0.1613	2.25	40	1250

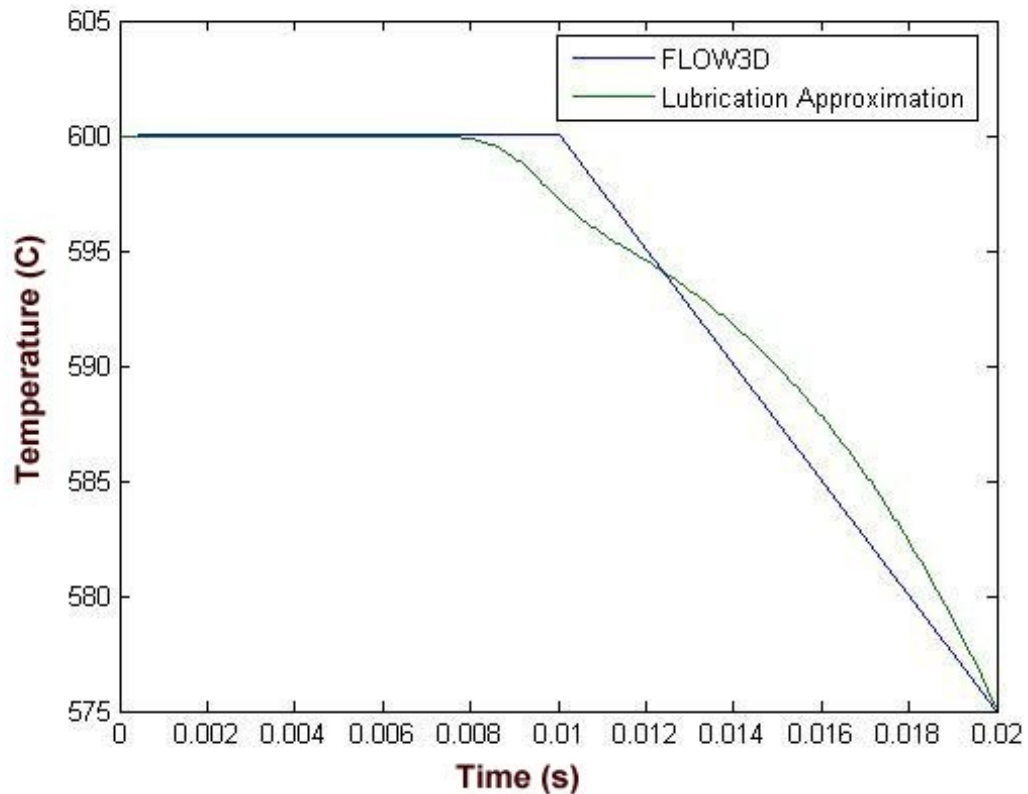


Figure 4.19 Temperature history at the centerline of section I in Figure 4.12; the cooling rate, v , is obtained from the slope of the curve.

4.13 Significant Improvement in Computational Speed

The most beneficial advantage of the proposed numerical algorithm is the substantial reduction in CPU time. Proposed algorithm required only 8 minutes to achieve a converged solution compared to 52 minutes required by the commercial software FLOW3D for the case shown in Figures 4.15 and 4.17. This remarkable reduction in computational time is an important feature of the proposed algorithm—the little error in its predictions are a small price to pay for a many-fold improvement in the computational speed.

4.14 Further Validation through a Parametric Study

Further verification of the proposed model was conducted by changing initial cavity thickness, channel-wall temperature, and liquid-metal velocity at the inlet. For the parametric study, the channel was considered to be of a constant height. The liquid-metal flow-length in all three cases was compared with the results obtained using FLOW3D. Comparisons of these numerical results are shown in Figures 4.20 – 4.22.

4.14.1 Effect of changes in ventilation-channel thickness

First parametric study was conducted by changing the thickness of the ventilation channel and keeping the wall temperature and liquid-metal initial velocity constant. Channel thickness was changed from 0.5 mm to 1 mm, with initial metal velocity set at 1 m/s and wall temperature kept constant at 60⁰ C. Flow analyses were run three times with a 0.25 mm increase in the ventilation channel thickness. Results of the study are shown in Figure 4.20 where flow length (the length the liquid metal moves in the ventilation channel before coming to a stop) is plotted as function of channel thickness. We see a remarkable convergence between predictions of our algorithm and FLOW3D. The monotonically-increasing result indicates an increase of the liquid-metal flow length can be expected by increasing the channel thickness. Doubling the channel thickness results leads to a similar increase in the flow length.

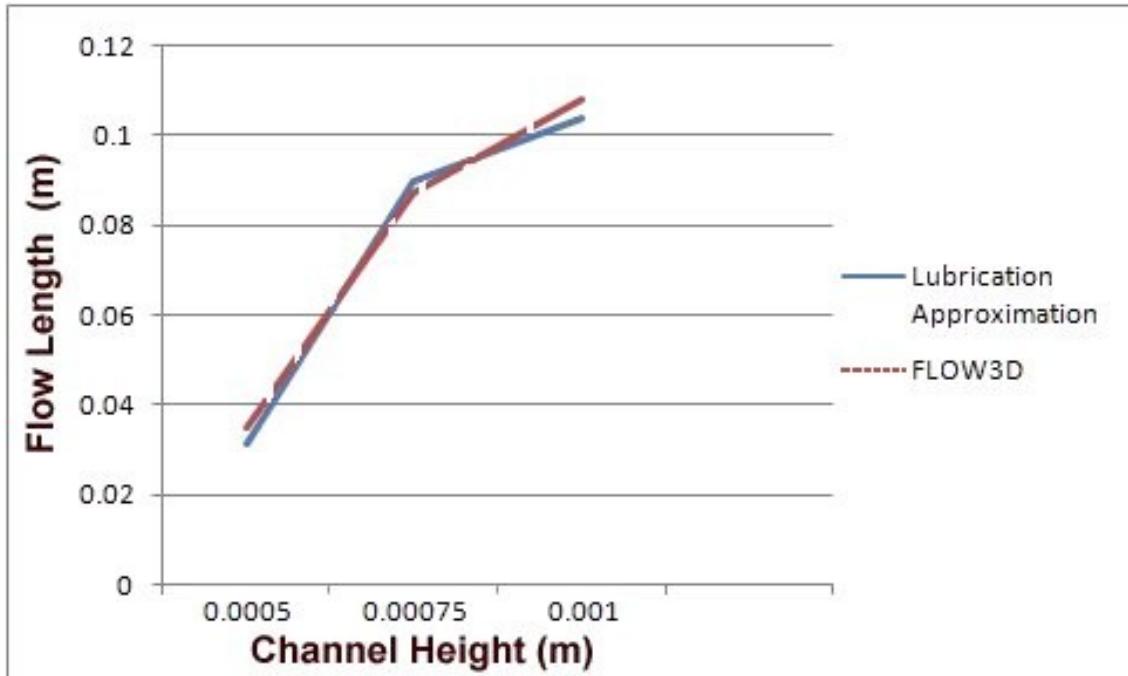


Figure 4.20 Metal flow-length vs. cavity thickness—result of the parametric study.

4.14.2 Effect of changes in wall temperature of the ventilation channel

Next parametric study was conducted by changing the temperature of the ventilation-channel walls. The channel thickness was set at 1 mm and the walls temperature was initially set at 60⁰ C with the initial liquid-metal velocity of 1 m/s. Four consecutive simulations were conducted with temperature of the wall increased by 20⁰ C each time. The relation between the wall temperature and the liquid-metal flow-length is shown in Figure 4.21. Once again, a remarkable match is obtained between the predictions of our proposed algorithm and FLOW3D. Results indicate that the wall temperature of the channel has only a slight effect on the flow length of the liquid-metal.

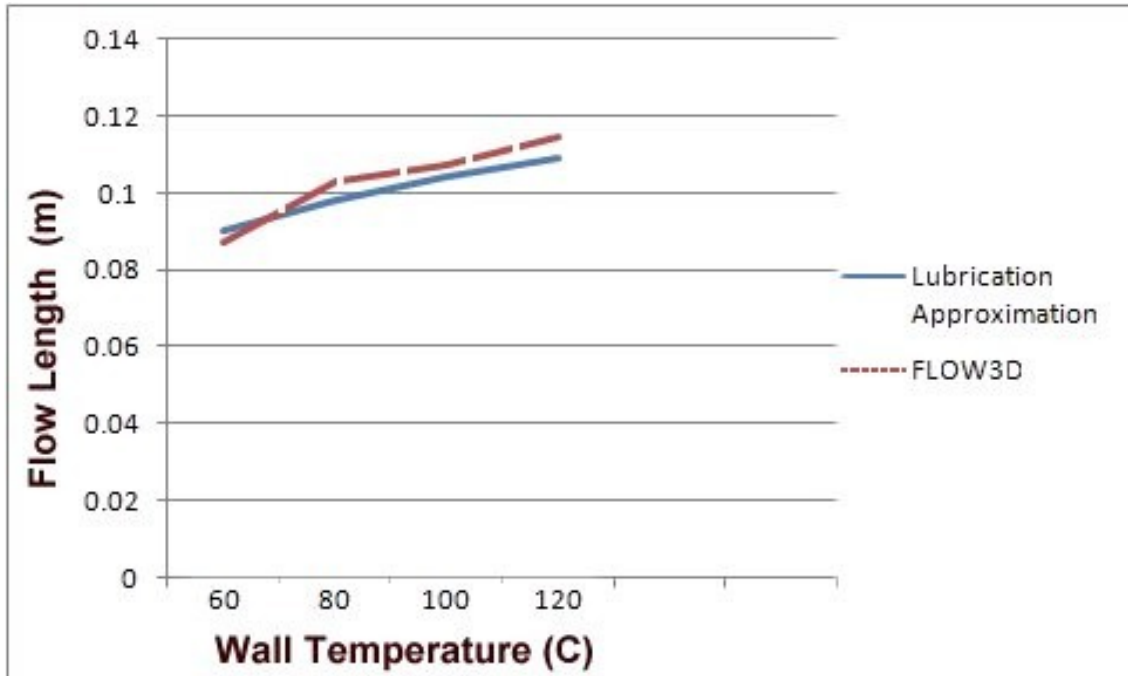


Figure 4.21 Metal flow-length vs. wall temperature—result of the parametric study.

4.14.3 Effect of changes in the initial metal velocity

Variation of the initial liquid-metal velocity and its effect on the flow length in the ventilation channel was also studied. The liquid-metal velocity was initially set at 0.5 m/s, with the ventilation channel thickness at 1 mm and the channel-wall temperature at 60°C. Four consecutive simulations were run while increasing the inlet metal-velocity by 0.25 m/s each time. The resultant correlation between the liquid-metal initial velocity and flow length is shown in Figure 4.22. Results indicate that flow length of the liquid metal increases with an increase in the metal velocity at the channel entrance. However, after the metal speed reaches 1.5 m/s, the increase in the flow length is much less than seen between the velocities of 0.75 – 1.5 m/s. It can be explained by the fact that convective heat-transfer coefficient between liquid metal and channel wall is an increasing function

of the metal velocity⁹: it increases with an increase in the metal velocity, and consequently, the liquid metal solidifies much faster in the channel. Also note that the accuracy of proposed algorithm deteriorates with an increase in the inlet speed. It can be explained by the fact that as the Reynolds number increases with an increase in the inlet speed of the liquid metal, turbulence in metal flow become more pronounced and the lubrication approximation employed in our algorithm is rendered increasingly less accurate.

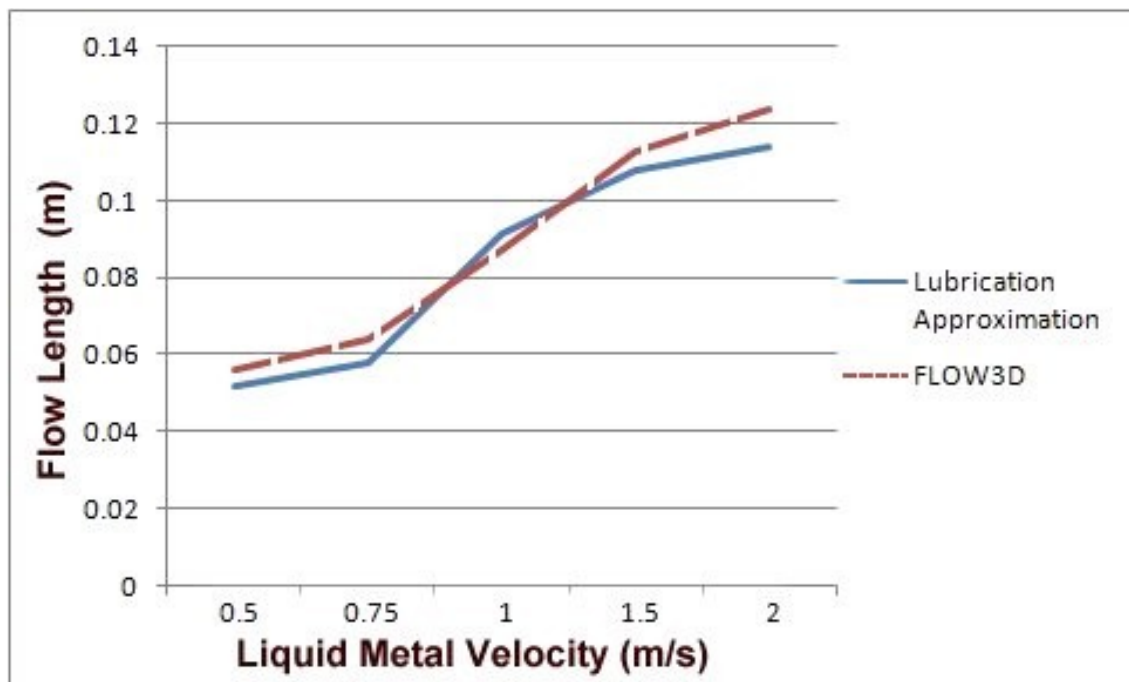


Figure 4.22 Metal flow-length vs. metal velocity at the entrance of the ventilation channel—result of the parametric study.

⁹ Increase in the liquid-metal velocity increases the Reynolds number, which in turn increases the Nusselt number. Since Nusselt number is proportional to the convective heat transfer coefficient, it increases heat transfer coefficient as well [8].

4.15 Summary and Conclusions

A numerical algorithm based on the lubrication approximation is developed to study transient flow and solidification in a thin ventilation channel of the die-cast die. Procedure consists of dividing casting into two regions. First solution is obtained in the main cavity where some commercial CFD software can be used to estimate flow and temperature distributions. Then the results at cut-off plane between the main cavity and ventilation channel are transferred into proposed algorithm as initial condition at the entrance of the ventilation channel for further analysis. The flow governing equations are integrated along the channel thickness using the lubrication approximation to yield governing equations for 2.5-D channel flow. The heat balance equation over the control volume yielded a temperature equation after incorporating the Stefan's condition for metal solidification. The finite difference method based on SIMPLE algorithm with staggered Cartesian grid arrangement is used for numerical approximation of the discretized governing equations. Volume of fluid method is utilized to define position of the free surface.

Results of the presented algorithm are validated by comparing them with predictions of the commercial CFD software FLOW3D[®] for a casting produced by the cold-chamber high-pressure die-cast process. The algorithm results are in good agreement (within 5%) with the predictions of the commercial CFD code as well as observations in actual castings. A good agreement is also achieved between the directly measured SDAS (secondary dendrite arms spacing) from an actual casting and the theoretically estimated SDAS using our algorithm and FLOW3D results.

A parametric study of on liquid metal flow and solidification in a ventilation channel using both the algorithm and FLOW3D results shows that the metal flow-length increases with the increase in the ventilation-channel thickness, wall temperature, and initial entrance velocity. Doubling the channel thickness leads to a similar increase in the flow length. Changes in the channel thickness influence the liquid-metal flow-length the most, and the channel wall temperature influences the flow length the least. These results can be used during the initial stages of the die-cast die design to estimate the length of the ventilation channel.

Although proposed algorithm did not predict the correct shape of the free surface of the liquid metal flow in the ventilation channel, and the shape of the solid-liquid interface, it correctly predicted flow length of the metal in the channel, and the location where solidification occurs along the channel length. Despite being slightly inaccurate, the most significant advantage of the proposed numerical algorithm is a substantial reduction in CPU time—the proposed algorithm required merely 8 minutes to achieve a converged solution compared to the 52 minutes required by the commercial software FLOW3D.

Chapter 5: Some Concerns and Future Research Directions

In the last two chapters, the algorithm developed using the lubrication approximation and the simpler laminar flow is shown to be a useful tool for predicting flow length, gap width, and temperature distribution during the flow of the liquid metal in thin channels. It was found to be especially useful for predicting the flow and solidification characteristics in the ventilation channels of the die-cast die.

However, the presented algorithm revealed some of its limitations as well. For example, the algorithm was developed and verified for simple rectangular channels. Future development of the algorithm should include derivation of the governing equations for flow in more complex shaped channels. To analyze the flow and solidification characteristics of liquid metal flowing around corners and in wavy shaped channels, it may be necessary to include the centripetal-type inertial forces as well as to use the curvilinear coordinates. Modifications of some basic assumptions may also be necessary. For example, assuming a slug-flow velocity profile rather than a parabolic profile may be closer to the real turbulent flow observed in the channel. These types of changes should be a part of the directions taken for future code development.

Presented algorithm was developed using a constant thermo-physical properties of the liquid metal. Future developments should include the use of the solidification model that utilizes the temperature-percentage of solids curve obtained from the solidification curve and measured using a thermocouple in conjunction with the Fourier interaction procedure [41]. It will allow one to use the presented algorithm to calculate flow and solidification characteristics for a variety of commercial alloys. For example, the solidification curve for the aluminum alloy A380 is shown in Figure 5.1. The curve shape

represents a balance between heat lost by the metal during solidification and heat generated during phase change. As observed in the figure, the latent heat of fusion is not a linear function of time. In binary alloys, the heat is released over a range of temperatures, so solidification does not progress in an orderly manner. First part of the solidification curve indicates rapid release of the latent heat, until all superheat is lost. However, solidification doesn't affect the liquid metal until the temperature falls below the liquidus line (point 1 on the solidification curve). This point is also called the temperature of liquidus arrest; this is the temperature at which the primary dendrites start to form. The next important point on the solidification curve, point 2, corresponds to the time close to the end of the solidification process. In order to better determine the characteristic points of the solidification process, the first-derivative curve is overlaid on the solidification curve and is shown in Figure 5.2. The first-derivative curve not only helps to determine changes in the solidification process, but also allows one to distinguish the point at which the primary and secondary dendrites are formed. As it can be observed in the figure, the first-derivative curve increases in value (up to the point 1 in Figure 5.2), indicates the beginning of solidification. And then, at the end of the solidification process (point 2 in Figure 5.2), it decreases. The region between points 1 and 2 on the first-derivative curve indicates free growth of the primary dendrites. The temperature range, as seen between points 1 and 2, is where dendrite arms increase in size, but are not yet touching each other. Point 2 is called the dendrite coherency point and corresponds to the fraction of solids in the liquid metal when dendrite arms come in contact with each other. After that point, free growth is not possible any more, and the region between point 2 and point 3 corresponds to the phenomena of dendrite thickening and formation of the rigid

skeleton. The region of the first-derivative curve between points 4 and 5, corresponds to the end of solidification. Derived relations will allow one to use a temperature-dependent latent heat value, instead of the usual constant one.

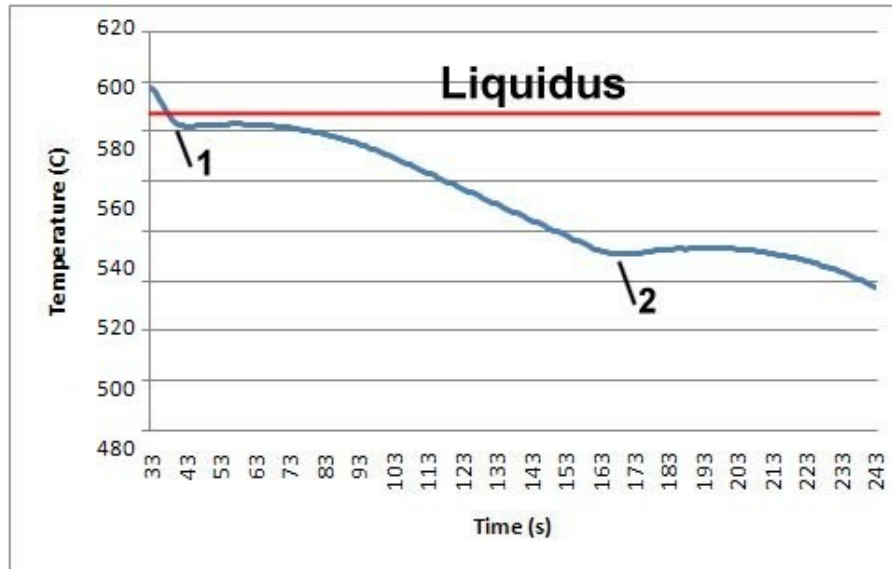


Figure 5.1 The measure solidification curve for aluminum A380 alloy.

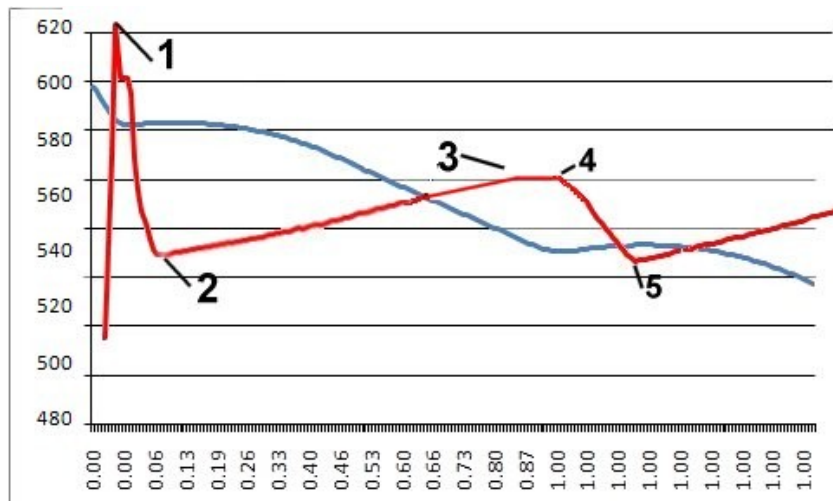


Figure 5.2 The first-derivative curve, obtained from the slope of the solidification curve shown in Figure 5.1, is overlaid on the original solidification curve. (Y axis is liquid metal temperature, X axis is percentage of solid in metal)

The melt viscosity does not play a significant role in the flow of liquid metal in thin channels. As was shown earlier using the Weber and Capillary numbers, the inertial force is the dominant force during metal flow through the ventilation channels. However, in order to increase the accuracy of predictions by the proposed algorithm, the change in the metal viscosity with an increase in solid volume fraction still needs to be included, even though most of the change in viscosity occurs towards the end of solidification [44] and hence may not affect the simulation accuracy much.

As shown in Figure 5.2, the primary dendrites start to form when the metal is still in the shot sleeve, i.e., at point 1. As the metal flows through the gates of the die-cast die, some of the dendrites break into smaller pieces, and are carried through the cavity of the die-cast die to the overflows and then to the ventilation channels, thus increasing the solid fraction in the melt. They usually become centers of nucleation for the equiaxed dendrites during further solidification. Note that due to a small channel thickness (0.5 mm), a high metal velocity, and a high solidification rate, the columnar dendrites cannot form during solidification inside the thin channels and the mushy zone doesn't develop to influence the metal flow. (As seen in Figure 5.3, the non-dendrite structure is dominant inside the thin ventilation channel.)

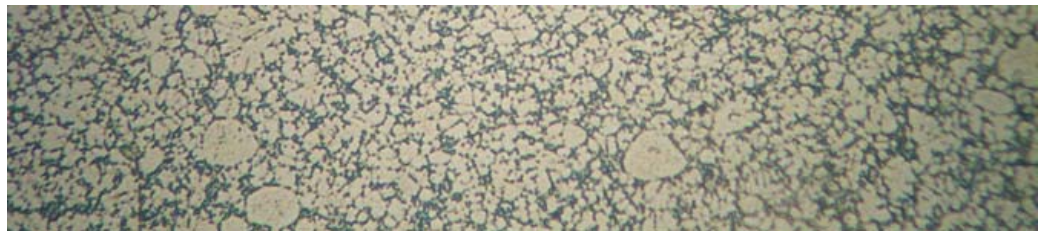


Figure 5.3 Non-dendrite structures seen in the micrograph of a section of a thin ventilation channel.

As a future development, the variable viscosity as a function of the liquid-metal temperature (and hence the solid fraction) can be used to improve the accuracy of the proposed algorithm. Such a development may improve the prediction accuracy for the analysis of metal flows in thicker channels (1-2 mm).

With an increase in the accuracy of temperature predictions, several other important parameters can be predicted as well. For example, after implementing all the proposed changes in the code, the simulation for predicting metal flow and solidification can also be used for the subsequent prediction of the macro and micro structures in thin channels.

The ideas presented in this final chapter, if implemented, may improve the accuracy of the proposed algorithm. However, their implementation will introduce additional nonlinearities (and hence additional iterative loops) in the proposed (simpler) solution, and hence may rob the method of its advantages of faster computational speed. Only some future research will answer these questions conclusively.

References

1. *About die casting*, The North American Die Casting Association, archived from the original on 2010-10-15, retrieved 2010-10-15.
2. W. F. Smith, '*Structure and Properties of Engineering Alloys*', McGraw-Hill, 1993.
3. Jean-Luc Chabert, et al. '*A History of Algorithms: From the Pebble to the Microchip*', 1999, Springer-Verlag.
4. C. Edwards, Jr. '*The Historical Development of the Calculus*', Springer-Verlag, 1997.
5. J. von Neumann and H. Goldstine, "Numerical Inverting of Matrices of High Order" Bulletin of the AMS, Nov. 1947
6. J. D. Hoffman , '*Numerical methods for engineers and scientists*', CRC Press, 2001
7. S.V. Patankar, '*Numerical heat transfer and fluid flow*', McGraw-Hill, 1980. Harlow,
8. F.H. Harlow, J.E. Welch, "*Numerical Calculation of Time-Dependent Viscous Incompressible Flow*", 1965 Phys. Fluids 8, 2182.
9. B.D. Nichols, C.W. Hirt, "Methods for Calculating Multidimensional, Transient Free Surface Flows Past Bodies", *Proc. of the First International Conf. On Num. Ship Hydrodynamics*, Gaithersburg, ML, Oct. 20-23 1975.
10. R.K. Shah, M.S. Bhatti, '*Laminar convective heat transfer in ducts*' *Handbook of Single Phase convective heat transfer*', Kakac S. Shah R.K., and Aung W., Willey, New York, 1987
11. C.W. Hirt, B.D. Nichols, "Volume of fluid (VOF) method for the dynamics of free boundaries", *J. Comp. Phys.* 39, pp. 201-208 1981.
12. B. R. Munson, A. P. Rothmayer, T. H. Okiishi, W. W. Huebsch, '*Fundamentals of Fluid Mechanics*', Wiley, New York, 2012.

13. A.Z. Szeri, '*Tribology friction, lubrication, and wear*', McGraw-Hill, 1979
14. M. Epstein, F. B. Cheung, 'Complex freezing-melting interfaces in fluid flow', *Fluid Mech.*, 15, pp. 293-319, 1983.
15. B. Weigard, H. Beer, 'Ice-formation phenomena for water flow inside a cooled parallel channel: an experimental and theoretical investigation of wavy ice layers', *Int. J. Heat Mass Transfer*, Vol. 36 No. 3 pp. 685—693, 1993
16. A. Rouboa, E. Monteiro, 'Heat transfer in multi-block grid during solidification: Performance of finite differences and finite volume method', *J. Material Processing Technology*, 204, pp. 541-458, 2008.
- 17.B. Mochnacki, E. Majchrzak, 'Numerical modelling of casting solidification using generalized finite difference method', *Material Science Forum*, 638-642, pp. 2676-2681, 2010
18. X. Yao, M.S. Dargusch, A.K. Dahle, C.J. Davidson, D.H. StJohn, 'Investigation into the effects of nucleation parameters on grain formation during solidification using a cellular automation—finite control volume method', *J. Materials Research*, 23(9), pp. 2312-2325, 2008
19. H. Montazeri, M. Bussmann, J. Mostaghimi, 'Accurate implementation of forcing term for two-phase flows into SIMPLE algorithm', *Int. J. of Multiphase Flow*, 45, pp. 40-52, 2012
20. Z. Domanski, M. Ciesielski, B. Mochnacki, 'Application of control volume method using the Voronoi tessellation in numerical modelling of solidification process', *AIP Conference Proceedings*, pp. 17-26, 2010
- 21.V. Grozdanic, 'Finite-difference methods for simulating the solidification of castings',

Matriali in Tehnologije, 43 (5) pp. 233-237, 2009

22. C. Yang, C. Li, 'Application of SIMPLE algorithm on non—staggered grid to numerical simulation of the Yellow River flow and sediment transport in Shapotou Reach', *ISWREP 2011 – Proceedings of 2011 International Symposium on Water Resurce and Environmental protection*, 1, No. 5893085, pp. 626—629.
23. M. Larmaei, T. –F. Mahdi. 'Analysis of SIMPLE algorithm for depth averaged simulations', *Environmental hydraulics-proceedings of the 6th International symposium on environmental hydraulics*, 2, pp. 967-972, 2010.
24. A. K. Rastogi, 'Predictions of heat and mass transfer in open channels', *J. of the Hydraulics Division, ASCE*, 104(3), pp. 397-420, 1978.
- 25 Y. S. Chen, S.M. Kim, 'Computation of turbulent flow using an extended $k - \varepsilon$ turbulence closure model', *NASA, CR—179204*, pp. 21-25.
- 26 V. Yakhot, S.A. Orszag, S. Thangam, T. B. Speziale, 'Development of turbulence models for shear flow by a double expansion technique', *Phys. Fluids A*, 4(9) pp. 1510—1520, 1992.
27. H. S. Hele-Shaw, 'The flow of water', *Nature, London* vol. 58, pp. 34-38, 1898.
28. K. Venkatesan, R. Shivpuri, 'Numerical simulation and comparison with water modeling studies of the inertia dominated cavity filling in die casting', *Simulation of Materials Processing: Theory, Methods and Applications*, edited by S. F. Shen and P. R. Dawson - Balkema, Rotterdam, pp. 1203-1211, 1995.

29. V. Aleksenko, V.V. Nakoryakov, B.G. Pokusaev, 'Wave formation on a vertical falling liquid film', *AIChE J.* vol. 31, pp. 1446-1458, 1985.
30. S.C. Gupta, 'The Classical Stefan Problem: basic concepts, modelling and analysis', JAI Press, 2003.
31. J.K. Carpenter, P.H. Steen, 'Heat transfer and solidification in planar-flow melt-spinning: high wheel speeds', *Int. J Mass Transfer*, V 40, N 9 pp. 1993-2007, 1997.
32. NADCA Product specification for die castings, Section 3 Table A-3-2-97
33. R. Mizanur, K. Siddique, R. Khayat, 'Influence of inertia and topography in thin-cavity' *Physics of fluids*, V.14 N. 5, pp. 1703-1719 2002.
34. Ch. Karcher, P.H. Steen, 'High Reynolds number flow in a narrow gap driven by solidification', *Physics of fluids*, vol. 13, number 4, pp 834-840, 2001.
35. J.K. Carpenter, P.H. Steen, 'Heat transfer and solidification in planar-flow melt-spinning: high wheel speeds', *Int. J. Heat Mass Transfer* Vol. 40, No 9, pp 1993-2007, 1997.
36. A. Reikher, K. M. Pillai 'A fast numerical simulation for modelling simultaneous metal flow and solidification in thin cavities using the lubrication approximation' *Numerical Heat Transfer Part A*, V63, pp. 75-100, 2013.
37. K. Venkatesan, R. Shivpuri, 'Numerical simulation and comparison with water modeling studies of the inertia dominated cavity filling in die casting', *Simulation of Materials Processing: Theory, Methods and Applications*, edited by S. F. Shen and P. R. Dawson, Balkema, Rotterdam, pp. 1203-1211 1995.
38. B. J. Hamrock, 'Fundamentals of Fluid Film Lubrication', McGraw-Hill, New York, 1994.
39. FLOW3D® Flow Science, www.flow3d.com.

- 40 C. Kwak, C. Kiris, '*Computation of Viscous Incompressible Flows*', Springer, 2011.
- 41.E. Fras, 'A new concept in thermal analysis of casting', *Transactions of American Foundarymen's Society*, 1993. V.101: p. 505-511.
- 42.W. Kurz and D.J. Fisher, 'Dendrite growth at the limit of stability: tip radius and spacing', *Acta Metall.*, 1981, vol. 29, pp. 11–20.
- 43.J. E. Hatch, '*Aluminum: Properties and Physical Metallurgy*', ASM International, 1984.
44. G.E.Totten, K. Funatani, L. Xie, '*Handbook of metallurgic process design*', Marcel Dekker Inc., 2004

Appendix A

Reynolds lubrication equation after including the effect of inertia

Governing equation of the transient flow in non-dimensional form is given as follows:

Momentum equations

$$\begin{cases} \delta \left(\frac{\partial u}{\partial t} + u \frac{\partial u}{\partial x} + v \frac{\partial u}{\partial y} \right) = \frac{\partial^2 u}{\partial z^2} - \frac{\partial p}{\partial x} \\ \delta \left(\frac{\partial v}{\partial t} + u \frac{\partial v}{\partial x} + v \frac{\partial v}{\partial y} \right) = \frac{\partial^2 v}{\partial z^2} - \frac{\partial p}{\partial y} \end{cases} \quad (\text{A1})$$

where $\delta = \varepsilon^2 \text{Re}$ modified Reynolds number.

$$\text{Re - Reynolds number} \left(= \frac{\rho \bar{V} L}{\mu} \right)$$

$$\varepsilon - \text{cavity aspect ratio} \left(= \frac{H_0}{L} \right)$$

Continuity equation

$$\frac{\partial u}{\partial x} + \frac{\partial v}{\partial y} = 0 \quad (\text{A2})$$

The dimensionless variables are defined as

$$x = \frac{X}{L}, \quad y = \frac{Y}{L}, \quad z = \frac{Z}{H}, \quad h = \frac{H}{H_0}, \quad u = \frac{u}{\bar{V}}, \quad v = \frac{v}{\bar{V}}, \quad w = \left(\frac{H_0}{L} \right)^2 \frac{L}{\mu \bar{V}} P$$

where \bar{V} is a reference velocity, u , v , and w are the velocities in x , y , and z direction, and H is the thickness of the cavity. Since velocity w is vanishing at the top and bottom boundaries, and its variation is negligible owing to a small thickness of the cavity, it will

be set to zero. Using the continuity equation, equation (A1) can be expressed in a convergent form as

$$\left\{ \begin{aligned} \delta \left[\frac{\partial u}{\partial t} + \frac{\partial u^2}{\partial x} + \frac{\partial uv}{\partial y} \right] &= \frac{\partial^2 u}{\partial z^2} - \frac{\partial p}{\partial x} \\ \delta \left[\frac{\partial v}{\partial t} + \frac{\partial uv}{\partial x} + \frac{\partial v^2}{\partial y} \right] &= \frac{\partial^2 v}{\partial z^2} - \frac{\partial p}{\partial y} \end{aligned} \right. \quad (\text{A3})$$

On integrating equation (A3) over the thickness of the cavity yields

$$\left\{ \begin{aligned} \delta \left[\int_0^h \frac{\partial u}{\partial t} dz + \int_0^h \frac{\partial u^2}{\partial x} dz + \int_0^h \frac{\partial uv}{\partial y} dz \right] + \int_0^h \frac{\partial p}{\partial x} dz &= \int_0^h \frac{\partial^2 u}{\partial z^2} dz \\ \delta \left[\int_0^h \frac{\partial v}{\partial t} dz + \int_0^h \frac{\partial uv}{\partial x} dz + \int_0^h \frac{\partial v^2}{\partial y} dz \right] + \int_0^h \frac{\partial p}{\partial y} dz &= \int_0^h \frac{\partial^2 v}{\partial z^2} dz \end{aligned} \right. \quad (\text{A4})$$

We will assume parabolic form of velocity distribution in x and y direction:

$$u = U(x, y, t)(z^2 - zh) \quad (\text{A5})$$

$$v = V(x, y, t)(z^2 - zh) \quad (\text{A6})$$

On substituting velocity distribution equations (A5) and (A6) into equation (A4), we get

$$\left\{ \begin{aligned} \delta \left[\int_0^h \frac{\partial \left(U(z^2 - zh) \right)}{\partial t} dz + \int_0^h \frac{\partial \left(U^2(z^2 - zh)^2 \right)}{\partial x} dz + \int_0^h \frac{\partial \left(UV(z^2 - zh)^2 \right)}{\partial y} dz \right] \\ + \int_0^h \frac{\partial p}{\partial x} dz = \int_0^h \frac{\partial^2 \left(U(z^2 - zh) \right)}{\partial z^2} dz \\ \delta \left[\int_0^h \frac{\partial \left(V(z^2 - zh) \right)}{\partial t} dz + \int_0^h \frac{\partial \left(UV(z^2 - zh)^2 \right)}{\partial x} dz + \int_0^h \frac{\partial \left(V^2(z^2 - zh)^2 \right)}{\partial y} dz \right] \\ + \int_0^h \frac{\partial p}{\partial y} dz = \int_0^h \frac{\partial^2 \left(V(z^2 - zh) \right)}{\partial z^2} dz \end{aligned} \right. \quad (\text{A7})$$

$$\delta \left[\int_0^h \frac{\partial(U(z^2 - zh))}{\partial t} dz + \int_0^h \frac{\partial(U^2(z^2 - zh)^2)}{\partial x} dz + \int_0^h \frac{\partial(UV(z^2 - zh)^2)}{\partial y} dz \right] + \int_0^h \frac{\partial p}{\partial x} dz = \int_0^h \underbrace{\frac{\partial}{\partial z} \left(\frac{\partial U z^2}{\partial z} - \frac{\partial U z h}{\partial z} \right)}_X dz \quad (\text{A8})$$

$$\delta \left[\int_0^h \frac{\partial(V(z^2 - zh))}{\partial t} dz + \int_0^h \frac{\partial(UV(z^2 - zh)^2)}{\partial x} dz + \int_0^h \frac{\partial(V^2(z^2 - zh)^2)}{\partial y} dz \right] + \int_0^h \frac{\partial p}{\partial y} dz = \int_0^h \underbrace{\frac{\partial}{\partial z} \left(\frac{\partial V z^2}{\partial z} - \frac{\partial V z h}{\partial z} \right)}_{XI} dz \quad (\text{A9})$$

Using the property

$$\frac{\partial(f(x)g(x))}{\partial x} = g \frac{\partial f(x)}{\partial x} + f \frac{\partial g(x)}{\partial x} \quad (\text{A10})$$

the term X in equation (A8) can be written as

$$X = \frac{\partial}{\partial z} \left(\frac{\partial U z^2}{\partial z} - U h \right) \quad (\text{A11})$$

And then term XI in Eq.(A9) can be written as

$$XI = \frac{\partial}{\partial z} \left[\frac{\partial V z^2}{\partial z} - V h \right]$$

Since there are no changes in U and V velocities in z direction i.e., $\frac{\partial U h}{\partial z} = 0$ and $\frac{\partial V h}{\partial z} = 0$

X and XI further simplifies to

$$X = \frac{\partial}{\partial z} \left(\frac{\partial U z^2}{\partial z} \right)$$

$$XI = \frac{\partial}{\partial z} \left(\frac{\partial Vz^2}{\partial z} \right)$$

Opening brackets in equations (A8) and (A9) as well as temporarily eliminating the common z direction integral yields:

$$\begin{aligned} & \delta \left[\frac{\partial}{\partial t} U(z^2 - zh) + \underbrace{\frac{\partial}{\partial x} U^2 \{z^4 - 2z^3h + z^2h^2\}}_{XX} + \underbrace{\frac{\partial}{\partial y} UV \{z^4 - 2z^3h + z^2h^2\}}_{XXX} \right] + \frac{\partial p}{\partial x} \\ & = \frac{\partial}{\partial z} \left(\frac{\partial Uz^2}{\partial z} \right) \end{aligned} \quad (A11)$$

$$\begin{aligned} & \delta \left[\frac{\partial}{\partial t} V(z^2 - zh) + \underbrace{\frac{\partial}{\partial x} UV \{z^4 - 2z^3h + z^2h^2\}}_{XXI} + \underbrace{\frac{\partial}{\partial y} V^2 \{z^4 - 2z^3h + z^2h^2\}}_{XXXI} \right] + \frac{\partial p}{\partial y} \\ & = \frac{\partial}{\partial z} \left(\frac{\partial Vz^2}{\partial z} \right) \end{aligned} \quad (A12)$$

Opening brackets and rearranging terms in equations (A11) and (A12) results in the following equations:

$$\frac{\partial}{\partial t} U(z^2 - zh) = z^2 \frac{\partial U}{\partial t} - \frac{\partial(Uh)}{\partial t} z = z^2 \frac{\partial U}{\partial t} - zh \frac{\partial U}{\partial t} - zU \frac{\partial h}{\partial t} \quad (A13)$$

$$\begin{aligned} XX &= \frac{\partial}{\partial x} U^2 \{z^4 - 2z^3h + z^2h^2\} = z^4 \frac{\partial U^2}{\partial x} - 2z^3 \frac{\partial(U^2h)}{\partial x} + z^2 \frac{\partial(Uh)^2}{\partial x} \\ &= \frac{\partial U^2}{\partial x} z^4 - 2z^3h \frac{\partial U^2}{\partial x} - 2z^3U^2 \frac{\partial h}{\partial x} + z^2h^2 \frac{\partial U^2}{\partial x} + z^2U^2 \frac{\partial h^2}{\partial x} \\ &= \left(\frac{\partial U^2}{\partial x} z^4 - 2z^3h \frac{\partial U^2}{\partial x} + z^2h^2 \frac{\partial U^2}{\partial x} \right) + \left(-2z^3U^2 \frac{\partial h}{\partial x} + 2z^2U^2h \frac{\partial h}{\partial x} \right) \\ &= \frac{\partial U^2}{\partial x} (z^4 - 2z^3h + z^2h^2) + 2U^2 \frac{\partial h}{\partial x} (z^2h + z^3) \end{aligned} \quad (A14)$$

$$\begin{aligned}
XXI &= \frac{\partial}{\partial x} UV \left\{ z^4 - 2z^3h + z^2h^2 \right\} = z^4 \frac{\partial UV}{\partial x} - 2z^3 \frac{\partial(UVh)}{\partial x} + z^2 \frac{\partial(UVh^2)}{\partial x} \\
&= \frac{\partial UV}{\partial x} z^4 - 2z^3h \frac{\partial UV}{\partial x} - 2z^3UV \frac{\partial h}{\partial x} + z^2h^2 \frac{\partial UV}{\partial x} + z^2UV \frac{\partial h^2}{\partial x} \\
&= \left(\frac{\partial UV}{\partial x} z^4 - 2z^3h \frac{\partial UV}{\partial x} + z^2h^2 \frac{\partial UV}{\partial x} \right) + \left(-2z^3UV \frac{\partial h}{\partial x} + 2z^2UVh \frac{\partial h}{\partial x} \right) \\
&= \frac{\partial UV}{\partial x} \left(z^4 - 2z^3h + z^2h^2 \right) + 2UV \frac{\partial h}{\partial x} \left(z^2h + z^3 \right)
\end{aligned} \tag{A15}$$

$$\begin{aligned}
XXX &= \frac{\partial VU}{\partial y} \left\{ z^4 - 2z^3h + z^2h^2 \right\} = z^4 \frac{\partial UV}{\partial y} - 2z^3 \frac{\partial(UVh)}{\partial y} + z^2 \frac{\partial(UVh^2)}{\partial y} \\
&= z^4 \frac{\partial UV}{\partial y} - 2z^3h \frac{\partial UV}{\partial y} - 2z^3UV \frac{\partial h}{\partial y} + z^2h^2 \frac{\partial UV}{\partial y} + z^2UV \frac{\partial h^2}{\partial y} \\
&= \left(z^4 \frac{\partial UV}{\partial y} - 2z^3h \frac{\partial UV}{\partial y} + z^2h^2 \frac{\partial UV}{\partial y} \right) + \left(2z^2hUV \frac{\partial h}{\partial y} - 2z^3UV \frac{\partial h}{\partial y} \right) \\
&= \frac{\partial UV}{\partial y} \left(z^4 - 2z^3h + z^2h^2 \right) + 2UV \frac{\partial h}{\partial y} \left(z^2h - z^3 \right)
\end{aligned} \tag{A16}$$

$$\frac{\partial}{\partial t} V \left(z^2 - zh \right) = z^2 \frac{\partial V}{\partial t} - \frac{\partial(Vh)}{\partial t} z = z^2 \frac{\partial V}{\partial t} - zh \frac{\partial V}{\partial t} - zV \frac{\partial h}{\partial t} \tag{A17}$$

$$\begin{aligned}
XXXI &= \frac{\partial V^2}{\partial y} \left\{ z^4 - 2z^3h + z^2h^2 \right\} = z^4 \frac{\partial V^2}{\partial y} - 2z^3 \frac{\partial(V^2h)}{\partial y} + z^2 \frac{\partial(V^2h^2)}{\partial y} \\
&= z^4 \frac{\partial V^2}{\partial y} - 2z^3h \frac{\partial V^2}{\partial y} - 2z^3V^2 \frac{\partial h}{\partial y} + z^2h^2 \frac{\partial V^2}{\partial y} + z^2V^2 \frac{\partial h^2}{\partial y} \\
&= \left(z^4 \frac{\partial V^2}{\partial y} - 2z^3h \frac{\partial V^2}{\partial y} + z^2h^2 \frac{\partial V^2}{\partial y} \right) + \left(2z^2hV^2 \frac{\partial h}{\partial y} - 2z^3V^2 \frac{\partial h}{\partial y} \right) \\
&= \frac{\partial V^2}{\partial y} \left(z^4 - 2z^3h + z^2h^2 \right) + 2V^2 \frac{\partial h}{\partial y} \left(z^2h - z^3 \right)
\end{aligned} \tag{A18}$$

Substitution of the above-derived terms into the original equations, Eqs. (A11) and (A12), results in

$$\left\{ \begin{aligned}
& \frac{\partial U}{\partial t} (z^2 - zh) - \frac{\partial h}{\partial t} zU + \frac{\partial U^2}{\partial x} (z^4 - 2z^3h + z^2h^2) + 2U^2 \frac{\partial h}{\partial x} (z^2h + z^3) \\
& + \frac{\partial UV}{\partial y} (z^4 - 2z^3h + z^2h^2) + 2UV \frac{\partial h}{\partial y} (z^2h + z^3) = \frac{\partial}{\partial z} \left(\frac{\partial Uz^2}{\partial z} \right) - \frac{\partial p}{\partial x} \\
& \frac{\partial V}{\partial t} (z^2 - zh) - \frac{\partial h}{\partial t} zV + \frac{\partial UV}{\partial x} (z^4 - 2z^3h + z^2h^2) + 2UV \frac{\partial h}{\partial x} (z^2h + z^3) \\
& \frac{\partial V^2}{\partial y} (z^4 - 2z^3h + z^2h^2) + 2V^2 \frac{\partial h}{\partial y} (z^2h - z^3) = \frac{\partial}{\partial z} \left(\frac{\partial Vz^2}{\partial z} \right) - \frac{\partial p}{\partial y}
\end{aligned} \right. \quad (\text{A19})$$

Rearranging terms in Eq. (A19) leads to

$$\left\{ \begin{aligned}
& \frac{\partial U}{\partial t} (z^2 - zh) - \frac{\partial h}{\partial t} zU + \underbrace{\left(\frac{\partial U^2}{\partial x} + \frac{\partial UV}{\partial y} \right) (z^4 - 2z^3h + z^2h^2)}_I + \underbrace{\left(2U^2 \frac{\partial h}{\partial x} + 2UV \frac{\partial h}{\partial y} \right) (z^2h + z^3)}_{II} \\
& = \frac{\partial}{\partial z} \left(\underbrace{\frac{\partial^2 Uz^2}{\partial z}}_{III} \right) - \frac{\partial p}{\partial x} \\
& \frac{\partial V}{\partial t} (z^2 - zh) - \frac{\partial h}{\partial t} zV + \underbrace{\left(\frac{\partial UV}{\partial x} + \frac{\partial V^2}{\partial y} \right) (z^4 - 2z^3h + z^2h^2)}_{IX} + \underbrace{\left(2UV \frac{\partial h}{\partial x} + 2V^2 \frac{\partial h}{\partial y} \right) (z^2h + z^3)}_{IIX} \\
& = \frac{\partial}{\partial z} \left(\underbrace{\frac{\partial Vz^2}{\partial z}}_{IIIX} \right) - \frac{\partial p}{\partial y}
\end{aligned} \right. \quad (\text{A20})$$

We will bring back the z direction integration and integrate along the z direction all the terms of equation (A20) in the following section.

$$\begin{aligned}
\frac{\partial U}{\partial t} \left[\int_0^h (z^2 - zh) dz \right] &= \frac{\partial U}{\partial t} \left[\int_0^h z^2 dz - h \int_0^h z dz \right] = \frac{\partial U}{\partial t} \left[\frac{z^3}{3} \Big|_0^h - h \frac{z^2}{2} \Big|_0^h \right] \\
&= -\frac{1}{6} \frac{\partial U}{\partial t} h^3
\end{aligned} \quad (\text{A21})$$

$$\frac{\partial h}{\partial t} U \int_0^h z dz = \frac{\partial h}{\partial t} U \frac{z^2}{2} \Big|_0^h = \frac{1}{2} \frac{\partial h}{\partial t} U h^2 \quad (\text{A22})$$

Integrating term I results in

$$\begin{aligned}
& \left(\frac{\partial U^2}{\partial x} + \frac{\partial UV}{\partial y} \right) \int_0^h z^4 dz - 2h \left(\frac{\partial U^2}{\partial x} + \frac{\partial UV}{\partial y} \right) \int_0^h z^3 dz + h^2 \left(\frac{\partial U^2}{\partial x} + \frac{\partial UV}{\partial y} \right) \int_0^h z^2 dz \\
&= \left(\frac{\partial U^2}{\partial x} + \frac{\partial UV}{\partial y} \right) \frac{z^5}{5} \Big|_0^h - 2h \left(\frac{\partial U^2}{\partial x} + \frac{\partial UV}{\partial y} \right) \frac{z^4}{4} \Big|_0^h + h^2 \left(\frac{\partial U^2}{\partial x} + \frac{\partial UV}{\partial y} \right) \frac{z^3}{3} \Big|_0^h \\
&= \left(\frac{\partial U^2}{\partial x} + \frac{\partial UV}{\partial y} \right) \frac{h^5}{5} - 2h \left(\frac{\partial U^2}{\partial x} + \frac{\partial UV}{\partial y} \right) \frac{h^4}{4} + h^2 \left(\frac{\partial U^2}{\partial x} + \frac{\partial UV}{\partial y} \right) \frac{h^3}{3} \\
&= \left(\frac{\partial U^2}{\partial x} + \frac{\partial UV}{\partial y} \right) \frac{h^5}{5} - \left(\frac{\partial U^2}{\partial x} + \frac{\partial UV}{\partial y} \right) \frac{h^5}{2} + \left(\frac{\partial U^2}{\partial x} + \frac{\partial UV}{\partial y} \right) \frac{h^5}{3} = \frac{1}{30} \left(\frac{\partial U^2}{\partial x} + \frac{\partial UV}{\partial y} \right) h^5
\end{aligned} \tag{A23}$$

Integrating term *IX* results in

$$\begin{aligned}
& \left(\frac{\partial UV}{\partial x} + \frac{\partial V^2}{\partial y} \right) \int_0^h z^4 dz - 2h \left(\frac{\partial UV}{\partial x} + \frac{\partial V^2}{\partial y} \right) \int_0^h z^3 dz + h^2 \left(\frac{\partial UV}{\partial x} + \frac{\partial V^2}{\partial y} \right) \int_0^h z^2 dz \\
&= \left(\frac{\partial UV}{\partial x} + \frac{\partial V^2}{\partial y} \right) \frac{z^5}{5} \Big|_0^h - 2h \left(\frac{\partial UV}{\partial x} + \frac{\partial V^2}{\partial y} \right) \frac{z^4}{4} \Big|_0^h + h^2 \left(\frac{\partial UV}{\partial x} + \frac{\partial V^2}{\partial y} \right) \frac{z^3}{3} \Big|_0^h \\
&= \left(\frac{\partial UV}{\partial x} + \frac{\partial V^2}{\partial y} \right) \frac{h^5}{5} - 2h \left(\frac{\partial UV}{\partial x} + \frac{\partial V^2}{\partial y} \right) \frac{h^4}{4} + h^2 \left(\frac{\partial UV}{\partial x} + \frac{\partial V^2}{\partial y} \right) \frac{h^3}{3} \\
&= \left(\frac{\partial UV}{\partial x} + \frac{\partial V^2}{\partial y} \right) \frac{h^5}{5} - \left(\frac{\partial UV}{\partial x} + \frac{\partial V^2}{\partial y} \right) \frac{h^5}{2} + \left(\frac{\partial UV}{\partial x} + \frac{\partial V^2}{\partial y} \right) \frac{h^5}{3} = \frac{1}{30} \left(\frac{\partial UV}{\partial x} + \frac{\partial V^2}{\partial y} \right) h^5
\end{aligned} \tag{A24}$$

Integrating term *II* results in

$$\begin{aligned}
& 2 \left(U^2 \frac{\partial h}{\partial x} + UV \frac{\partial h}{\partial y} \right) \int_0^h (z^2 h - z^3) dz = 2 \left(U^2 \frac{\partial h}{\partial x} + UV \frac{\partial h}{\partial y} \right) \left(\int_0^h z^2 h dz - \int_0^h z^3 dz \right) \\
&= 2 \left(U^2 \frac{\partial h}{\partial x} + UV \frac{\partial h}{\partial y} \right) \left(\frac{z^3}{3} h \Big|_0^h - \frac{z^4}{4} \Big|_0^h \right) \\
&= 2 \left(U^2 \frac{\partial h}{\partial x} + UV \frac{\partial h}{\partial y} \right) \left(\frac{h^4}{3} - \frac{h^4}{4} \right) = \frac{1}{6} \left(U^2 \frac{\partial h}{\partial x} + UV \frac{\partial h}{\partial y} \right) h^4
\end{aligned} \tag{A25}$$

Integrating term *IIX* results in

$$\begin{aligned}
& 2\left(UV \frac{\partial h}{\partial x} + V^2 \frac{\partial h}{\partial y}\right) \int_0^h (z^2 h - z^3) dz = 2\left(UV \frac{\partial h}{\partial x} + V^2 \frac{\partial h}{\partial y}\right) \left(\int_0^h z^2 h dz - \int_0^h z^3 dz\right) \\
& = 2\left(UV \frac{\partial h}{\partial x} + V^2 \frac{\partial h}{\partial y}\right) \left(\frac{z^3}{3} h \Big|_0^h - \frac{z^4}{4} \Big|_0^h\right) \\
& = 2\left(UV \frac{\partial h}{\partial x} + V^2 \frac{\partial h}{\partial y}\right) \left(\frac{h^4}{3} - \frac{h^4}{4}\right) = \frac{1}{6} \left(UV \frac{\partial h}{\partial x} + V^2 \frac{\partial h}{\partial y}\right) h^4
\end{aligned} \tag{A26}$$

Integrating term *III* results in

$$\frac{\partial}{\partial z} \left(\frac{\partial U z^2}{\partial z} \right) = \int_0^h \left(\frac{\partial}{\partial z} \left(\frac{\partial U z^2}{\partial z} \right) dz \right) = \frac{\partial U z^2}{\partial z} = 2U z \Big|_0^h = 2Uh \tag{A27}$$

Integrating term *III*X results in

$$\frac{\partial}{\partial z} \left(\frac{\partial V z^2}{\partial z} \right) = \int_0^h \left(\frac{\partial}{\partial z} \left(\frac{\partial V z^2}{\partial z} \right) dz \right) = \frac{\partial V z^2}{\partial z} = 2V z \Big|_0^h = 2Vh \tag{A28}$$

$$\begin{aligned}
& \frac{\partial V}{\partial t} \left[\int_0^h (z^2 - zh) \right] = \frac{\partial V}{\partial t} \left[\int_0^h z^2 dz - h \int_0^h z dz \right] = \frac{\partial V}{\partial t} \left[\frac{z^3}{3} \Big|_0^h - h \frac{z^2}{2} \Big|_0^h \right] \\
& = -\frac{1}{6} \frac{\partial V}{\partial t} h^3
\end{aligned} \tag{A29}$$

$$\frac{\partial h}{\partial t} V \int_0^h z = \frac{\partial h}{\partial t} V \frac{z^2}{2} \Big|_0^h = \frac{1}{2} \frac{\partial h}{\partial t} V h^2 \tag{A30}$$

On substituting back all the above terms into equation (A20), we get

$$\delta \left(-\frac{1}{6} \frac{\partial U}{\partial t} h^3 - \frac{1}{2} \frac{\partial h}{\partial t} U h^2 + \frac{1}{30} \frac{\partial U^2}{\partial x} h^5 + \frac{1}{6} U^2 \frac{\partial h}{\partial x} h^4 + \frac{1}{6} UV \frac{\partial h}{\partial y} + \frac{1}{30} \frac{\partial UV}{\partial y} h^5 \right) = 2Uh - \frac{\partial p}{\partial x} h \tag{A31}$$

$$\delta \left(-\frac{1}{6} \frac{\partial V}{\partial t} h^3 - \frac{1}{2} \frac{\partial h}{\partial t} V h^2 + \frac{1}{30} \frac{\partial UV}{\partial x} h^5 + \frac{1}{6} UV \frac{\partial h}{\partial x} h^4 + \frac{1}{6} V^2 \frac{\partial h}{\partial y} + \frac{1}{30} \frac{\partial V^2}{\partial y} h^5 \right) = 2Vh - \frac{\partial p}{\partial y} h \tag{A32}$$

On dividing this equation by h, we get

$$\left\{ \begin{aligned} \delta \left(-\frac{1}{6} \frac{\partial U}{\partial t} h^2 - \frac{1}{2} \frac{\partial h}{\partial t} U h + \frac{\partial U^2}{\partial x} \frac{h^4}{30} + \frac{1}{6} U^2 \frac{\partial h}{\partial x} h^3 + \frac{1}{6} UV \frac{\partial h}{\partial y} h^3 + \frac{\partial UV}{\partial y} \frac{h^4}{30} \right) &= 2U - \frac{\partial p}{\partial x} \\ \delta \left(-\frac{1}{6} \frac{\partial V}{\partial t} h^2 - \frac{1}{2} \frac{\partial h}{\partial t} V h + \frac{\partial UV}{\partial x} \frac{h^4}{30} + \frac{1}{6} UV \frac{\partial h}{\partial x} h^3 + \frac{1}{6} V^2 \frac{\partial h}{\partial y} h^3 + \frac{\partial V^2}{\partial y} \frac{h^4}{30} \right) &= 2V - \frac{\partial p}{\partial y} \end{aligned} \right. \quad (\text{A38})$$

A combining of similar terms results in

$$\left\{ \begin{aligned} \frac{\delta}{2} h \left(-\frac{1}{3} \frac{\partial U}{\partial t} h - \frac{\partial h}{\partial t} U \right) + \frac{\delta}{30} h^4 \left(\frac{\partial U^2}{\partial x} + \frac{\partial UV}{\partial y} \right) + \frac{\delta}{6} \left(U^2 \frac{\partial h}{\partial x} + UV \frac{\partial h}{\partial y} \right) h^3 &= 2U - \frac{\partial p}{\partial x} \\ \frac{\delta}{2} h \left(-\frac{1}{3} \frac{\partial V}{\partial t} h - \frac{\partial h}{\partial t} V \right) + \frac{\delta}{30} h^4 \left(\frac{\partial UV}{\partial x} + \frac{\partial V^2}{\partial y} \right) + \frac{\delta}{6} \left(UV \frac{\partial h}{\partial x} + V^2 \frac{\partial h}{\partial y} \right) h^3 &= 2V - \frac{\partial p}{\partial y} \end{aligned} \right. \quad (\text{A39})$$

The second term in the first equation of (A39) can be rewritten as

$$\frac{\partial U^2}{\partial x} + \frac{\partial UV}{\partial y} = U \frac{\partial U}{\partial x} + U \frac{\partial U}{\partial x} + U \frac{\partial V}{\partial y} + V \frac{\partial U}{\partial y} = U \left(\frac{\partial U}{\partial x} + \frac{\partial V}{\partial y} \right) + U \frac{\partial U}{\partial x} + V \frac{\partial U}{\partial y}$$

Since $\frac{\partial U}{\partial x} + \frac{\partial V}{\partial y} = 0$ (from the continuity equation, Eq.(4.12)), the final form is

$$\frac{\partial U^2}{\partial x} + \frac{\partial UV}{\partial y} = U \frac{\partial U}{\partial x} + V \frac{\partial U}{\partial y}$$

The second term in the second equation on (A39) can be transformed similarly.

On substituting back these transformations in (A39), the final form of the governing equations is expressed as

$$\boxed{\left\{ \begin{aligned} \frac{\delta}{2} h \left(-\frac{1}{3} \frac{\partial U}{\partial t} h - \frac{\partial h}{\partial t} U \right) + \frac{\delta}{30} h^4 \left(U \frac{\partial U}{\partial x} + V \frac{\partial U}{\partial y} \right) + \frac{\delta}{6} \left(U^2 \frac{\partial h}{\partial x} + UV \frac{\partial h}{\partial y} \right) h^3 &= 2U - \frac{\partial p}{\partial x} \\ \frac{\delta}{2} h \left(-\frac{1}{3} \frac{\partial V}{\partial t} h - \frac{\partial h}{\partial t} V \right) + \frac{\delta}{30} h^4 \left(U \frac{\partial V}{\partial x} + V \frac{\partial V}{\partial y} \right) + \frac{\delta}{6} \left(UV \frac{\partial h}{\partial x} + V^2 \frac{\partial h}{\partial y} \right) h^3 &= 2V - \frac{\partial p}{\partial y} \end{aligned} \right.} \quad (\text{A40})$$

Appendix B

Discretization of momentum equations

The final momentum equations, Eqn. (4.13), given in chapter 4 are replicated here for convenience.

$$-\frac{1}{6} \frac{\partial U}{\partial t} h^2 + \frac{\delta}{30} h^4 \left(U \frac{\partial U}{\partial x} + V \frac{\partial U}{\partial y} \right) + \frac{\delta}{6} \left(U^2 \frac{\partial h}{\partial x} + UV \frac{\partial h}{\partial y} \right) h^3 = 2U - \frac{\partial p}{\partial x} \quad (\text{B1})$$

$$-\frac{1}{6} \frac{\partial V}{\partial t} h^2 + \frac{\delta}{30} h^4 \left(U \frac{\partial V}{\partial x} + V \frac{\partial V}{\partial y} \right) + \frac{\delta}{6} \left(UV \frac{\partial h}{\partial x} + V^2 \frac{\partial h}{\partial y} \right) h^3 = 2V - \frac{\partial p}{\partial y} \quad (\text{B2})$$

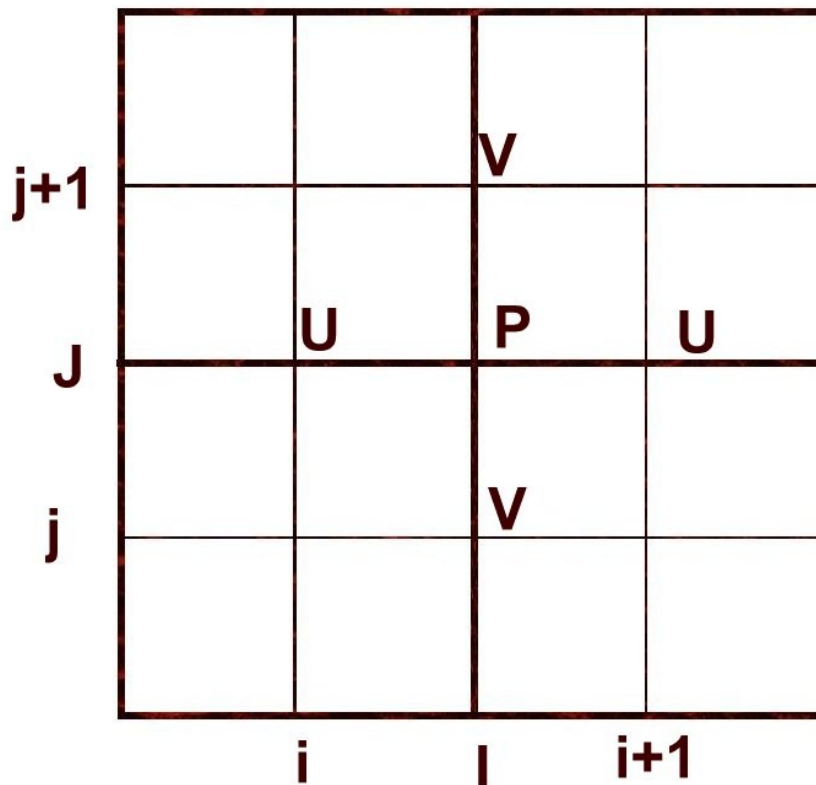


Figure B.1 Staggered grid arrangement

Staggered grid arrangement is shown in Figure B.1. This grid arrangement provides a stronger coupling between fluid pressure and velocities, thereby improving the stability of the solution. The primary grid-points, where the scalar quantities as pressure P and

temperature T are stored, are denoted with capital letters. The secondary grid-points, where vector quantities such as velocities U and V are stored, are denoted with small letters.

The discretized form of momentum equations on the staggered grid, using the first order, forward difference scheme in time and the central difference scheme in space, is shown below.

Momentum equation

In the x direction:

$$\begin{aligned}
 & -\frac{1}{6} \frac{U_{i+1,J}^{n+1} - U_{i+1,J}^n}{\Delta t} + \frac{\delta}{30} h_{i+1,J}^4 \left[\frac{(U^2)_{I+1,J}^n - (U^2)_{I,J}^n}{\Delta x} + \frac{(UV)_{i+1,j+1}^n - (UV)_{i,j+1}^n}{\Delta y} \right] \\
 & + \frac{\delta}{6} h_{i+1,J}^3 \left[U_{I,J}^2 \frac{(h)_{I+1,J}^n - (h)_{I,J}^n}{\Delta x} + UV_{I,J} \frac{(h)_{i+1,j+1}^n - (h)_{i+1,j}^n}{\Delta y} \right] \\
 & = 2 * U_{I,J}^n - \frac{(P)_{I+1,J}^n - (P)_{I,J}^n}{\Delta x}
 \end{aligned} \tag{B3}$$

In the y direction:

$$\begin{aligned}
 & -\frac{1}{6} \frac{V_{I,j+1}^{n+1} - V_{I,j+1}^n}{\Delta t} + \frac{\delta}{30} h_{I,j+1}^4 \left[\frac{(V^2)_{I,J+1}^n - (V^2)_{I,J}^n}{\Delta x} + \frac{(UV)_{i+1,j+1}^n - (UV)_{i+1,j}^n}{\Delta y} \right] \\
 & + \frac{\delta}{6} h_{I,j+1}^3 \left[V_{I,J}^2 \frac{(h)_{I,J+1}^n - (h)_{I,J}^n}{\Delta x} + UV_{I,J} \frac{(h)_{i+1,j+1}^n - (h)_{i,j+1}^n}{\Delta y} \right] \\
 & = 2 * V_{I,J}^n - \frac{(P)_{I,J+1}^n - (P)_{I,J}^n}{\Delta y}
 \end{aligned} \tag{B4}$$

Due to the staggered-grid arrangement used for the discretization of our partial differential equations, the values of velocities are available only on the secondary-grid points. An interpolation must be used to determine velocities on the primary-grid points. The following relations can be used:

$$\left(U^2\right)_{I,J+1} = \frac{1}{4} \left(U_{i+2,J} + U_{i+1,J}\right)^2 \quad (\text{B5})$$

$$\left(U^2\right)_{I,J} = \frac{1}{4} \left(U_{i+1,J} + U_{i,J}\right)^2 \quad (\text{B6})$$

$$\left(V^2\right)_{I,J+1} = \frac{1}{4} \left(V_{I,j+2} + V_{I,j+1}\right)^2 \quad (\text{B7})$$

$$\left(V^2\right)_{I,J} = \frac{1}{4} \left(V_{I,j+1} + V_{I,j}\right)^2 \quad (\text{B8})$$

$$(UV)_{i+1,j+1} = \frac{1}{4} \left(U_{I+1,j+1} + U_{I,j+1}\right) \left(V_{i+1,J+1} + V_{i+1,J}\right) \quad (\text{B9})$$

$$(UV)_{i,j+1} = \frac{1}{4} \left(U_{I,j+1} + U_{I-1,j+1}\right) \left(V_{i,J+1} + V_{i,J}\right) \quad (\text{B10})$$

$$(UV)_{i+1,j} = \frac{1}{4} \left(U_{I+1,j} + U_{I,j}\right) \left(V_{i+1,J} + V_{i+1,J-1}\right) \quad (\text{B11})$$

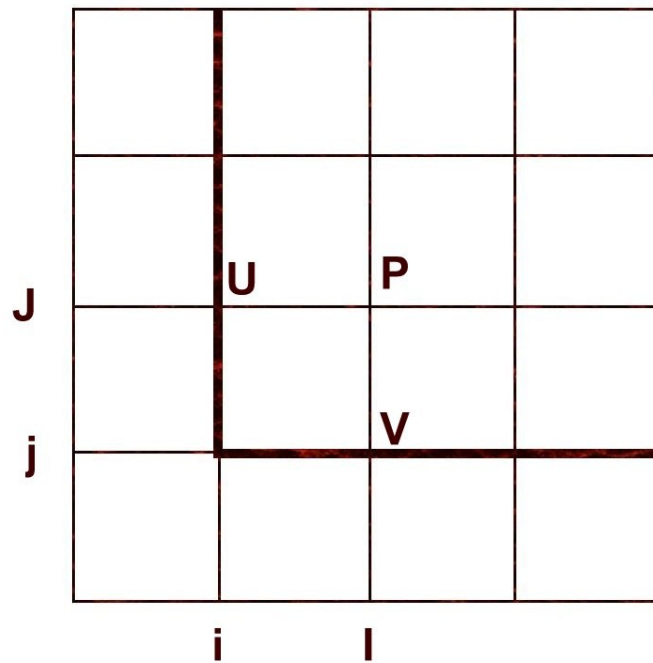


Figure B.2. Grid lines arrangement near the channel walls

In order to eliminate the need for pressure values at the boundaries, walls of the channel are made to coincide with the secondary-grid lines. Then fluid pressure is calculated inside the channel only.

No-slip boundary condition can be expressed as:

$$U_{i,j} = U_{i+1,j} = \dots = 0$$

$$V_{i,j} = V_{i+1,j} = \dots = 0$$

Values such as $U_{i,J-1}$ is required in the analysis and can be found as:

$$U_{I,j} = \frac{1}{2} (U_{I,J} + U_{I,J-1}) = 0 \Rightarrow U_{I,J-1} = -U_{I,J}$$

At the inflow boundary, velocities in the direction of flow, U , are known from the initial conditions. Velocities outside the boundary, such as $V_{I-1,j+1}$, are needed for the solution, and can be found from the extrapolation

$$V_{I-1,j+1} = V_{I,j+1} - \frac{\partial V}{\partial x} \Delta x = V_{I,j+1} - \frac{V_{I+1,j+1} - V_{I,j+1}}{\Delta x} \Delta x = 2V_{I,j+1} - V_{I+1,j+1}$$

Appendix C

Estimation of location of solid-liquid interface

Using the Stefan condition, the solid-liquid interface velocity can be calculated as

$$\rho L_f \frac{s_i^{n+1} - s_i^n}{\Delta t} = k_s \left. \frac{\partial T_s}{\partial x} \right|_{x=s(t)} - k_l \left. \frac{\partial T_l}{\partial x} \right|_{x=s(t)} \quad (C1)$$

When solid liquid interface is formed, $\frac{\partial T_s}{\partial x}$ term reduces to 0 since the interface temperature is kept at the melting point everywhere, while $\frac{\partial T_l}{\partial x}$ is estimated based on the temperature distribution in the liquid metal.

To compute the movement of the interface with time, the 1-D velocity of the solid-liquid interface is multiplied by the time step:

$$\Delta h_i^{n+1} = s_i^{n+1} * \Delta t \quad (C2)$$

Then the current height of the channel is estimated as

$$h_i^{n+1} = h_i^n - 2\Delta h_i^{n+1} \quad (C3)$$

with the factor of 2 being used to include the effect of interface movements both from top and bottom. A typical interface motion is shown in Fig. C.1

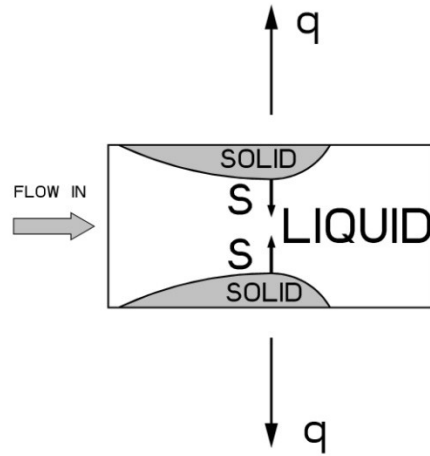


Figure C.1 A schematic showing the growth of solid-liquid interface due to metal solidification on the channel walls.

CURRICULUM VITAE

Alexandre Reikher

Place of birth Kishinev USSR

BS Kishinev Polytechnic Institute Kishinev USSR

Major: Mechanical Engineering

PhD UW Milwaukee, Milwaukee WI

Major: Engineering

Professional Publications:

Book:

” Casting: An analytical approach”, Springer, July 2007.

Papers:

1. Multi-Stage Plunger Deceleration System, NADCA congress 2008
2. Die-casting end-of-fill and drop forge viscometer flow transients examined with a coupled-motion numerical model. 68th WORLD FOUNDRY CONGRESS
3. Application of one dimensional numerical simulation to optimize process parameters of a thin wall casting in high pressure die casting process. Die Casting Engineer, May 2009.
4. Simulation of welding of aluminum parts using high energy laser beam, Presented on 2010 ASME international mechanical engineering congress Vancouver BC
5. Optimization of high vacuum die cast process. Die cast Engineer, July
6. A fast numerical simulation for modeling simultaneous metal flow and solidification in thin cavities using the lubrication approximation, Journal of Numerical Heat Transfer 2013